

Investigation of 90RWG – 10Na₂O – 0.01Cu₂O Thermoluminescence Dosimeter on the Effective Atomic Number and Elastic Properties

Y. Jaichueai^{1*}, J. Laopaiboon¹, C. Bootjomchai¹, C. Yenchai² and R. Laopaiboon^{1**}

¹Department of Physics, Faculty of Science, Ubon Ratchatani University, Ubon Ratchatani 34190, Thailand

²Department of Nuclear Engineering, Faculty of Engineering, Chulalongkorn University, Bangkok 10330, Thailand

* E-mail: Yuthachai.a@gmail.com

** E-mail: Raewatl@yahoo.com

Abstract

In this work, thermoluminescence radiation dosimeter type 90RWG – 10Na₂O – 0.01Cu₂O was investigated on their elastic properties, structural properties and effective atomic number. The glass samples were prepared by melt quenching technique. All glass samples were melted at temperature 1250 °C for 4 hr and annealed at temperature 500 °C for 2 hr. Then, the ultrasonic velocities were measured by ultrasonic technique at 4MHz and at room temperature. All glass samples were irradiated by radiation machine with gamma ray at 1 kGy. The elastic moduli (bulk modulus, Young's modulus Poisson's ratio and micro-hardness) were calculated before and after gamma irradiation at 1 kGy. FTIR spectroscopy was measured in wave number range 400 - 4000 cm⁻¹ to study structure of the glass samples before and after gamma irradiation. The results of elastic properties and structural properties before and after gamma irradiation were depend on Cu₂O content and damaged from gamma ray. This related to the number of bridging oxygen in glass network. The mass attenuation coefficient and effective atomic number could be calculated and were measured using the narrow beam transmission method. The theoretical values of effective atomic number were calculated by WinXCom program. The results of mass attenuation coefficient are good agreement between theoretical and experimental value. The effective atomic number in range 13-16 is quite close to that of bone.

Keywords: Glass, Thermoluminescence, Elastic moduli, Effective atomic number

Introduction

Nuclear technology is involves the reactions of atomic nuclei. It's has many applications in agriculture, medicine, industry and research. In medical applications, nuclear technology was divided into diagnostics and radiation treatment. The workers associated with radiation must have the personal radiation dosimeters due to the workers may be caused by exposure to radiation that originates outside the body. Thus, radiation dosimeters are important for the workers associated with radiation. One of the radiation dosimeters is thermoluminescence dosimeter (TLD). TLD are often used instead of the film badge. The two most common types of TLDs are lithium fluoride (LiF) and calcium fluoride (CaF₂). Lithium fluoride was used for dose measurements in radiotherapy since the effective atomic number of 8.3 ($Z_{\text{eff}} \sim 8.2$) is close to that of the soft

tissue or human tissue equivalent ($Z_{\text{eff}} \sim 7.42$) [1-4]. Thus, the medical application of TLD depends on the effective atomic number for each TLD kind. W. Sarakom et al. was studied the thermoluminescence properties of glass system 90RWG – 10Na₂O - xR_mO_n (where RWG is recycle window glass, R_mO_n are CrO₃, MnO₂, Cu₂O and NiO and x = 1, 0.1, 0.01, 0.001 mol%). They reported that the recycle window glass with 0.01 mol% of Cu₂O dopant has potential the thermoluminescence radiation dosimeter [5].

The purpose of the present work is to studied the structural, elastic properties and effective atomic number of 90RWG – 10Na₂O – 0.01Cu₂O glass system. The ultrasonic velocities of glass samples were measured by pulse echo technique and could be calculated elastic moduli before and after gamma irradiation at 1 kGy. Mass attenuation coefficient was measured by narrow beam

transmission method and could be calculated for effective atomic number. FTIR spectroscopy was measured in wave number range 400 - 4000 cm^{-1} before and after gamma irradiation at 1 kGy.

Materials and Methods

Preparation of the glass samples

The chemical composition analyses of the recycled window glass carried out by using the WDXRF technique and as shown in Table 1. The chemical composition of glass sample was weighed using a digital balance having accuracy of 0.0001 g and put into a ceramic crucible. Then, the chemical composition were melted using electric furnace at the temperature 1250°C for 2 hr and annealed at 450°C for 2 hr. Glass samples were cut into size 1×1 sq.inch and polished by using different grades of silicon carbide and aluminum powder respectively. The thickness measurement was carried out by vernier caliper.

Table 1 Quantitative analysis of chemical composition of RWG by using WDXRF technique

Chemical composition	Concentration (%)
Na ₂ O	15.1700
MgO	3.4080
SiO ₂	73.3900
Al ₂ O ₃	0.5866
CaO	7.3390
Fe ₂ O ₃	0.0635
TiO ₂	0.0263
K ₂ O	0.0238

Density and molar volume measurements

The densities of all glass samples were determined by Archimedes' principle using n-hexane as an immersion liquid and applying the relation [6]

$$\rho = \rho_l \left(\frac{W_a}{W_a - W_b} \right) \quad (1)$$

where ρ_l is the density of n-hexane, W_a and W_b are the glass sample weights in air and in n-hexane, respectively.

The molar volume (V_a) of the glass samples was calculated using the relation [7]

$$V_a = \frac{M}{\rho} \quad (2)$$

Where V_a is the molar volume of glass samples. M is the molecular weight of the glass samples and ρ is density of glass samples.

Ultrasonic velocity measurement

The ultrasonic velocities were measured using by pulse echo technique. The Ultrasonic flaw detector, SONATEST Sitescan 230 was used to measure ultrasonic wave velocity. The ultrasonic velocity can be calculated by the relation [8].

$$v = \frac{2x}{\Delta t} \quad (4)$$

where x is the glass sample thickness and Δt is the time interval.

Calculation of elastic moduli

The elastic properties include longitudinal modulus (L), Shear modulus (G), bulk modulus (K), Young's modulus (E), Poisson's ratio (σ) and micro-hardness (H) of the glass samples have been determined from the value of ultrasonic velocities and density using the relations [9].

Longitudinal modulus:

$$L = \rho V_L^2 \quad (5)$$

Shear modulus:

$$G = \rho V_S^2 \quad (6)$$

Bulk modulus:

$$K = L - \frac{4}{3}G \quad (7)$$

Young's modulus:

$$E = (1 + \sigma)2G \quad (8)$$

Poisson's ratio:

$$\sigma = \frac{L-2G}{2(L-G)} \quad (9)$$

Micro-hardness:

$$H = \frac{(1-2\sigma)E}{6(1+\sigma)} \quad (10)$$

Gamma irradiation

All glass samples were irradiated by radiation machine (THERATRON 780C) and gamma ray source with a dose rate of 3.26 Gy/min at room temperature. The distance between source and sample is 80 cm and field size is 30x30 cm². The glass samples were irradiated with gamma ray at 1 kGy. The diagram of geometry is shown in Figure 1.

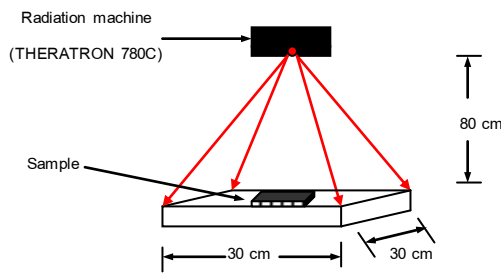


Figure 1 Geometrical arrangement of gamma irradiation

Narrow beam transmission method measurements

The geometry of narrow beam transmission method as shown in Figure 2. The linear attenuation coefficient was measured by narrow beam transmission method. Then, mass attenuation coefficient has been determined from the value of linear attenuation coefficient and density of glass samples.

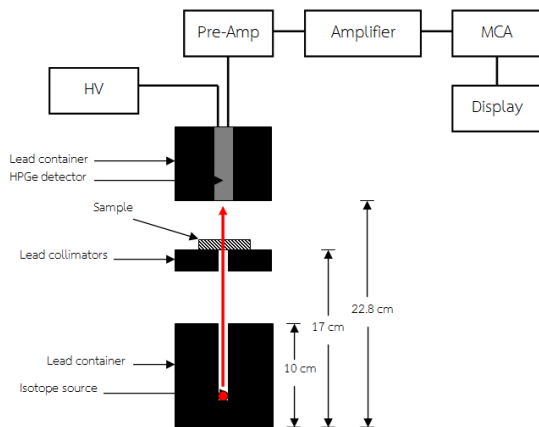


Figure 2 Experimental setup of narrow beam transmission method

Theoretical method

All glass samples are placed in the path of a beam of monoenergetic γ -ray radiations, the intensity of γ -ray beam will be attenuated according to the Beer–Lambert’s law. This equation is given below as

$$I = I_0 e^{-\mu x} \quad (11)$$

where I and I_0 are the incident and transmitted intensity of gamma radiation, x is the thickness of the absorbing medium and μ is the linear attenuation coefficient. Mass attenuation coefficients are used to determine the total atomic cross-section $\sigma_{t,a}$ by the following relation [10]

$$\sigma_{t,a} = \frac{\mu/\rho}{N_A \sum_i (w_i/A_i)} \quad (12)$$

where N_A is Avogadro’s number, A_i is atomic weight of element i , Also the total electronic cross-section ($\sigma_{t,el}$) of the element is expressed by the following formula [11]

$$\sigma_{t,el} = \frac{1}{N_A} \sum_i \frac{f_i A_i}{Z_i} (\mu/\rho)_i \quad (13)$$

where f_i and Z_i are the fractional abundance and atomic number, respectively, of constituent element i . Total atomic cross-section and total electronic cross-section are related to effective atomic number (Z_{eff}) of the compound through the formula [12]

$$Z_{eff} = \frac{\sigma_{t,a}}{\sigma_{t,el}} \quad (14)$$

FTIR spectroscopy measurements

The Infrared spectra of prepared glasses were performed using a Fourier Transform Infrared spectrometer. The glass samples were measured in the wavelength range 400 – 2000 cm⁻¹ using the KBr disk technique. The powdered glass samples were mixed with KBr in the ratio 1:100 (glass powder: KBr).

WinXCom program

The WinXCom program can be calculate the mass attenuation coefficients of elements, compounds and mixture materials. Moreover, WinXCom program also indicate that the three mechanism (Photoelectric absorption, Compton scattering and pair production) of matter. WinXcom program were developed the theoretical tables and computer program for calculation by Gerward et al. [13,14].

Results and Discussion

Density and molar volume of glass

The density and molar volume value was shown in Table 2. The density increase from 2.5526 to 2.5695 g.cm^{-3} when the content of doping Cu_2O increases in glass system. Density of glass samples increase due to the molecular weights of Cu_2O in glass system. The molecular weights of Cu_2O have more than silica (SiO_2). Molecular weight of Cu_2O is 143.08 g.mol^{-1} and 60.09 g.mol^{-1} of silica, respectively. The molar volume has decreased with the increasing of Cu_2O content in glass system. The decrease in molar volume could be explained using Equation (2). The increasing in density of glass samples are leads to the decrease in molar volume of glass samples.

Table 2 Chemical composition, density and molar volume of glass system

	Chemical composition (mol%)			$\rho(\text{g/cm}^3)$	$V_a(\text{cm}^3/\text{mol})$
	WG	Na_2O	Cu_2O	± 0.0004	± 0.006
S1	100	-	-	2.5243	23.554
S2	90	10	-	2.5526	23.487
S3	90	10	0.01	2.5695	23.337

Ultrasonic velocities and elastic moduli

The ultrasonic velocities were measured before and after gamma irradiation at 1 kGy by pulse echo technique. The value of longitudinal and shear velocities before and after gamma irradiation at 1 kGy as shown in Figure 3. and Figure 4, respectively. In before irradiation, glass doped 0.01 mol% of Cu_2O content, the longitudinal and

shear velocities of glass sample doped with 0.01 mol% of Cu_2O content have value greater than the sample undoped Cu_2O content. After irradiation, the longitudinal and shear velocities are less than the value of longitudinal and shear velocities for before gamma irradiation at 1 kGy of glass sample doped with 0.01 mol% of Cu_2O content. The decreases in the ultrasonic velocities for after gamma irradiation at 1 kGy are due to the damage from gamma ray. Normally, the increase in longitudinal and shear velocities is related to the decrease in the number of non-bridging oxygens and connectivity of glass network [15].

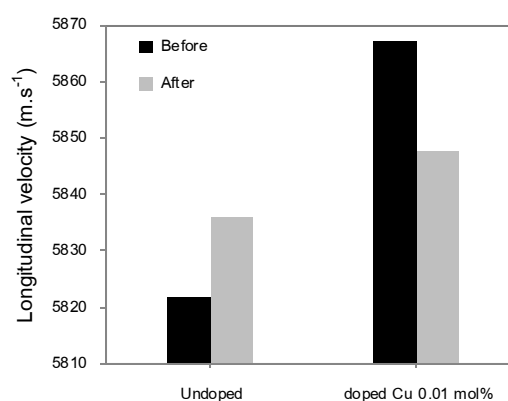


Figure 3 Variation of longitudinal velocities before and after gamma irradiation at 1 kGy for glass sample undoped and doped 0.01 mol% of Cu_2O content

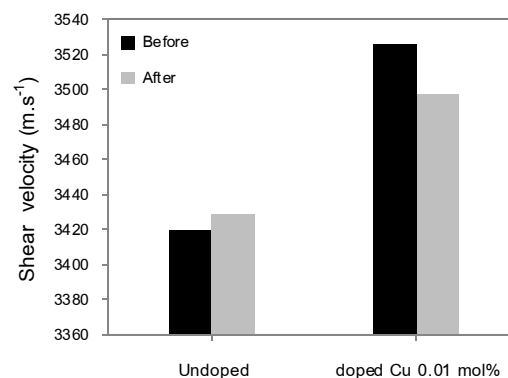


Figure 4 Variation of shear velocities before and after gamma irradiation at 1 kGy for glass sample undoped and doped 0.01 mol% of Cu_2O content

Young's modulus and bulk modulus as shown in Figure 5 and Figure 6, respectively. Young's modulus value of glass sample doped with 0.01 mol% of Cu_2O content have more

than the sample undoped Cu₂O content and decreased after irradiation at 1 kGy for glass sample doped with 0.01 mol% of Cu₂O content. This leads to the increasing of non-bridging oxygen in glass network. Young's modulus reveals shown the rigidity of glass system. Moreover, the values of Young's modulus are related to the change in the number of non-bridging oxygen (NBO) in the glass network [16]. Bulk modulus, the glass sample undoped Cu₂O content have value greater than the glass sample doped with 0.01 mol% of Cu₂O content for before gamma irradiation at 1 kGy. Then, the value of bulk modulus have increase after gamma irradiation at 1 kGy for glass sample doped with 0.01 mol% of Cu₂O content and undoped Cu₂O content. Bulk modulus reveals the change in the cross-linkage coordination of glass network [17]. The increase in bulk are reveals the increase in cross-linkage coordination of glass network.

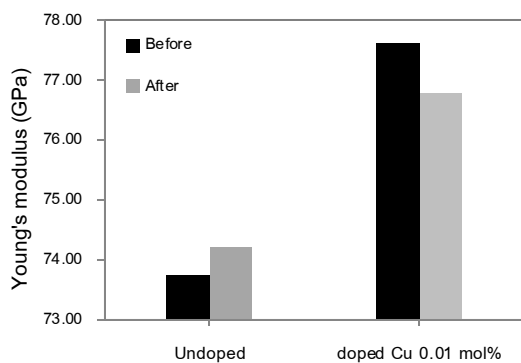


Figure 5 Variation of Young's modulus before and after gamma irradiation at 1 kGy for glass sample undoped and doped 0.01 mol% of Cu₂O content

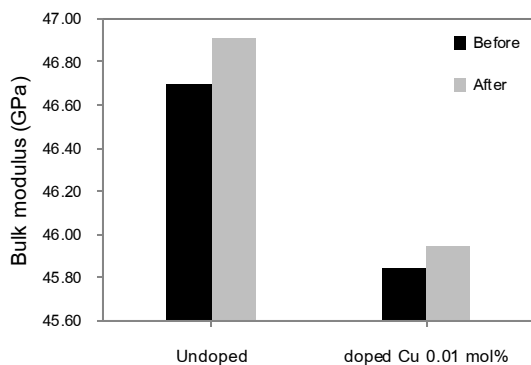


Figure 6 Variation of bulk modulus before and after gamma irradiation at 1 kGy for glass sample undoped and doped 0.01 mol% of Cu₂O content

Poisson's ratio and micro-hardness was shown in Table 3. Poisson's ratio reveals the cross-link density which is defined as the number of bridging bonds per cation [18]. The values of Poisson's ratio are decrease for glass sample doped with 0.01 mol% of Cu₂O content. Thus, the decreases of Poisson's ratio were shown that the increasing of cross-link density due to decrease of number of non-bridging oxygen [19]. The values of micro-hardness before gamma irradiation are more than the glass sample after irradiation for glass sample doped with 0.01 mol% of Cu₂O content. The micro-hardness reveals the solidity of glass network structure and micro-hardness relate to Poisson's ratio and Young's modulus.

Table 3 Micro-hardness and Poisson's ratio before and after gamma irradiation at 1 kGy for glass sample undoped and doped 0.01 mol% of Cu₂O content

Cu ₂ O (mol%)	$H \pm 0.022$ (GPa)		$\sigma \pm 0.0007$	
	Before	After	Before	After
undoped	5.274	5.276	0.2350	0.2363
0.01	6.083	5.836	0.2144	0.2214

Fourier transforms infrared absorption

The FTIR spectra for the glass with Cu₂O doped at the concentrations 0.01 mol% as shown in Figure 7. All glass samples were measured at room temperature in the wave number range 400–2000 cm⁻¹. The glasses network has the vibrations appear in the range 400–1500 cm⁻¹. The detailed assignments of IR bands of 90RWG – 10Na₂O – 0.01Cu₂O glasses are shown in the Table 4. In Figure 7, the first vibration signals at around 470 cm⁻¹ are assigned to the Si–O–Si bending modes of bridging oxygen. The peaks near 775-800 and 960 cm⁻¹ are assigned to the vibrations of O–Si–O bonds and vibrations of non-bridging oxygen (NBO), Si–O–Si bending modes, respectively. The peak in the region range of 1050-1120 cm⁻¹ is assigned to Si–O–Si anti symmetric stretching of Si-O-Si. The signal at approximately 1600 cm⁻¹ is assigned molecular water [20]. In wavenumber at 960-1150 cm⁻¹, the vibration of the Si–O–Si bending modes has more than the glass after gamma irradiation due to the structure damaged from gamma ray. This cause leads to not strong of glass and the value of elastic moduli for after gamma irradiation is less than the glass before gamma irradiation.

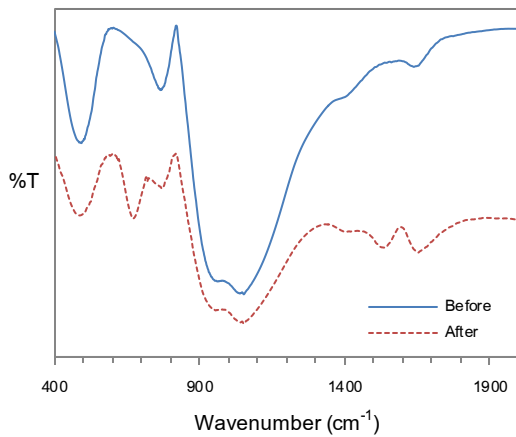


Figure 7 The IR spectra of the glass samples before and after gamma irradiation at 1 kGy for glass sample undoped and doped 0.01 mol% of Cu_2O content

Calculation of effective atomic number

Mass attenuation coefficient could be calculated by using the value of linear attenuation coefficient. The linear attenuation coefficient was evaluated from Beer–Lambert’s law equation. The value of mass attenuation coefficient between theoretical and experimental value was shown in Table 5. The value of mass attenuation coefficient from experiment and theoretical are correspond between experimental and theoretical value. In this work, the energy for experiment is 122, 662, 1173 and 1332 keV. The theoretical value of mass attenuation coefficient was calculated using WinXCom program. The effective atomic number (Z_{eff}) could be calculated using eq. (14). The effective atomic number between theoretical and experiment as shown in Figure 8. The values of theoretical effective atomic number were decreased with the increasing of photon energy. The experimental values of effective atomic number are more than the theoretical value. The experimental values of effective atomic number are not agreement with the theoretical value due to the total atomic cross-section of experimental values have more than the total atomic cross-section of theoretical value. Thus, the effective atomic number in range 14-16 for glass sample doped 0.01 mol% of Cu_2O content is quite close to that of bone. The effective atomic number is important for the treatment of disease, especially cancer, using X-rays or similar forms of radiation. Thus, the glass samples can be used instead human bone for treatment disease.

Table 4 Depicts the detailed assignments of IR bands of 90RWG – 10 Na_2O – 0.01 Cu_2O glass system

Peak position (cm^{-1})	Assignment
460-480	Bending vibration of Si-O-Si linkages [21]
640-680	Si-O-Si and O-Si-O bending [22]
775-800	Symmetric stretching vibrations of O-Si-O bonds [21]
960	Vibrations of non-bridging oxygen(NBO) [22]
1050–1120	Anti symmetric stretching of Si-O-Si linkages [20]
1400–1460	Carbonate group [21]
1630–1645	Molecular water [22]

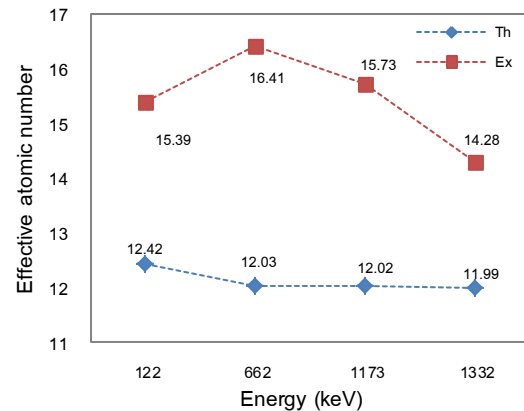


Figure 8 Variation of effective atomic number values for 90 RWG – 10 Na_2O - 0.01 Cu_2O glass as a function of energy

Table 5 mass attenuation coefficient of glass samples between theoretical and experimental value (cm^2/g)

Energy (keV)	undoped		0.01 mol% of Cu_2O content	
	<i>Ex</i>	<i>Th</i>	<i>Ex</i>	<i>Th</i>
122	0.141	0.156	0.152	0.158
662	0.074	0.077	0.070	0.077
1173	0.050	0.058	0.054	0.058
1332	0.050	0.055	0.048	0.054

Conclusions

Before irradiation, the value of elastic moduli except for bulk modulus was increased for glass sample doped with 0.01 mol% of Cu_2O content. While, bulk modulus were decreased for glass sample doped with 0.01 mol% of Cu_2O content. After irradiation, Young's modulus has less than the value before irradiation of glass sample doped with 0.01 mol% of Cu_2O content. The increase in bulk modulus for glass sample doped with 0.01 mol% of Cu_2O content are more values than bulk modulus before irradiation. The FTIR spectra are indicate that the decreasing of absorption of function group in glass network after irradiation for glass sample doped with 0.01 mol% of Cu_2O content. The results of FTIR spectra also support the result of the ultrasonic technique. Then, the value of mass attenuation coefficient from experiment and theoretical are correspond between experimental and theoretical value. The effective atomic number for experimental value is quite close to that of bone and can be used instead human bone for treatment disease.

Acknowledgments

The authors would like to thank Department of Physics and Department of Chemistry, Faculty of Science, Ubon Ratchathani University and Ubon Cancer Hospital for ultrasonic velocities measurement, FTIR spectroscopy and radiation machine (THERATRON 780C), respectively. Moreover, the authors would like to thank Department of Nuclear Engineering, Faculty of Engineering, Chulalongkom University for supporting narrow beam transmission method.

References

- [1] Vu Thi Thai Ha, 2007. "Preparation and characteristics of LiF:Mg,Cu,Na,Si thermoluminescent material". **Journal of Science, Mathematics - Physics** 23, 225-231.
- [2] Andreia Ruivo, César A.T. Laia, 2014. "Time-resolved luminescence studies of Eu^{3+} in soda-lime silicate glasses", **Journal of Quantitative Spectroscopy & Radiative Transfer**. 134, 29–38
- [3] A. Un, 2013. "Investigation of dopant effect on some TL dosimeters containing boron". **Radiation Physics and Chemistry** 85, 23–35
- [4] M. Marrale, A. Longo, A. Bartolotta, S. Basile, M.C. D'Oca, E. Tomarchio, G.A.P. Cirrone, F. Di Rosa, F. Romano, G. Cuttone, M. Brai, 2012. "Thermoluminescence response of sodalime glass irradiated with proton and neutron beams", **Nucl. Instr. Meth. B** 292, 55–58.
- [5] Witchuda Sarakom, 2013. "Themolminescence properties of recycled window glass doped NiO CrO_3 MnO_2 and Cu_2O as radiation dosimetry material", special project department of physics, ubonratchathani university.
- [6] Samir Y. Marzouk. 2009. "Ultrasonic and infrared measurements of copper-doped sodium phosphate glasses". **Materials Chemistry and Physics** 114, 188–193.
- [7] M.S. Gaafar, S.Y. Marzouk. 2007. "Mechanical and structural studies on sodium borosilicate glasses doped with Er_2O_3 using ultrasonic velocity and FTIR spectroscopy". **Physica B** 388, 294-302.
- [8] El-Mallawany, R.El-Khoshkhany, N., Afifi, H. 2006. "Ultrasonic studies of $(\text{TeO}_2)_50 - (\text{V}_2\text{O}_5)_50-x - (\text{TiO}_2)_x$ glasses". **Mater. Chem. Phys.** 95, 321–327.
- [9] M.A. Sidkey, M.S. Gaafar. 2006. "Ultrasonic studies on network structure of ternary $\text{TeO}_2 - \text{WO}_3 - \text{K}_2\text{O}$ glass system". **Physica B** 348, 46–55.
- [10] Gerward, L, Guilbert, N., Jensen, K.B, Levring, H., 2004. "WinXCom –a program for calculating x-ray attenuation coefficients", **Radiat.Phy.Chem.** 71, 653-654.
- [11] Singh, N., Singh, K.J., Singh, K., Singh, H., 2006. "Gamma-ray attenuation studies of $\text{PbO-BaO-B}_2\text{O}_3$ glass system". **Radiat. Meas.** 41, 84-88.
- [12] Shaema, G., Singh, K., "Manupriya, Mohan, S., Singh, H. Mohan, Bindra, S., 2006. "Effect of gamma irradiation on option and structural properties of $\text{PbO-Bi}_2\text{O}_3$ glass". **Radiation Physics and Chemistry** 75, 959-966.

- [13] Gerward, L., Guilbert, N., Jensen, K.B., Levring, H., 2001. "X-ray absorption in matter". Reengineering XCOM. **Radiation Physics and Chemistry** 60, 23–24.
- [14] Gerward, L., Guilbert, N., Jensen, K.B., Levring, H., 2004. "WinXCom – a program for calculation X-ray attenuation coefficients". **Radiation Physics and Chemistry** 71, 653–654.
- [15] M.S. Gaafar, S.Y. Marzouk. 2007. "Mechanical and structural studies on sodium borosilicate glasses doped with Er_2O_3 using ultrasonic velocity and FTIR spectroscopy". **Physica B** 388, 294-302.
- [16] H. Affi, S. Marzouk, 2003, "Ultrasonic velocity and elastic moduli of heavy metal tellurite glasses". **Materials chemistry and physics** 80 , 517-523.
- [17] Prado, M.O. Messi, 2001, "The effects of radiation on the density of an aluminoborosilicate glass". **Journal of Non-Crystalline Solids** 289, 175-184.
- [18] B.Bridge, A.A Higazy, 1986, "Model of the Compositional Dependence of the Elastic Moduli of Polycomponent Oxide Glasses". **Physics and Chemistry of Glasses** 27, 1-14.
- [19] A.V. Gayathri Devi, V.Rajendran, 2010, "Ultrasonic characterisation of calcium phosphate glasses and glass-ceramics with addition of TiO_2 ". **Journal of Engineering Science and Technology** 2(6), 2483-2490.
- [20] E.M.A. Khalil, 2011, "*Infrared absorption spectra of transition metals-doped soda lime silica glasses*". **Physica B**. 405, 1294–1300.
- [21] S.P.H.S. Hashim, 2011, "*physical properties of borotellurite glass doped with manganese*". **Solid State Science and Technology**, Vol.19, 342-347.
- [22] F.H. ElBatal. 2014. "Characterization by combined optical and FT infrared spectra of 3d-transition metal ions doped-bismuth silicate glasses and effects of gamma irradiation", **Spectrochimica Acta Part A: Molecular and Biomolecular Spectroscopy**. 122, 461–468.

Design and Development of Colorimetry Program on a Smart Phone for pH Determination

K. Armart, J. Laopaiboon and S. Pencharee*

Department of Physics, Faculty of Science, UbonRatchathani University, 85 Sathonlamark Road, Warinchumrab, UbonRatchathani, 34190

*E-mail: Somkid.p@ubu.ac.th

Abstract

As pH values was widely used in medical, industrial and environmental. Determination of pH can be using chemical methods. This study has the capabilities of smart phones to use analysis of color solution called "pH value" as needs to know the pH. The pH indicator solution was dropped to the samples and then the color changes according to the pH. The sample put within a drapes box for prevent optical interference. Inside the box, install two white light compact fluorescent lamps as the light source. At the front of the box was drill for take a picture in the box. The color was read and evaluate to pH by pH value application. The result found that the pH range of 4.0 – 8.0 can be correctly identified. This research was a simple system can be applied to many applications, low cost and easy to carry.

Keywords: pH, Smart phone, Image processing, Chemical method

Introduction

The pH is an indicator of the widely used in many fields such as the environment, industry and medicine. To describe the important features of the solution, the pH value is used to measure the acidity or alkalinity of a solution and it depends on the reaction of hydrogen ion concentration. Especially, the value of a neutral intermediate aqueous solution is pH 7.0 at the reference temperature of 25 °C; solutions with a pH value below 7.0 are considered acid, and those with a pH value above 7.0 are base. The acidity - alkalinity of the solution will affect the chemical properties of natural resources such as water and soil. Due to water and soil are important to the lives of humans, plants and animals it has to be the recommended the pH range is appropriate and how to

measure the pH value of solution was mixed in water or soil. To control the acid – base and in order to use these resources to the maximum benefit. The suitable pH range for to water or soil resources, usually to be in a neutral pH range. [1 - 2]

Acidity - alkalinity of the solution will be identify able by chemical methods such as the use litmus blue or red, this method able to tell only acidity (blue to red) or alkalinity (red to blue). For how to using of universal indicator paper and solution, even if it can be compared to a color chart to indicate the pH but it may be an error because of the color via naked eye or with optical interference from the environment as well as color charts to deteriorated. For pH meter has two types of pens and desk either way, though with high precision but it is expensive as well. There is

also a method of storage devices are difficult to use. And some are not easy to use in the field. [3 - 7]

The advancement in technology and the electronics industry has led to the development of computers and the various electronic media. Particular the technology of android operating system on portable devices include tablets, smart phones and net books [8]. These devices often have digital color camera installed on the inside and have a function that can be optimized for versatile. Especially when applied in detecting and measure the intensity of the color is technically called "Colorimetry" whether is presented for analysis image the spectrums are projected onto a ripeness banana for level [9]. Deploy as a colorimeter for the chlorine concentration in water [10, 11]. And the color analysis to assess their levels of rice leaf nitrogen [12]. Therefore, in this study and the development of applications for analysis pH value of solution by preparing buffer solution with pH differences and clear.

Structure of the smart phone based color analysis of buffer solution

The structure of the smart phone based color analysis design is shown in Figure 1. Consisted of a smart phone, inside a drapes box have the white paper reference scene, a test tube with buffer solution inside and the install two white light compact fluorescent lamps as the light source (Each 8 Watt). The test tube is located in front of the reference scene. Front of the box is drill a hole to use to camera shooters the smart phone. The test tube will be set to match with a peephole for the shooting. The smart phone will be adjusted view of the digital color the camera to provide see the test tube and reference scene be clearly. And used Indicator for determine pH in the range 3.0 to 9.0. So that the solution to change color and then photograph the color of the solution. Color images are saved automatically registered into red, green, and blue color planes. To indicate the pH value of solution at the pixel (x, y) and saved the

picture. Found that the planes of the red and green color of the solution changes affect so, internal application was written the conditions to calculate the pH needs to know it. To be used of the red planes as a basis for decision making. If the red plane is than or equal to 140 pH values was calculated by equation (1), but if the red planes is less than 140 to calculate the pH values of equation (2).

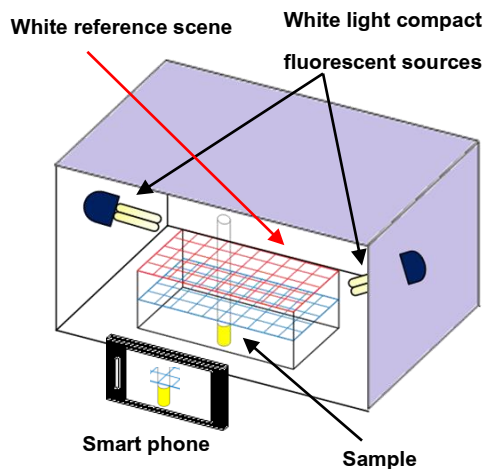


Figure 1 pH meter at develop on smart phone for estimating pH in solutions

Materials and Methods

Preparation of buffer solutions [13]

We prepare the acid buffer solution via mixed weak acid with salt of weak acid solution. Firstly, 5.834 ml of acetic acid (CH_3COOH) solution is dissolved in 1000 ml of DI water. In the meantime, 8.203 g of sodium acetate (CH_3COONa) powder is dissolved in 1000 ml of DI water. After that, prepare the base buffer solution via mixed weak base with salt of weak base solution. Prepare 14.196 g of disodium hydrogen phosphate (Na_2HPO_4) powder is dissolved in 1000 ml of DI water. And 13.799 g of sodium phosphate (NaH_2PO_4) powder is dissolved in 1000 ml of DI water. Mixing the solution of CH_3COOH and CH_3COONa then calibrate the pH to values 3.0, 3.5, 4.0, 4.5, 5.0. Mixed the solution of Na_2HPO_4 and

NaH₂PO₄ and then calibrate the pH to values 6.0, 6.5, 7.0, 7.5, 8.0, 8.5, 9.0 with 713 pH meter. [14]

Sample preparation

Brought the buffer prepared each of pH values put into a test tube 3 ml. After that, drops of indicator (For pH 3.0 – 9.0) into a test tube containing the solution pH values 0.3 ml in each tube. Vibrate the solution to combine. Figure 2 shows buffer solution

with each pH mixed with the indicator solution. It can be clearly observed that there is a color change. The pH 3.0 - 4.5 to pinkish dark red, pH 5.0 to dark orange, pH 5.5 to orange, pH 6.0 to yellow, pH 6.5 to light green, pH 7.0 to green and pH 7.5 – 9.0 to pinkish dark green.

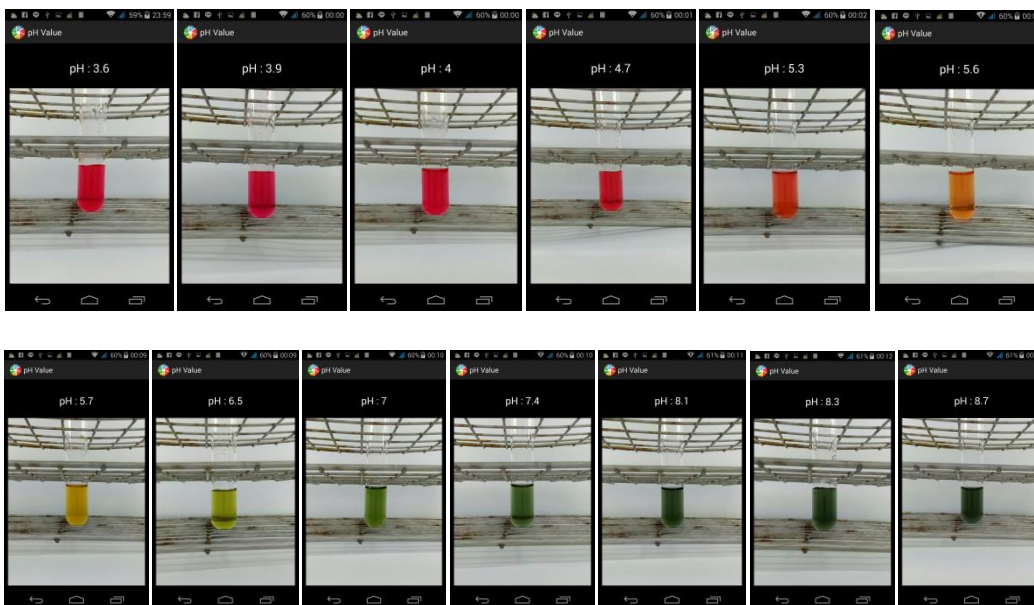


Figure 2 Buffer solution with each pH mixed with the indicator solution.

Experimental procedures

Setup

The experiments in laboratory as the Figure 1, our experimental setup is shown in Figure 3. Our smart phone is “Wiko Rigde” embedded with Android 4.4.2 operating system, a 13 MPixel digital camera, 2 GB of RAM, and a 1.4 GHz processing unit [15]. The application was written in Java by using eclipse for design [16 -19]. The sample put within a drapes box for prevent optical interference. The digital camera of this smart mobile phone has a measured 90° full field of view via drill for take a picture in the box. Inside the box, install two white light compact fluorescent lamps as the light source. Our cheap

uniformly white reference scene is a white A4 paper. The measured distance between the smart phone and the white reference paper is 26 cm and distance between the smart phone and test tube is 18 cm.

Within the screen consists of frame blue circle of 40 x 40 pixels is programmed will be shown on the screen of a smart phone to provide user can easily adjust the position and orientation of the smart phone in appearance that the test tube is properly fitted. Its purpose is to collect image data in red, green, and blue color planes for the solution under investigation. When pressed, the capture button will be recorded picture on the SD card in pH value folder. The pressed album will be the page album.

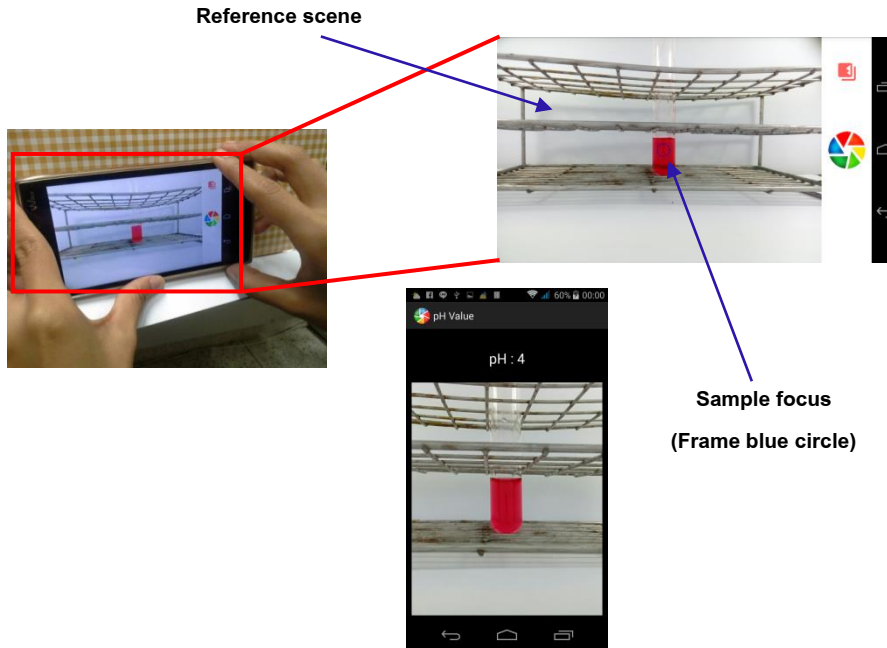


Figure 3 Overview of experimental demonstration.

Calibration and test

To calibrate the pHs, in this App, with 713 pH meter, the consequent pHs are measured from the different buffer solution, then the relativity between the Red values and pHs are plotted as shown in Figure 4. According to the Figure 4, when the pHs are increased the Red values inversely are rapidly decreased in range of pH 5.5 - 9.0.

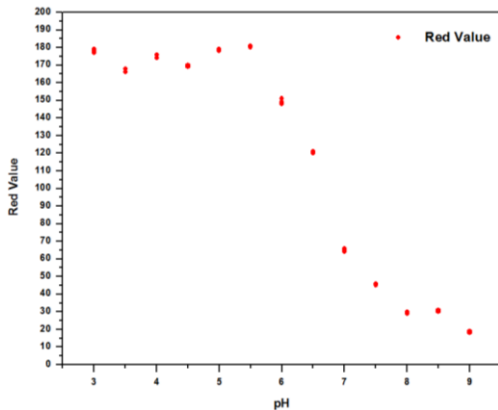


Figure 4 The relativity between Red value and pH.

The Figure 5 shows that the relativity between the Green values and the pH-values. In range of pH 3.0 - 6.5 the Green values are increased, but in range of pH 6.5 - 9.6 they are decreased.

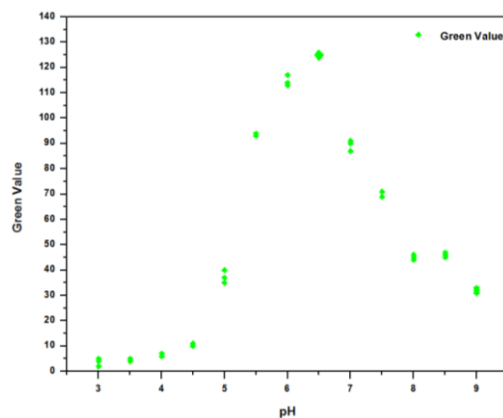


Figure 5 The relativity between Green value and pH.

The relativity between the Blue values and pH-values is unpredictable as shown in Figure 6.

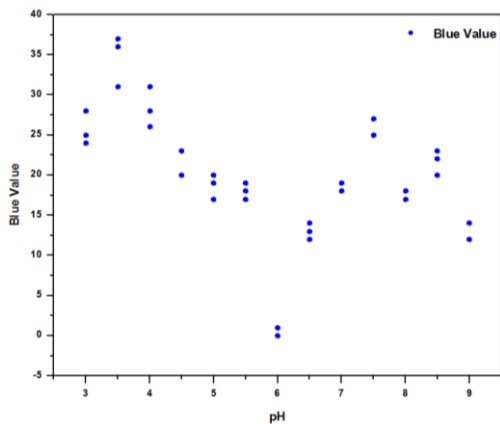


Figure 6 The relativity between Blue value and pH.

The relativity of the Red, Green and Blue value with pH showed that the Red and Green value is planes color indicative of a change in the pH range of are likely of course. Therefore it uses the Red value with pH of as decided to divide the relativity of pH with Green value are 2 case as shown on the Figure 7. Case 1, if Red value is greater than or equal to 140 we find that a three-parameter exponential function as

$$pH = e^{\left(1.78 - \frac{(4.97)}{(Green+4.82)}\right)} \quad (1)$$

Is mathematically fitted excellent ($R^2 = 93.60\%$) with our experimental data in the 3.0 – 6.0 pH range. Case 2, if Red value is less than 140 we find that a three-parameter exponential function as

$$pH = 4.62 \times e^{\left(\frac{(65.02)}{(Green+66.26)}\right)} \quad (2)$$

Is mathematically fitted excellent ($R^2 = 96.34\%$) with our experimental data in the 6.5 – 9.0 pH range.

Since the both above equations convert RGB and pH, so the equations added in the application. When the smart phones have ready for analyzing the pH solution. Once the smart phone finishes the analysis, the display of the smart phone shows the image of the test tube filled with acid or base solution. The amount of pH found is also highlighted as image in Figure 3. Prepared additional test sets of the above pH solutions and randomly putting each one of the whole test tube. We find that our smart phone can effectively analyze pH in the 4.0-8.0 with a measured

pH 0.05 standard deviation, 0.71% relative standard deviation (%RSD), limited color is caused by a chemical reaction between the indicators and buffer solution certain the colors that are very similar. The measured average analytical time is 2.4 s and the size of the application program is only 3.28 MB.

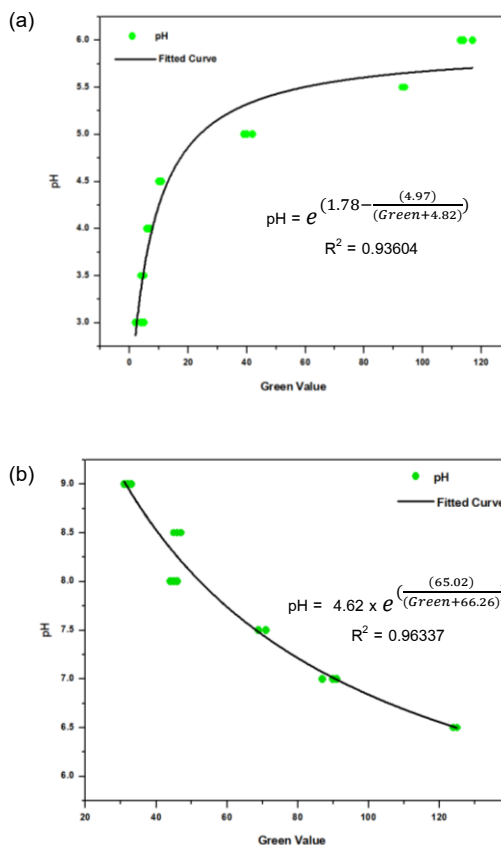


Figure 7 Relativity between the measured pH and Green value. (a) Red value is less than 140. (b) Red value is greater than or equal to 140

Conclusions

We developed and shown the smart phone can be functioned as a color analyzer for estimating the color of pH. Concept is to utilize the 2D detection from the digital camera of the smart phone by means of arranging both the reference scene and the test tube in such a way that they both fit in the camera's field of view. In this research, a smart phone is embedded

with our application program called “pH value” for analyzing the color buffer solution that mixing indicator for find pH value. We found that the Red and Green value affected change in color of the buffer solution at in pH values. Red value is less than 140 we find that pH 3.0 – 6.0 with accuracies 93.60% and Red value is greater than or equal to 140 we find pH 6.5 – 9.0 with accuracies 96.34%. Experimental procedures using a smart phone with an Android operating system, a white A4 paper, buffer solution and indicator shows a promising result in determining pH values in 4.0 – 8.0 with a measured pH 0.05 standard deviation, 0.71% relative standard deviation. Other features include low cost, portability and ease of operation and can be supplied through a marketing application. Furthermore compared to typical pH meter, it can be seen that our application has the ability to reset or customizable for other purposes as needed. The future work we plan to apply our application to real samples such as pH water in water sources naturally.

Acknowledgments

The study was supported from the Department of Physics, Faculty of Science, Ubon Ratchathani University, Glass Technology Excellent Center (GTEC) and Science Achievement Scholarship of Thailand (SAST).

References

- [1] Ecology and Environment Mahidol University. “The chemical properties of the water”, http://www.il.mahidol.ac.th/e-edia/ecology/chapter3/chapter3_water2.htm.
- [2] Alissara Kuprasit , Thailand Institute of Scientific and Technological Research. 2011. “Acid - base of soil”, <http://www.tistr.or.th/tistrblog/?p=1115>
- [3] The Institute for Innovation and Development of Learning Process - Mahidol University. 2007. “Indicator for acid – base”, <http://www.il.mahidol.ac.th/e-media/acid-base/C8.HTM>
- [4] Sudarat pennoo , Bansomdejchaopraya Rajabhat University. 2012. “Properties of acid – base”, <https://sites.google.com/site/smbatikhxngsaralalaykrdbes/3-kar-trwc-sxb-saralalay-krd-bes>.
- [5] Coastal fisheries research and development. 2003, Dec 23. “pH meter of water buying guide to suitable for applications and cost-effective”, <http://www.fisheries.go.th/cf-chan/visit-water-room/pH/pH-page.html>.
- [6] Science Tech Co., LTD. 2005. “pH Meter”, <http://www.sa.sciencetech.co.th/pdf/Micro.pdf>.
- [7] Bangkok high lab. “acid - base Meter and pH Meter is?”, <http://www.bangkokhighlab.com/ph-meter-what/>.
- [8] Athipluck Chotthanapaisit. 2014. “What is a smart phone, tablet and phablet different.” <http://news.siamphone.com/news-14121.html>.
- [9] Yuttana Intaravanne, Sarun Sumriddetchkajorn, Jiti Nukeawa. 2012. “Cell phone-based two-dimensional spectral analysis for banana ripeness estimation”. **Sensors and Actuators**. B168: 390–394.
- [10] Sarun Sumriddetchkajorn, Kosom Chaitavon, Yuttana Intaravanne. 2013. “Mobile device-based self-referencing colorimeter for monitoring chlorine concentration in water”. **Sensors and Actuators**. B182: 592–597.
- [11] Sarun Sumriddetchkajorn, Kosom Chaitavon, Yuttana Intaravanne. 2014. “Mobile-platform based colorimeter for monitoring chlorine concentration in water”. **Sensors and Actuators**. B191: 561–566.
- [12] Yuttana Intaravanne, Sarun Sumriddetchkajorn. 2015. “Android-based rice leaf color analyzer for estimating the needed amount of nitrogen fertilizer”. **Computers and Electronics in Agriculture**. 116: 228–233.

- [13] Department of Chemistry, Faculty of Science, Ubon Ratchathani University. 2014. **Chemistry Laboratory II.** Ubon ratchathani.
- [14] J. Frank, Ch. Buchmann. 1995. **pH Meter 713.** Herisau, Switzerland: The METROHM AG.
- [15] Wiko mobilie. 2015. "Ridge user guide", <http://data.wikomobile.com/documents/fichiers/bd954cc2dcf02d61164237ca235f9331.pdf>.
- [16] Chakchai So-In, Pongsathon Janyoi. 2011. **Basic Android App Development.** Nonthaburi : IDC Premier.
- [17] ThaiCreate.Com Team. 2003. "Android Tutorials – leaning android app free on smart phone". <http://www.thaicreate.com/mobile/android.html>
- [18] Promlert Lovichit. 2012. **Guide apps for Android beginners.** Bangkok: Provision.
- [19] Kobkiat Saraubon. 2013. **Develop App Android.** Bangkok: Media Network.

Determination of the Distribution Function of Spacing between Fibers of a Row of Parallel Cylindrical Fibers with Non-Uniform Spacing from its Hydraulic Permeability: Applications to Glomerular Filtration

N. Punyaratabandhu^{*} and P. Dechadilok

Department of Physics, Faculty of Science, Chulalongkorn University, Patumwan, Bangkok Thailand. 10330

^{*}E-mail: a.pong.bandhu@gmail.com

Abstract

In Nephrology, hydraulic permeability, the ratio between averaged fluid velocity and pressure difference, indicates renal filtration efficiency. The objective of this work is to determine the distribution function of spacing between adjacent cylinders of a row of parallel rigid cylinders from its hydraulic permeability and use it to determine the nanostructure of the epithelial slit of the glomerular capillary wall. The gap-width between adjacent fibers is assumed to follow the gamma function. The mean and standard deviation of the fiber spacing are found employing the Newton-Raphson method. The convergence of the Newton-Raphson scheme is achieved rapidly after a few iterations, yielding the same mean and standard deviation of the fiber spacing regardless of the initial input. The mean value of half-width of the gap between fibers of the slit diaphragm obtained from the Newton-Raphson method is compared with values reported from transmission electron microscopy and electron tomography.

Keywords: Epithelial slit, Glomerular capillary wall, Hydraulic permeability, nephrology, Renal filtration efficiency

Introduction

Blood ultrafiltration in glomerular capillaries is believed to be the first step of renal urine formation. The mammalian glomerular capillary has a unique structure consisting of several cellular layers. The filtrated fluid is transported from the capillary lumen to the Bowman's capsule by passing through the fenestrae of the endothelial cell layers, across the hydrogel known as the glomerular basement membrane (GBM), and through the slit diaphragm connecting the foot processes of the epithelial cells, as shown in the schematic drawing shown in Figure 1. It is therefore desired to relate the nanostructure of each layer to its contribution to fluid and solute transport restriction. Our work focuses on investigate

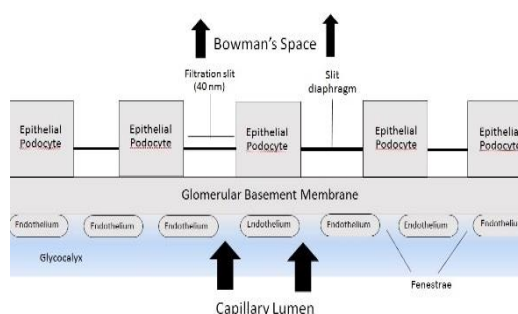


Figure 1 Schematic drawing of an ultrastructural model of the glomerular capillary wall introduced by Edwards and Deen [1, 2]. The arrows indicate the direction of fluid flow. Figure is not drawn to scale.

the hydraulic permeability and structure of the slit diaphragm.

The total glomerular hydraulic permeability (k), the averaged fluid velocity per unit pressure difference, is contributed by the hydraulic permeability of the three cellular layers as following (with the detailed derivation given in the appendix A):

$$\frac{1}{k} = \frac{1}{k_{en}} + \frac{1}{k_{GBM}} + \frac{1}{k_{ep}} \quad (1)$$

where k_{en} and k_{GBM} are the hydraulic permeability of the endothelial cell layer and the glomerular basement membrane, respectively. k_{ep} , the hydraulic permeability of the epithelial cell layer, is the product between the GBM surface fraction not covered by the podocytes (\mathcal{E}_s), and the averaged hydraulic permeability of the slit diaphragm, $\langle k_s \rangle$.

$$k_{ep} = \mathcal{E}_s \langle k_s \rangle \quad (2)$$

Embedded in equation (2) is an assumption that there is no transcellular flow. Images from electron microscopy [3] have shown the slit diaphragm to be a planar arrangement of fibers connecting the podocytes. Drumond and Deen [4] proposed having the slit diaphragm being a row of parallel cylinders. They also demonstrated that assuming the uniform spacing between fibers in the slit diaphragm cannot explain the profile of the solute sieving (the ratio between the solute concentration in primary urine and that in blood) as a function of solute sizes, suggesting that the gap-width between adjacent fibers of the epithelial slit is not uniform. They also proposed that the fiber spacing followed either the log-normal distribution or the gamma distribution since the value of these distribution functions became zero as the gap-width of the fiber spacing vanished or reached infinity. In our work, the gamma distribution is employed, and the mean and standard deviation of the fiber spacing, factors which are crucial to glomerular size-selectivity, is determined from the Newton-Raphson method, and compared with images from electron microscopy.

Materials and Methods

Model formulation

As aforementioned, the slit diaphragm in the epithelial cell layer of the glomerular capillary wall is modeled as a row of parallel fibers attached to parallel walls shown in Figure 2. u is the half-width of the gaps between adjacent fibers, whereas R is the fiber radius of the slit diaphragm. If $g(u)$ is the distribution function of the fiber spacing, an averaged velocity can be calculated using a following equation:

$$\langle V_s \rangle = \frac{\int_0^{\infty} (u + R)g(u)V_s du}{\int_0^{\infty} (u + R)g(u)du} \quad (3)$$

where $\langle V_s \rangle$ is an averaged fluid velocity. As defined in Figure 2, R is the fiber radius, and V_s is the fluid velocity in the slit channel. The distance between the centerlines of two adjacent fibers equals $u + R$.

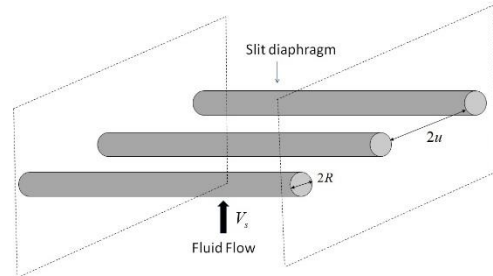


Figure 2 The slit diaphragm modeled as a row of parallel cylindrical fibers. V_s is the fluid velocity filtering through the slit diaphragm, and R is the fiber radius. u is the half-width of the spacing between adjacent fibers. Although not shown in the figure, u is assumed to be non-uniform with the distance between the centerlines of two adjacent fibers being $u+R$.

An averaged hydraulic permeability, a ratio between the averaged velocity and the pressure difference, can be written as following:

$$\langle k_s \rangle = \frac{\langle V_s \rangle}{(\Delta P)_s} = \frac{\int_0^{\infty} (u + R)g(u)V_s du}{(\Delta P)_s \int_0^{\infty} (u + R)g(u)du} \quad (4)$$

where $\langle k_s \rangle$ is an averaged hydraulic permeability and $(\Delta P)_s$ is the pressure drop across the epithelial slit. There exists previous calculation involving the relationship between the velocity, V_s , and the pressure drop, $(\Delta P)_s$, in a form of the dimensionless flow resistance, f_T , defined as

$$f_T = \frac{(u+R)(\Delta P)_s}{\eta V_s} \quad (5a)$$

η is the fluid viscosity. Combining equations (4) and (5a), the relationship between hydraulic permeability and dimensionless flow resistance becomes

$$\langle k_s \rangle = \frac{\int_0^\infty (u+R)^2 f_T^{-1}(u) g(u) du}{\eta \int_0^\infty (u+R) g(u) du} \quad (5b)$$

Once f_T is obtained, the distribution function, $g(u)$, can be determined from the averaged hydraulic permeability of the epithelial slit as discussed below.

Calculation of dimensionless flow resistance

The Reynolds number characterizing the filtration process through the glomerular capillary wall is known to be very low. Viscous dissipation dominates the system. We employed the formulation introduced by Drumond and Deen [4] where the dimensionless flow resistance, f_T , of the epithelial slit is

$$f_T = f + f_p \quad (6)$$

where f_p is the dimensionless flow resistance of a Poiseuille flow between parallel plates, whereas f is the dimensionless flow resistance of a flow past a row of parallel cylinders. In other words, the slit diaphragm is modeled as a row of parallel cylinders connecting two parallel walls (with the parallel walls being the simplification of the podocyte surfaces). The relationship between fluid velocity, V_s , and pressure drop, $(\Delta P)_s$, in equation (5a) of a flow past a row of parallel cylinders is obtained from solving the Stokes and continuity equations for a flow past a row of parallel cylinders by using the commercial finite

element package (COMSOL Multiphysics, Stockholm, Sweden). Our results agree very well with previous calculations by Drumond and Deen [8], and the lubrication approximation of Sangani and Acrivos [9], confirming the accuracy of the finite element solution.

Determination of the distribution function of fiber spacing from its hydraulic permeability

Following the formulation of Drumond and Deen [4], our assumption is that the distribution function of u , the half-width of the spacing between adjacent fibers of the slit diaphragm, follows the gamma distribution:

$$g(u) = \frac{\gamma_2^{\gamma_1} u^{\gamma_1-1} e^{-\gamma_2 u}}{\Gamma(\gamma_1)} \quad (7)$$

where γ_1 and γ_2 are both constants, and $\Gamma(\gamma_1)$ is the gamma function of γ_1 . The mean and variance of u , $\langle u \rangle$ and $\langle u^2 \rangle$, can be calculated from the values of γ_1 and γ_2 as shown below.

$$\langle u \rangle = \frac{\gamma_1}{\gamma_2} \quad (8a)$$

$$\langle u^2 \rangle = \frac{\gamma_1}{\gamma_2^2} \quad (8b)$$

The standard deviation of u is simply the square root of the variance given in equation (8b).

Once the dimensionless flow resistance is known, for a given value of γ_1 , γ_2 can be calculated from the averaged hydraulic permeability through the slit diaphragm, $\langle k_s \rangle$, by solving equation (5b) using the Newton-Raphson method, a very well-known numerical method employed in finding successively better approximation of the root of the equation. The Newton-Raphson scheme was written using MATLAB v. 2011b software (Mathwork, Netick, MA, USA). Once γ_1 and γ_2 are obtained, the distribution function of the gap half-width, $g(u)$, is known, and the mean and standard deviation of u can then be calculated from equation (8a) and the square root of the solution of equation (8b).

From the physiological observation, the fraction of GBM not covered by the podocytes, \mathcal{E}_s , is approximately 0.11 in rats [2]. If $\langle k_s \rangle = 114 \text{ nm/s/Pa}$, from equation (2), k_{ep} is, therefore, 12.5 nm/s/Pa. From the work of Deen et al. [2] using Darcy's Law and the conservation of mass, k_{GBM} was calculated to be approximately 3-9 nm/s/Pa. The contribution of the endothelial cell layer to the total hydraulic permeability, however, remains questioned, as the endothelial cell layers consists of circular fenestra filled with multiple protein fibers and cross-linked chains of unknown concentration. If we are to assume that the concentration of protein fibers in the fenestrae is low such that the endothelial fenestrae can be modeled as short liquid-filled cylindrical pores, k_{en} has been calculated to be around $2 \times 10^{-7} \text{ nm/s/Pa}$ [2]. Substituting k_{ep} , the averaged k_{GBM} of the range shown above, and k_{en} into equation (1) shows that k is about 3.7nm/s/Pa which falls into the range of the total glomerular hydraulic permeability obtained from micropuncture experiments that is approximately 3-5 nm/s/Pa for rats. Therefore, in our calculation, $\langle k_s \rangle$ is set at 114 nm/s/Pa Pa at 37°C.

Results and discussion

Results obtained from this numerical scheme are shown below in Figures 3 and 4 where values of γ_2 and the mean value of fiber gap half-width, $\langle u \rangle$, are plotted as a function of numbers of iterations, respectively. The results are shown for $\langle k_s \rangle = 114 \text{ nm/s/Pa}$. The epithelial slit fiber radius, R , is estimated from images from electron tomography [3] and assumed to be 4.5 nm. As shown in the figures, convergence of the Newton-Raphson method is achieved after a few iterations, reaching the same values of the mean and standard deviation of fiber spacing of the epithelial slit regardless of the initial guess for γ_2 , denoted below in the figures as γ_{20} . For $\gamma_{20} = 2, 3, 4, 7, 8$ and 9 nm^{-1} , the final solution

for γ_2 is always 5.40 nm^{-1} for as illustrated in Figure 3, always yielding the mean value of the half-width of gap between adjacent fibers in the epithelial slit, $\langle u \rangle$, at 2.06 nm as shown in Figure 4.

In addition, the standard deviation of the gap half-width can also be obtained from substituting γ_1 and γ_2 calculated using the Newton-Raphson method shown in Figure 4 into equation (8b). The result is shown in Figure 5 where the standard deviation of u is plotted as a function of the number of iterations. Regardless of the initial guess for γ_2 , the standard deviation of u always converge to 0.62 nm. Convergence of the Newton-Raphson scheme is achieved after a few iterations, and the final solution for γ_2 remains the same regardless of input values of γ_{20} .

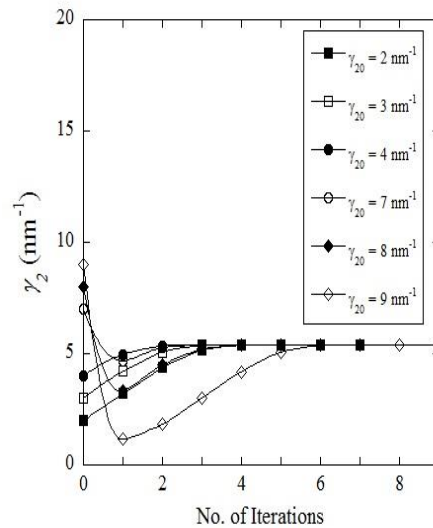


Figure 3 the parameter γ_2 of the gamma distribution (as shown in equation (7)) as a function of number of iterations. γ_{20} are initial guesses for γ_2 . $\gamma_1 = 11.11$. $\langle k_s \rangle = 114 \text{ nm/s/Pa}$ at 37°C.

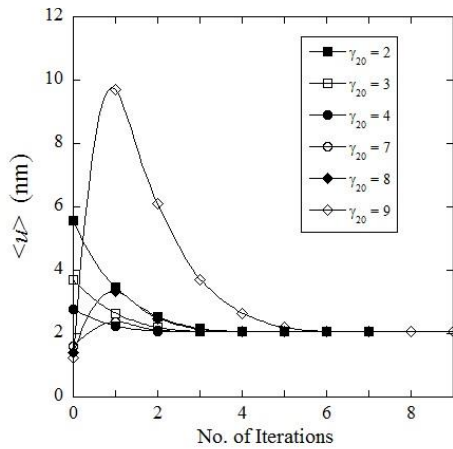


Figure 4 $\langle u \rangle$, the mean value of the fiber spacing half-width, as a function of number of iterations. γ_{20} is the initial guess for γ_2 . $\gamma_1 = 11.1$. $\langle k_s \rangle = 114$ nm/s/Pa at 37°C.

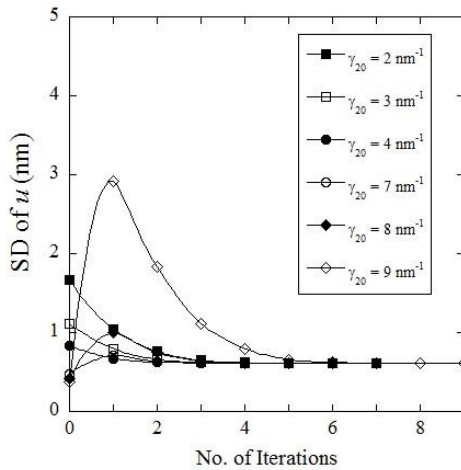


Figure 5 the standard deviation of the half-width of the gap between adjacent fibers of the slit diaphragm as a function of number of iterations. γ_{20} is the initial guess for γ_2 . $\gamma_1 = 11.1$. $\langle k_s \rangle = 114$ nm/s/Pa at 37°C.

For a given value of γ_1 , the Newton-Raphson method yields a value of γ_2 that gives the desired value of $\langle k_s \rangle$. Shown in Figure 6 is the distribution,

$g(u)$, that yields k_s at 114 nm/s/Pa for $\gamma_1 = 2, 4$ and 11.1. For different values of γ_1 , the obtained γ_2 and $g(u)$ are different, resulting in different values of the mean and standard deviations of u as shown in the figure. When $\gamma_1 = 2$ and 4, $\langle u \rangle$ is 1.67 and 1.88 nm, respectively. With $\gamma_1 = 11.1$, $\langle u \rangle = 2.06$ nm which agrees well with the observation of Rodewald and Karnovsky [6] from transmission electron microscopy (TEM) that reports the size of u at 2 nm. It also agrees with the tomography results of Wartiovaara et al. [3]. Among the values of γ_1 , $\gamma_1 = 11.1$ yields the closest mean value of fiber spacing to that reported from TEM and electron tomography.

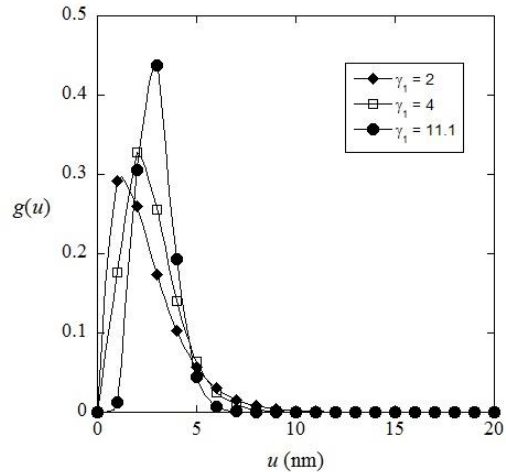


Figure 6 the distribution function, $g(u)$, of the half-width of the gap between adjacent fibers of the slit diaphragm as a function of u . $\gamma_1 = 2, 4$ and 11.1. $\langle k_s \rangle = 114$ nm/s/Pa at 37°C.

Conclusions

The slit diaphragm is modeled as a row of parallel fibers with spacing between adjacent fibers following the gamma distribution. The Newton-Raphson scheme converges rapidly, always yielding the same final distribution function. If the restriction on fluid transport of the endothelial cell layer is

assumed to be much less than those of the GBM and the epithelial cell layer, the results from the Newton-Raphson method yields a mean value of fiber spacing that is very close to results reported by Rodewald and Karnovsky as well as those obtained from tomography with the total glomerular hydraulic permeability falling into the range obtained from micropuncture experiments. Directions of our future work include investigating the relationship between the change in the nanostructure of the slit diaphragm and the change in solute-sieving and size-selectivity of glomerular capillary wall in order to find the distribution function of spacing between fibers capable of yielding both the appropriate hydraulic permeability and solute sieving.

Acknowledgments

His Royal Highness Crown Prince Maha Vajiralongkorn Scholarship from the Graduate School, Chulalongkorn University to commemorate the 72nd anniversary of his Majesty King Bhumibala Aduladeja is gratefully acknowledged. Financial supports from the Faculty of Science (A1B1), and Chulalongkorn University (New Faculty Member Grant, Ratchadapiseksompote Fund) are greatly appreciated.

Appendix: Total hydraulic permeability of glomerular capillary wall and contributions of the three cellular layers

The total hydraulic permeability of glomerular capillary wall is the averaged fluid velocity ($\langle V \rangle$) per unit pressure difference (ΔP). Their relationship can be written as following.

$$\Delta P = \left(\frac{1}{k}\right) \langle V \rangle \tag{A1}$$

Likewise, the hydraulic permeability of each cellular layer is the ratio between the averaged fluid velocity through that layer and the pressure drop across that cellular layer, and the relationship between the fluid

velocity and the pressure drop across the cellular layer are shown below.

$$\Delta P_{en} = \left(\frac{1}{k_{en}}\right) \langle V_{en} \rangle \tag{A2}$$

$$\Delta P_{GBM} = \left(\frac{1}{k_{GBM}}\right) \langle V_{GBM} \rangle \tag{A3}$$

$$\Delta P_{ep} = \left(\frac{1}{k_{ep}}\right) \langle V_{ep} \rangle \tag{A4}$$

where ΔP_{en} , ΔP_{GBM} and ΔP_{ep} are the pressure difference across the endothelial cell layer, the GBM and the epithelial cell layer, respectively. $\langle V_{en} \rangle$, $\langle V_{GBM} \rangle$ and $\langle V_{ep} \rangle$ are the averaged fluid velocity through the endothelial cell layer, the GBM and the epithelial cell layer, respectively.

The total pressure drop across the glomerular capillary wall is the sum of ΔP_{en} , ΔP_{GBM} and ΔP_{ep} . From conservation of mass, the averaged fluid velocity, $\langle V \rangle$, must equal to the averaged fluid velocity of each successive cellular layer; $\langle V_{en} \rangle$, $\langle V_{GBM} \rangle$ and $\langle V_{ep} \rangle$. Combining equations (A1)-(A4), we obtain

$$\Delta P = \left(\frac{1}{k_{en}} + \frac{1}{k_{GBM}} + \frac{1}{k_{ep}} \right) \langle V \rangle \tag{A5}$$

Therefore, the contributions to k from k_{en} , k_{GBM} and k_{ep} are as shown in equation (1) in the introduction.

References

- [1] Edwards, A., Daniels, B.S., and Deen, W.M., 1999. "Ultrastructural model for size selectivity in glomerular filtration". **Am J Physiol Renal Physiol.** 276: F892-F902.
- [2] Deen, W.M., Lazzara, M.J., and Myers, B.D. 2001. "Structural determinants of glomerular permeability". **Am J Physiol Renal Physiol.** 281: 579-596.
- [3] Wartiovaara, J., et al. 2004. "Nephrin strands contribute to a porous slit diaphragm scaffold as revealed by electron tomography". **The Journal of Clinical Investigation.** 114: 1475-1483.

- [4] Drumond, M.C., and Deen, W.M. 1995. "Hindered transport of macromolecules through a single row of cylinders: applications to glomerular filtration". **Journal of Biomechanical Engineering**. 117: 414-422.
- [5] Dechadilok, P., et al. Transport of spherical particles through fibrous media and a row of parallel cylinders with applications in glomerular filtration. In Preparation.
- [6] Rodewald, R., and Karnovsky, M.J. 1974. "Porous substructure of the glomerular slit diaphragm in the rat and mouse". **J Cell Biol**. 60: 423–433.
- [7] Squarer, A., et al. 1998. "Mechanisms of progressive glomerular injury in membranous nephropathy". **J Am Soc Nephrol**. 9:1389–1398.
- [8] Drumond, M.C., and Deen, W.M. 1994. "Stokes flow through a row of cylinders between parallel walls: model for the glomerular slit diaphragm". **Journal of Biomechanical Engineering**. 116:184-189.
- [9] Sangani, A.S., and Acrivos, A. 1982. "Slow flow past periodic arrays of cylinders with application to heat transfer". **Int. J. Multiphase Flow**. 8: 193-206.

Effects of Sintering Temperature on Physical Properties of Chitosan/Hydroxyapatite Composites

C. Boonpratum, P. Limsuwan and K. Naemchanthara*

Department of Physics, Faculty of Science, King Mongkut's University of Technology Thonburi,
126 Pracha-Uthit Rd., Bangmod, Thung Khru, Bangkok, 10140, Thailand

*E-mail: puri_kit@hotmail.com

Abstract

The chitosan/hydroxyapatite (CS/HA) composites were prepared from hydroxyapatite synthesized from chicken eggshells and chitosan of shrimp. The composites were added chitosan with different concentration from 1 to 15 g and sintered at various temperature from 200 to 1200°C with an increment 100°C. The crystal structure, function group, morphology and thermal behavior of composites were investigated by X-ray diffractometer (XRD), Fourier transform infrared spectroscopy (FTIR), field-emission scanning electron microscopy (FESEM) and thermogravimetric analyses (TGA), respectively. The results showed that the crystalline of composite was increased with increasing temperature. The porous of composites were appeared after sintered at 300°C due to decomposed of chitosan. The number and size of pore was depended on amount of chitosan. The results of this research indicated that the sintering temperature could be produced porous on chitosan/hydroxyapatite composites.

Keywords : Chitosan, Eggshells, Hydroxyapatite, Precipitation

Introduction

Hydroxyapatite (HA, $\text{Ca}_{10}(\text{PO}_4)_6(\text{OH})_2$) is an interesting biomaterial that the properties as same the mineral phase of bone such as biocompatibility, bioactive, non-toxicity, non-inflammatory and non-immunogenicity [1,2]. However, it has low mechanical properties such as brittleness, hardness and difficult to casting [3]. Therefore, some authors were interested that natural polymers compensate the weak mechanical points of HA [4,5]. Among all the natural polymers, chitosan (CS), a deacetylated product of chitin, is a widely polymers for improve mechanical properties due to CS possesses biodegradable, biocompatible, antibacterial, flexible and adhesive [6-8].

In this study, CS/HA composites were synthesized from chicken eggshells and added various chitosan concentration from 1 to 15 g by precipitation method and sintered at various temperature from 200 to 1200°C. The crystal structure, function group,

morphology and thermal behavior of composites were investigated by X-ray diffractometer (XRD), Fourier transform infrared spectroscopy (FTIR), field-emission scanning electron microscopy (FESEM) and thermogravimetric analyses (TGA), respectively.

Materials and Methods

Materials

Chitosan was exacted from shrimp shells by chemical technique, deacetylation degree 87.5%. The chicken eggshells were obtained from King Mongkut's University of Technology Thonburi canteen. Diammonium hydrogen orthophosphate ($(\text{NH}_4)_2\text{HPO}_4$), ammonia solution and nitric acid were purchased from Sigma-Aldrich Company, USA.

Preparation of CS/HA composites

The calcium oxide (CaO) was prepared from chicken eggshells. The method of preparation started

from removed the membranes of chicken eggshells, washed with distill water and dried in the air for two days. The chicken eggshells were ground into powder and heated at 1300°C for 4 h. Initially $\text{Ca}(\text{NO}_3)_2$ was prepared by mixing CaO powder with nitric acid (HNO_3) and adjusted pH 12 with ammonia solution while the chitosan solution at the different weight from 1 to 15 g were dissolved into 300 ml 1% (v/v) acetic acid aqueous solution, stirred until good homogenization. The powder of $((\text{NH}_4)_2\text{HPO}_4)$ was dissolved into 200 ml deionized water and mixed with the chitosan solution. The pH of the gel solution was adjusted to 12 with ammonia solution. Afterward the solution was dropped into stirred calcium nitrate solution, stirred in the air for 24 h and kept in room temperature for one day. The precipitation of solution was washed with distill water until the precipitation was pH about 7, filter with filter membrane and annealed at 65°C in the air for 48 h. The CS/HA composites were grinded with agate mortar into powder. Sample of this experiment consist of 1, 5, 9, 15 g of chitosan which are named as CS1/HA, CS5/HA, CS9/HA and CS15/HA, respectively. Finally, all sample were sintered at various temperature from 200 to 1200°C for 4 h with a sintering rate 10°C/min.

Forming of CS/HA composites

The CS/HA composites were prepared by 1 g of CS/HA powder was compressed to pellets with high pressure hydraulic in 3000 psi. After that the pellets were sintered at 400°C for 4 h and sintered again at 1200°C for 4 h.

Characterization

Powder X-ray diffraction (XRD) of raw chitosan, hydroxyapatite and CS/HA composites at different concentration were measured by a Philips X'Pert PW3020 diffractometer using $\text{CuK}\alpha$ radiation ($\lambda=1.5406 \text{ \AA}$) with 30 mA, 30 kV. Infrared spectra were measured in the range 4000-400 cm^{-1} using a Fourier transform infrared spectrometer (FTIR; Perkin Elmer Spectrum Two) 16 scans and spectral solution

of 2 cm^{-1} . The thermogravimetric analysis (TGA; Perkin Elmer TGA7) was measured in the range between 75 to 800°C with a heating rate of 10°C/min. The morphology and microstructure of CS/HA composites were observed by field-emission scanning electron microscopy (FEI SEM; Nova NanoSEM 450). The compressive strength of CS/HA composites were measured by universal testing machine (LR5KPlus Series).

Results and Discussion

XRD analysis

Figure 1 shows the crystal structure phase of CS, HA and CS/HA composites at different concentration were investigated via XRD. The peak at 2theta 19.8 (C) represent CS in agreement to Lima et al. [9]. The peak at 2theta 25.87, 31.95, 39.81, 46.71 and 49.46 (H) represent the crystallinity of HA. All of the XRD patterns of HA and CS/HA were identified according JCPDS file no.09-0432. The average crystallite sizes of the HA and CS/HA were approximately between 55 to 70 Å. [10]. Moreover, the result indicated that the concentration of CS increase did not change the crystallographic structure of HA.

Figure 2 shows the crystal structure phase of CS15/HA composites at difference temperature.

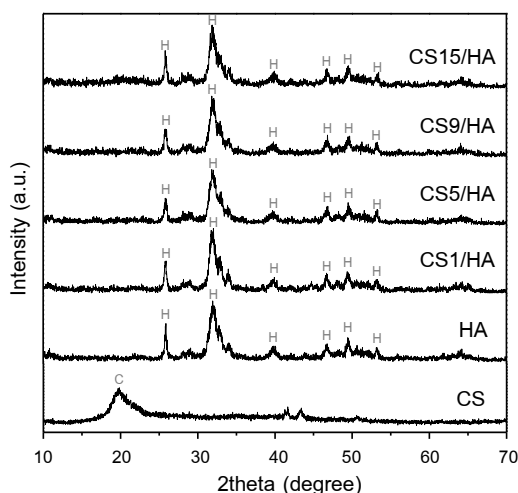


Figure 1 The XRD patterns of CS, HA and CS/HA composites synthesized at different concentration.

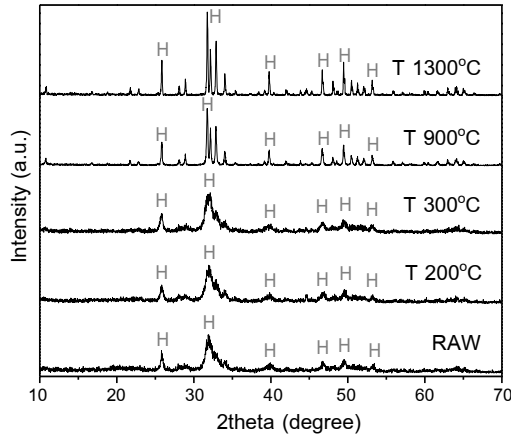


Figure 2 The XRD patterns of CS15/HA composites sintered at different temperature.

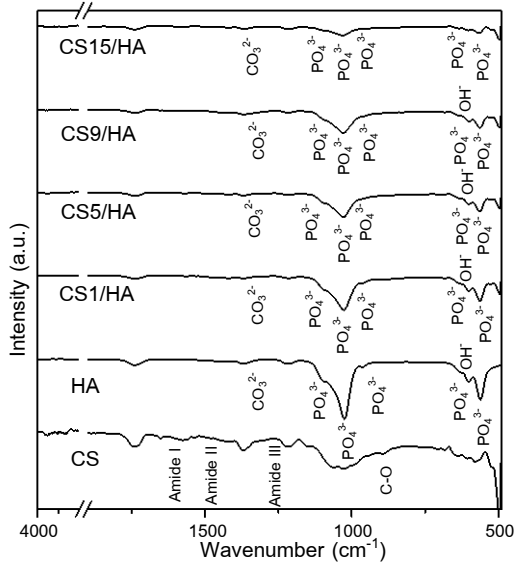


Figure 3 The FTIR spectra of CS, HA, and CS/HA composites synthesized at different concentration.

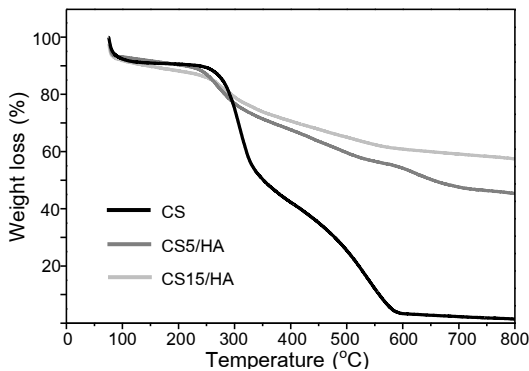


Figure 4 The TGA thermograms of CS, CS5/HA and CS15/HA

The result indicated that the crystallinity of HA increase with increasing sintering temperature.

FTIR analysis

The FTIR spectra of CS, HA and CS/HA at different concentration was presented in Figure 3. The CS presents transmission bands at 1654 (amide I), 1562 (amide II), 1366, 1220 (amide III), 1026 and 896 cm^{-1} (C-O) in agreement to Kong et al. [11]. The characteristic spectra of pure HA presents transmission bands for the phosphate group at 1096, 1040, 962, 598 and 568 cm^{-1} for the carbonate group at 1380 cm^{-1} and for the hydroxyl group at 632 cm^{-1} in agreement to Gonzalez et al. [12]. The result indicated that the crystal of HA and CS/HA composites contained carbonate. Carbonate was probably synthesized from CO_2 at atmosphere when $\text{Ca}(\text{NO}_3)_2$ decompose into Ca^{2+} and 2NO_3^- . The reaction take place with adsorption and absorption of CO_2 become to calcite of CaCO_3 . Furthermore, the intensity of phosphate group decrease with increasing weight of CS.

TGA analysis

Figure 4 shows the TGA thermogravimetric curves of CS and CS/HA at different concentration were obtained in order to investigate a material's thermal behavior. The TG curves have two parts for all sample: the first part between 75 to 156.8 $^{\circ}\text{C}$ that can be assigned to evaporation of the water molecules [9]. The second part between 156.8 to 800 $^{\circ}\text{C}$ that can be assigned to thermal decomposition of organic macromolecules. The chitosan began to degrade around 245 $^{\circ}\text{C}$ and decompose completely around 600 $^{\circ}\text{C}$. The weight loss of CS5/HA and CS15/HA were 62% and 45%, respectively. Moreover, by using TGA analysis it was possible to calculate the CS concentration in CS/HA composites by comparing the different of the total weight loss.

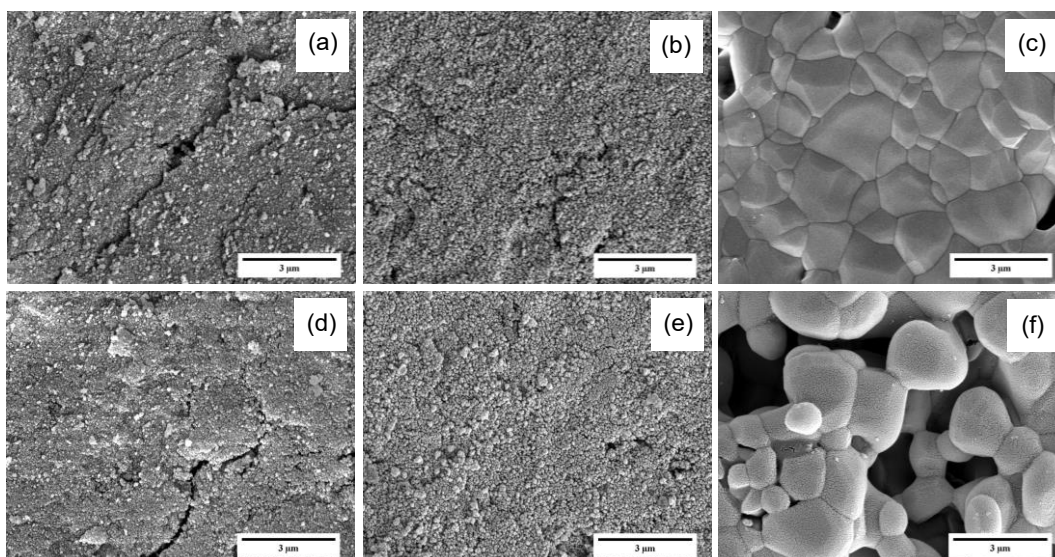


Figure 5 The SEM images of CS1/HA composites (a) pre-sintering and post-sintering at (b) 600°C and (c) 1200°C and CS9/HA composites (d) pre-sintering and post-sintering at (e) 600°C and (f) 1200°C.

Morphology analysis

Figure 5 shows the FESEM images of CS1/HA and CS9/HA composites pre- and post-sintering at 600 and 1200°C. For pre-sintering, the SEM images of CS1/HA and CS9/HA show the same morphology that the spherical small particles and tightly agglomerated. The average sizes of the CS1/HA and CS9/HA were approximately 44.95 and 60.85 nm, respectively. For post-sintering at 600°C, the size and shapes of particles exhibited same morphology that the spherical small particles and the average size were approximately 52.23 and 61.50 nm, respectively. The result indicated that the size and dispersion of particles had different no significant at the various concentration of chitosan. For post-sintering at 1200°C, the morphology melted become to grains. The grain size of CS1/HA and CS9/HA were approximately 0.3 to 4.65 µm. The porosity increased with increasing CS concentration due to effect of degradation of CS polymer.

Mechanical properties

Figure 6 shows the compressive strengths of HA and CS/HA scaffolds at different concentration and temperature. The compressive strength increased from

3.5 to 18.2 MPa with increasing CS concentration from 1 to 15 g. For post-sintering at 1200°C, the compressive strength of HA and CS/HA scaffolds various CS concentration at 1, 5, 9 and 15g were approximately 54.6, 334.6, 104.3, 80.32 and 65 MPa, respectively. The result indicated that the CS1/HA was highest compressive strength but the compressive strength decreased with increasing CS concentration more than 1 g due to the porosity of the scaffolds composites were increased corresponding to FESEM results.

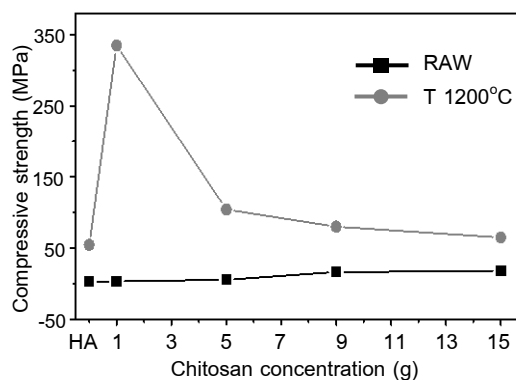


Figure 6 The compressive strengths of HA and CS/HA composites synthesized at different concentration

Conclusions

The CS/HA composites with various concentration of chitosan were successfully synthesized by precipitation method from waste chicken eggshells. The results of this research indicated that the concentration of CS increase did not change the crystallographic structure of HA. The size and dispersion of particles had different no significant at the various concentration of chitosan. The crystallinity of HA increase with increasing sintering temperature. Moreover, the CS can improve mechanical properties and the sintering temperature can be produced porous on CS/HA composites.

Acknowledgments

The authors acknowledge the support given to this work by Faculty of Science, King Mongkut's University of Technology Thonburi. The authors would like to sincere thanks to Kasertsart University provided Thermogravimetric analysis for experiment.

References

- [1] Khaled, R.M., Hanan, H.B., and Zenab, M.E. 2014. "In vitro study of nano-hydroxyapatite/chitosan-gelatin composites for bio-applications". **J ADV RES.** 5: 201-208.
- [2] Khaled, R.M., Zenab, M.E., and Aida, A.S. 2011. "In vitro properties of nano-hydroxyapatite/chitosan biocomposites". **CERAM INT.** 37: 3265-3271.
- [3] Nikpour, M. R., Rabiee, S. M., and Jahanshahi, M. 2012. "Synthesis and characterization of hydroxyapatite/chitosan nanocomposite materials for medical engineering applications". **COMPOS PART B-ENG.** 43: 1881-1886.
- [4] Xing, L., KaiHui, N., Shuai, S., and Hao, C. 2012. "Preparation and characterization of nano-hydroxyapatite/ chitosan cross-linking composite membrane intended for tissue engineering". **INT J BIOL MACROMOL.** 50: 43-49.
- [5] Isamu, Y., Shunsuke, I., Akiyoshi, O., Hideki, M., and Junzo, T. 2003. "The effect of citric acid addition on chitosan/hydroxyapatite composites". **COLLOID SURFACE A.** 214: 111-118.
- [6] Hebeish, A.A., Ramadan, M.A., Montaser, A.S., and Ahmed, M.F. 2014. "Preparation, characterization and antibacterial activity of chitosan-g-poly acrylonitrile/silver nanocomposite". **INT J BIOL MACROMOL.** 68: 178-184.
- [7] Fatemeh, H., Mohammad, E.B., Daryoosh, V., and Lobat, T. 2015. "In situ preparation of iron oxide nanoparticles in natural hydroxyapatite/chitosan matrix for bone tissue engineering application". **CERAM INT.** 41: 3094-3100.
- [8] Lei, S., Lu, G., Yan-Feng, X., Yao, W., Fang, W., and Zhong-Wei, G. 2011. "Antibacterial hydroxyapatite/chitosan complex coatings with superior osteoblastic cell response". **MATER LETT.** 65: 974-977.
- [9] Leite Lima, P.A., Cristiane, X.R., Gloria, A.S., Karine, A., and Luis, E.A. 2013. "Preparation, characterization and biological test of 3D-scaffolds based on chitosan, fibroin and hydroxyapatite for bone tissue engineering". **MAT SCI ENG C MATER.** 33: 3389-3395.
- [10] Chalongwut, B., Pichet, L., Ekachai, H., Weeranut, K., and Kittisakchai, N. 2015. "Preparation and Characterization Chitosan/Hydroxyapatite Composites from Waste for Bio-applications". Proceeding of Siam Physics Congress 2015. pp. 67-70.
- [11] Jilie, K., and Shaoning, Y. 2007. "Fourier Transform Infrared Spectroscopic Analysis of Protein Secondary Structures". **ACTA BIOCH BIOPH SIN.** 39: 549-559.
- [12] Gonzalez, G., Sagarzazu, A., and Villalba, R. 2006. "Mechanochemical transformation of mixtures of Ca(OH)₂ and (NH₄)₂HPO₄ or P₂O₅". **MATER RES BULL.** 41: 1902-1916.

Measurement of Sucrose Content in Solution using UV-Vis Spectroscopy

J. Sanguansuttigul*, K. Thamaphat and P. Limsuwan

Green Synthesis and Application Laboratory, Applied Science and Engineering for Social Solution,
 Department of Physics, Faculty of Science, King Mongkut's University of Technology Thonburi, Bangmod,
 Thungkru, Bangkok 10140

*E-mail: zhedew19@gmail.com

Abstract

In food, beverage, and sugar production processes, one of the most important control parameters required in the product quality control is sucrose content or named as Brix percentage. Several methods have been developed to measure the Brix percentage. The UV-Vis spectroscopy is an alternative method to analysis sucrose content in solution due to its easy and simple. Based on Beer-Lambert law, the results showed that the highest absorption peak of sucrose solution was observed at approximately 197 nm associated with σ to π^* electronic transition of carbon in sucrose molecule. The absorbance at this UVC wavelength increased with increasing sucrose content. The quantitative analysis can be obtained by plotting a standard curve of absorbance versus Brix percentage. The results achieved in this work can be used to develop a low cost portable device for sucrose measurement using UVC lamp and photodiode as a light source and detector, respectively.

Keywords : % Brix, Sucrose concentration, Beer-Lambert law, UV-Vis Spectroscopy

Introduction

Sugar is an essential component in plants, fruits, vegetables and all living organisms, where they have structural, cryoprotective and metabolism roles. In commercial usage the term of sugar usually refers to sucrose. It plays a dominant role in food processing, agriculture, as well as in international economics and politics. There are many plants from which sucrose is commercially extracted such as the date palm, sorghum (*Sorghum vulgare*), sugar maple (*Acer saccharum*), carob, locust bean, and recognizably, sugarcane (*Saccharum officinarum*) and sugar beet (*Beta vulgaris*) are the most widen sources [1]. Sugarcane is an important crop in many countries including Thailand. It produces cane sugar which can be commonly classified into five types based on the international sugar market: raw sugar, refined sugar, plantation white sugar, brown sugar, and soft brown sugar [2-4]. In sugar production process, each type of sugar has to

satisfy rigorous quality demands which apparently address to sucrose content indicating to sugar purity. Therefore, sucrose content is one of the most important figure for the procedure and the refiner. The percentage by weight of sucrose in a pure sugar solution is measured in Degree Brix unit.

The classical method most widely used for determination of the sucrose content is refractometry based on refractive index measurement. Many kinds of refractometer are developed for measuring % Brix such as Abbé refractometer, hand refractometer, dipping refractometer, and automatic refractometer [4]. However, modern instrumental methods such as gas chromatography, electrochemical method, infrared spectroscopy, ultrasound and high-performance liquid chromatography have been continuous employed for analysis of sucrose content [5-8]. Although these methods have been successfully applied to analysis,

the high cost of acquisition and maintenance are still problems. For that reason, the accurate, simplicity, and low-cost measurement of percent % Brix is needed.

UV-Vis spectroscopy is one of the most common techniques used in routine analysis and the development of analysis method using UV-Vis spectroscopy is always of interest because does not imply additional cost or the acquisition of new equipment. Nowadays, the UV-Vis spectroscopy is applied in differentiation of the agricultural, and food and beverage products such as tea, wine and coffee [9-11]. In this paper, an alternative economic portable device based on the UV-Vis spectroscopy for the sucrose content measurement is developed and proposed.

Materials and Methods

The sucrose solution with different concentrations; 1, 3, 5, 7, 10, 20, 30, and 50 %w/v was prepared by dissolving sucrose powder obtained from Ajax UNIVAR in deionized water. The UV-Vis absorption of all sucrose solutions were studied by UV-Vis spectrophotometer (Perkin, Lambda35). The absorption spectrum was recorded in the range of 190-800 nm. Then, the absorption intensity in UV-Vis wavelength range was observed. The wavelength that shows an obvious light absorption intensity difference at different sucrose concentrations was determined. This wavelength was used to define the light source and photodetector type of % Brix meter. The % Brix portable meter proposed herein was constructed from materials that cost-effective and easy to find in local market.

Results and Discussion

The absorbance spectra of sucrose solution with different concentrations recorded in the range 190 – 800 nm was shown in Figure 1. Experimental measurements were made in terms of absorbance (A), which is defined as:

$$A = -\log T = \log \frac{P_0}{P} = abc \quad (1)$$

When
 A is Absorbance (a.u.),
 T is Transmittance,
 P₀ is corrected incident radiation energy,
 P is radiation power,
 a is absorptivity (l/(g·cm)),
 b is path length (m), and
 C is solution of concentration (mol/l).

The intensity of the light passing through the sample cell is also measured for that wavelength - given the symbol, P. If P is less than P₀, the sucrose solution has absorbed some of the light (neglecting reflection of light off the cuvette surface). The absorbance of a transition depends on two external assumptions. The first absorbance is directly proportional to the concentration (C) of the sucrose solution used in the experiment and the second is directly proportional to the length of the light path (b), which is equal to the width of the cuvette [12]. In Figure 1, the absorbance in the range of 190 – 400 nm is associated with the σ to π* electronic transition of carbon in sucrose molecule as shown in Figure 2. As can be seen, the highest absorbance in UVC at 197 nm.

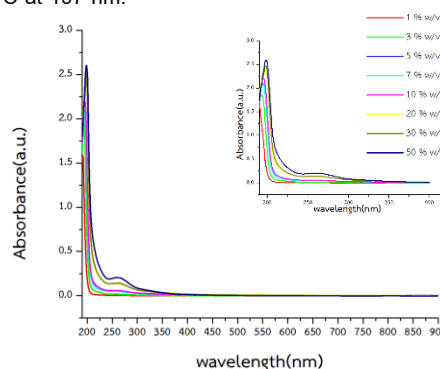


Figure 1 UV – Visible absorption spectra of sucrose solutions with different concentrations.

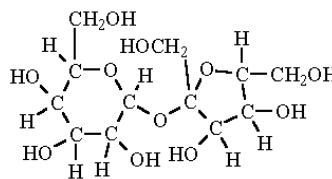


Figure 2 Molecular structure of sucrose.

In order to develop a low cost portable device for sucrose measurement, a UVC lamp (Aqua, G16T5) with a peak wavelength at 257 nm was therefore selected as a light source. It is low cost and available in local market. A photodiode (SgLux, SG01S-C18) that responds wavelength from 221 to 358 nm was used as detector. The components diagram and layout of portable device for sucrose measurement were shown in Figure 3.

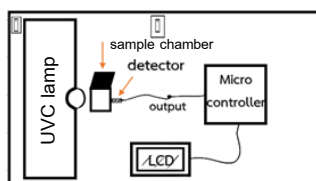


Figure 3 Diagram shows the components and layout of portable device.

The schematic of voltage sensor was shown in Figure 4. Power supplied to the circuit was a 5 V DC source. The output signal from amplifier chip LMC6001 was transferred to a microcontroller, PIC16F819. The microcontroller, which was programmed by C language, transformed output voltage and displayed the measured value of % Brix on LCD.

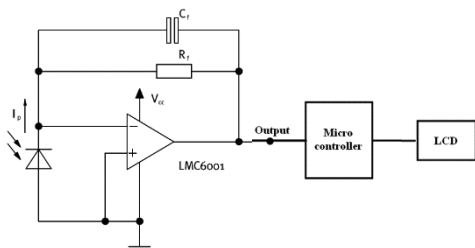


Figure 4 Voltage sensor schematic.

The calibration curve is shown in Figure 5. The relation between output voltage and % Brix showed the linearity of R^2 (coefficient of determination) = 0.9985, and low variability for three repetitive measurements. So this portable device has developed for sucrose measurement which can measure % Brix in the range of 0 - 50 % Brix.

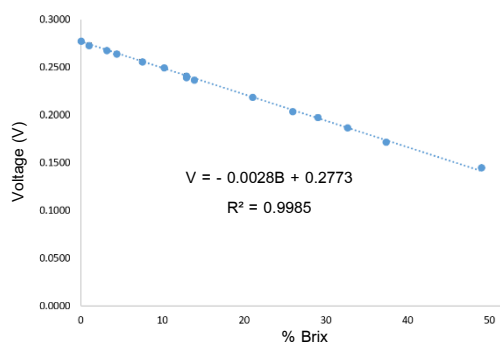


Figure 5 Detector output voltage and solution sweetness.

A developed portable device for measurement of %Brix solution using UV Light was shown in Figure 6.

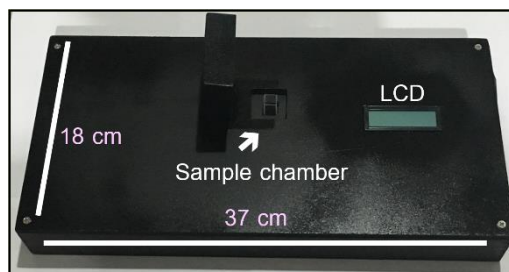


Figure 6 Portable device for measurement of %Brix solution.

Conclusions

UV-Vis spectrophotometry is an alternative to measurement of %Brix solution using UV Light. This principle can be used to develop a low cost and efficient portable device for measurement of sucrose content in sugar production process, food and beverage.

Acknowledgments

The authors would like to thank the Faculty of Science, King Mongkut's University of Technology Thonburi for the financial support.

References

- [1] Caballero, B., Trugo, L.C. and Finglas, P.M. 2003. **Encyclopedia of Food Sciences and Nutrition**. Vol. 9, 2nd ed., Amsterdam: Academic Press.
- [2] Worsfold, P., Townshend, A. and Poole, C. 1995. **Encyclopedia of Analytical Science**. London: Academic Press.
- [3] Pennington, N.L. and Baker, C.W. 1990. **Sugar: A User's Guide to Sucrose**. New York: VNR.
- [4] Chen, C.P. and Chou, C.C. 1993. **Sugar Handbook: A Manual for Cane Sugar Manufacturers and Their Chemists**. New York: Wiley.
- [5] Rodriguez-Saona, L.E., Fry, F.S., McLaughlin, M.A. and Calvey, E.M. 2001. "Rapid analysis of sugars in fruit juices by FT-NIR spectroscopy". **Carbohydr Res.** 336: 63-74.
- [6] Shanmugavelan, P., Kim, S.Y., Kim, J.B., Kim, H.W., Cho, S.M., Kim, S.N., Kim, S.Y., Cho, Y.S. and Kim, H.R. 2013. "Evaluation of sugar content and composition in commonly consumed Korean vegetables, fruits, cereals, seed plants, and leaves by HPLC-ELSD". **Carbohydr Res.** 380: 112-117.
- [7] Rambla, F.J., Garrigues, S. and de la Guardia, M. 1997. "PLS-NIR determination of total sugar, glucose, fructose and sucrose in aqueous solutions of fruit juices". **Anal Chim Acta.** 344: 41-53.
- [8] Jan, M.V.S., Guarini, M., Guesalaga, A., Pérez-Correa, J.R. and Vargas, Y. 2008. "Ultrasound based measurements of sugar and ethanol concentrations in hydroalcoholic solutions". **Food Control.** 19: 31-35.
- [9] Palacios-Morillo, A., Alcázar, A., de Pablos, F. and Jurado, J.M. 2013. "Differentiation of tea varieties using UV-Vis spectra and pattern recognition techniques". **Spectrochim Acta A.** 103: 79-83.
- [10] Casale, M., Oliveri, P., Armanino, C., Lanteri, S. and Forina, M. 2010. "NIR and UV-vis spectroscopy, artificial nose and tongue: Comparison of our fingerprint techniques for the characterization of Italian red wines". **Anal Chim Acta.** 668: 143-148.
- [11] Souto, U.T.C.P., et al. 2010. "UV-Vis spectrometric classification coffees by SPALDA". **Food Chem.** 119: 368-371.
- [12] Clark J., 2007, **The Beer-Lambert Law** [Online], Available : http://chemwiki.ucdavis.edu/Core/Physical_Chemistry/Spectroscopy/Electronic_Spectroscopy/Electronic_Spectroscopy_Basics/The_Beer-Lambert_Law#The_Absorbance_of_a_Solution.html [2016, June 06].

Determination of Damped Harmonic Oscillation through Woltenhofen's Pendulum

A. Malaithong, K. Thamaphat and W. Liewrian*

Physics Learning Innovation Group, Department of Physics, Faculty of Science, King Mongkut's University of Technology

Thonburi, Bangmod, Thungkru, Bangkok 10140, Thailand

E-mail: * watchara.liewrian@mail.kmutt.ac.th

Abstract

A simple demonstration set for investigating the damping effect of Waltenhofen's eddy current pendulum was developed in this work. The demonstration set composes of a metal plate moving through a magnetic field. The magnetic field was generated by applying a DC current to two solenoid coils. The influences of the magnetic field strength, the material type and the pendulum length of metal plate on the damping effect were studied. The results showed that the chaotic motion of pendulum occurred at a low magnetic field and the damping action increased with increasing the magnetic field strength. The material type and the length of metal plate influenced on the decay behavior of the damped oscillation. The heavier weight and low resistance of metal plate have higher angular momentum and resulted on the slower pendulum decay. This demonstration set, which is an example of magnetic brake system, can be applied for the contribution on physics teaching as science, technology, engineering and mathematics (STEM) education in high school. It can improve students' knowledge on the magnetic induction and the damping oscillation.

Keywords: Waltenhofen's pendulum, Damped harmonic oscillation, Electromagnetic induction

Introduction

For Thailand education in the 21st century, student is faced with rapidly changing and all information is not limited to just around us anymore, just click on the fingertips. Education around the world are moving away from the style of teaching that teachers are central to learning in a new paradigm. Consequently, both teachers and students should seek self-knowledge through real action because actual knowledge into enduring understanding rather than rote learning [1,2]. The STEM education is a way of learning that help students to develop skills of science, technology, engineering and mathematics on their own through the integrated learning and teachers must give students the experience of taking the actual test together with a description using the knowledge from previous

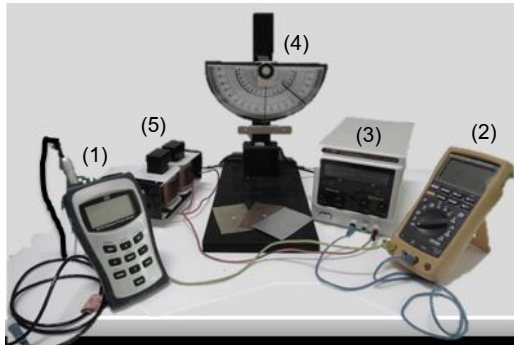
experience as called PBL (Project-Based Learning). Typically, teacher use virtual experiment for mimicking realistic experiment because the effective experimental setup is usually expensive and time-consuming. By using hands-on activity and doing it themselves, this setup help students practice and deepen their understanding of the principles and theories of Physics more. This model also inspire students to be creative and leads to more innovation in the future [3].

For teaching basic physics in topics about simple harmonic motion and electromagnetic, the students still cannot apply the knowledge these two links and integrate that leads to the damped harmonic motion. The school has a shortage of equipment such trials. The researcher created a set of learning about damped harmonic motion and study of magnetic field effect

when the metal plate have difference length and size explain that by Faraday's Law and Lenz's Law [4].

Experimental details

The experimental set is shown in Figure1. A semi-circle used to measure the angle when the plate swing. Apply direct current (D.C.) power supply APS3005s input current 0.0 - 0.6 A and measuring the electric current by multimeter Fluke 189. For using the metal plates, there are three types that consist of aluminum, copper and brass of size 5 x 10 cm², 5 x 12 cm² and 5 x 14 cm². With applying Tesla meter, we can measure magnetic field distribution in copper coils that is the set for creating a magnetic field contains an iron core and two coils.



(a)



(b)

(c)

Figure 1 (a) A demonstration setup for magnetic-damped pendulum (1.Tesla-meter 2. Multimeter 3. Power supply 4. Copper coils 5. Waltenhofen's pendulum)
(b) The part of creating magnetic field can be separated into components and compose is to make easy to portable, (c) show position with scales for measuring the distribution of the magnetic field in the area core.

To study nature of the pendulum motion with magnetic damping, we have to track the position of the

motion of the metal plates and then we compare with the motion of metal plate three type when the plate moving through a magnetic field set. For study effect of size and type of material on the motion of the plates when it moving through a magnetic field, we set aluminum, copper and brass size 5 x 10 cm², 5 x 12 cm² and 5 x 14 cm². We control magnetic intensity by adjusting the voltage gradually increasing validity of 0.0 - 0.6 A. and track the movement of the metal plate with a video camera. To analysis the time dependence of angular displacement by using Tracker software version 4.2. Because the initial angle of each measurement are not constant, we use normalize method to make it easy to analysis data.

Results and Discussion

For measuring the magnetic field distribution in the magnetic core, we found that the pattern of the magnetic field look like the bell curve that the magnetic field is gradually increase at -X axis area and gradually decrease at +X area and high magnetic field is at X = -2 to X = 2 as shown in Figure 2. From the graph we found the position at (X,Y) = 0,0 is the highest magnetic field distribution.

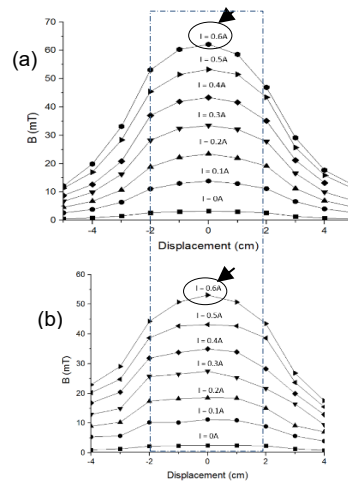


Figure 2 The magnetic field distribution (a) in X axis and (b) in Y axis versus displacement

The pendulum with damping has a general solution is

$$\theta(t) = \theta_0 e^{-\gamma t} \cos(\omega_1 t + \phi) \quad (1)$$

Where

ω_1 = frequency of the damp oscillation (Hz)

ϕ = Phase constant (radian)

γ = Damping term

The angular displacement results of each metal as shown in Figure 3 was found that aluminum plate move to equilibrium position fastest due to it has less mass ,but brass and copper with same mass where damping behavior is similar. When we consider effect of resistance, we found that for aluminum, its damping is higher than brass and copper and in this reason, we should analysis more detail of specific aluminum. In Figure 4, magnetic intensity of the aluminum is proportional to retarding force which is considered at the low magnetic intensity. Applying very low magnetic field to the pendulum, the effect of air resistance is more than magnetic damping and it makes angle swing gradual decrease slowly. If we apply the high magnetic field into the metal plate that magnetic damping is more than air resistance that make angle swing reduced gradually quickly such as angular displacement of the plate under $B = 48.68$ mT.

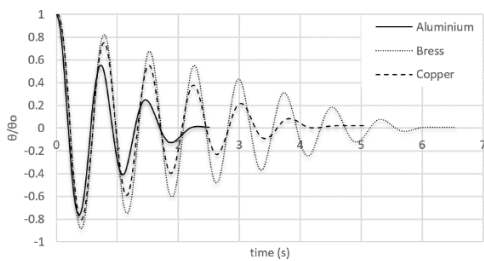


Figure 3 This graph shows relation of θ/θ_0 with time for the damped harmonic motion for each type of metal plate.

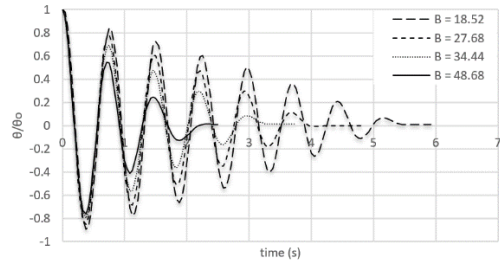


Figure 4 This graph shows relation of θ/θ_0 with time for the damped harmonic motion of aluminum. At $B = 0$ mT metal plate moves under air resistance, but at $B > 0$ mT it moves under magnetic force.

In this case can be described by using Equation 1, we focus on only the positive amplitude that is relation between $\frac{\theta(t)}{\theta_0}$ and $e^{-\gamma t}$ as shown in Figure 5(a).

$$\frac{\theta(t)}{\theta_0} = e^{-\gamma t} \cos(\omega_1 t + \phi) \quad (2)$$

$$\ln \frac{\theta(t)}{\theta_0} = \ln(e^{-\gamma t})(1) = -\gamma t \quad (3)$$

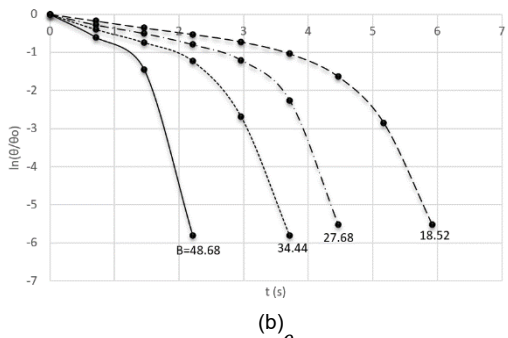
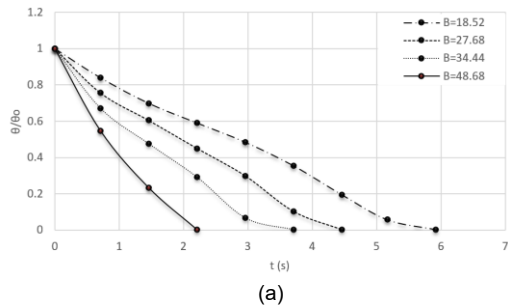


Figure 5 (a) The graph shows peak of θ/θ_0 with time for the damped harmonic motion in this case we consider specific positive amplitude. (b) The graph shows relation of $\ln \theta/\theta_0$ with time for the damped harmonic motion specific positive amplitude.

After taking natural log both sides of the equation will get the result is shown in Figure 5(b). At the initial time of the motion will be based on conditions γ_{Air} to be more than γ_B the metal plate moving slow due to influence of air resistance. For long time ago, the plate move slow due to the influence of magnetic force than air resistance and oscillation is rapidly decrease at high magnetic field. To investigate the effect of damping, the magnetic field is less that almost no damped motion but it start at $B=18.52$ mT and damped increasing when magnetic field increases (magnetic field proportional to damping term) is shown in Figure 5.

When consider difference size of metal plate found aluminum size 5×10 cm² moves to equilibrium position fastest as shown in Figure 6.

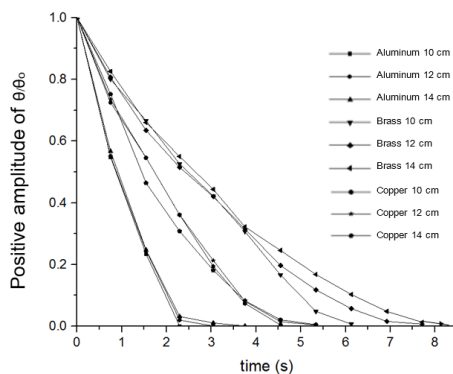


Figure 6 The relation of θ/θ_0 with time for the damped harmonic motion specific positive amplitude for each type metal plate.

Conclusions

At the initial time the metal plate is damped due to air resistance. For long time, the effect of damping increases the angle of swing that is gradually reduced. In this reason, the plate is underdamped pendulum motion. This experimental set can be used to demonstrate electromagnetic and damped harmonic oscillation concepts in physics class by STEM education.

Acknowledgments

The authors would like to thank you Faculty of Science of King Mongkut's University of Technology Thonburi, Bangkok Thailand and Satrinonthaburi School .

References

- [1] M.E. Bacon and D.D. Nguyen, 2005, "Real-world damping of a physical pendulum, **European Journal Of Physics**, Vol. 26 , pp. 651–655
- [2] J. Poonyawatpornkul and P. Wattanakasiwich, 2013, "High-speed video analysis of damped harmonic motion", **Physics Educations**, Vol. 48, No. 5, pp.782-789.
- [3] R. Yager, 2015, "The Role of Exploration in the Classroom (STEM)", **Springer**, Vol.52, pp.210–218.
- [4] Y. Xie, M. Fang and K. Shauman, 2015, "STEM Education", **Annual Review of Sociology**, Vol.41, pp. 331–357.

Synthesis and Characterization of Calcium Oxide as Catalyst for Biodiesel Production

J. Inthanont¹, P. Limsuwan¹, W. Kaewwiset², K. Wanthong¹ and K. Naemchanthara^{1*}

¹Department of Physics, Faculty of Science, King Mongkut's University of Technology Thonburi,
126 Pracha-Uthit Rd., Bangmod, Trungkru, Bangkok, 10140, Thailand

²Department of Physics, Faculty of Liberal Arts and Science, Kasetsart University, Kamphaeng Saen Campus,
1 Malaiman Rd., Kamphaeng Saen, Kamphaeng Saen Nakhon Prathom, 73140, Thailand

*E-mail: puri_kit@hotmail.com

Abstract

The catalyzer for biodiesel production in this work was prepared from cockle shell. The cockle shell was heated in the air at different temperature from 200 to 1300 °C for 4 h. The cockle shell before and after heated was characterized by X-ray diffraction (XRD) and Fourier transform infrared spectroscopy (FTIR). Nuclear magnetic resonance spectroscopy (NMR) was used to determine yield of biodiesel from cockle catalyze. The results shown that the natural phase of cockle shell was aragonite phase and changed to calcite phase after heated at 400 °C. The calcite phase of cockle shell was completely transformed to calcium oxide (CaO) after heated at 900 °C. The yield of biodiesel from CaO from cockle shell after heated at 1100 to 1300 °C had higher than other were compered. The results from this research indicated that the CaO from cockle shell could be used as a catalyst for biodiesel production.

Keywords: Biodiesel, Catalyst, Cockle shell, Transesterification

Introduction

Nowadays, the quantitative to use diesel fuel is increasing each year while source of natural fuel is rapidly decrease. Biodiesel, one of choice is interest to use instead diesel fuel and a mixture of fatty acid alkyl ester produce by the transesterification of vegetable oil or animal fats with nano-alkyl alcohols [1]. The transesterification reaction is produce low yield of biodiesel and long term to reaction. The researcher is interesting to development yield of biodiesel by using catalyst such as base, acid and enzyme catalyst [2]. For base catalysts, it is the most famous because of friendly environment and low temperature synthesis. Heterogeneous base catalyst is easily separate from the reaction mixture by filtration and then reuse [3]. Calcium oxide (CaO) is one of popular, found in natural

and produce from waste shell that compose of calcium carbonate (CaCO₃) such as coral, rock, eggshell and sea shell. In this work, the cockle shell was used catalyst for transesterification of biodiesel. The cockle shell powder was heated at various temperature to study crystal structure by X-ray diffraction (XRD). Each heated cockle shell at various temperature was catalyzed in biodiesel production and investigated yield of biodiesel by Fourier transform infrared (FTIR) spectroscopy and nuclear magnetic resonance (NMR) spectroscopy and compared with commercial biodiesel.

Materials and Methods

Material

The cockle shells were collected from Jatujak market, Bangkok, Thailand. Methanol was perched

from Sigma- Aldrich Company, USA. Palm oil was obtained from Morakot Industries, public company limited, Samut Prakarn, Thailand.

Method

The cockle shells were thoroughly washed with distills water and dried at room temperature for 2 days. The cockle shells were grounded into powder and calcined at different temperature from 200 to 1300 °C with heating rate of 10 °C /min for 4 h. The catalyst from cockle shells were kept in desiccator to prevent contact with air. The phase of the prepared catalyst was characterized by X-ray diffraction (XRD) using Cu K α radiation over a 2 θ range from 20 to 80°. The conversion of palm oil to biodiesel was performed in a volumetric flask. The volumetric flask soaked in the glycerin and warmed with hotplate at 65 °C. Transesterification reaction of palm oil, methanol and catalyst were added in volumetric flask under atmospheric pressure at 65 °C for 3 h while stirring at 700 rpm. The solution was centrifuged at 3,000 rpm for 15 min and filtered biodiesel on the top of the centrifuge tube. The properties of synthesized biodiesel were investigated by Fourier transform infrared spectroscopy (FTIR, Perkin Elmer (spectra two)) at a spectral range of 4000-500 cm⁻¹. The yields of synthesized biodiesel were characterized via nuclear magnetic resonance spectroscopy (NMR) with a Bruker Advance-II (400 MHz) spectrometer. The properties and yield of biodiesel from cockle shell catalyst were compared with commercial biodiesel.

Results and Discussion

Phase structure of catalyzer

The powder cockle shells were pre and post annealed at different temperature and characterized the crystal structure by XRD as results shown in Figure 1. The XRD pattern of cockle shell pre-annealed was appeared at 2theta 26, 27, 31, 33, 36, 37, 38, 41, 42, 45, 48, 50, 52 and 53 that assignment the pure aragonite phase of calcium carbonate and corresponded with JCPDS file no. 75-2230. The

aragonite phase of cockle shell was not changed after annealed at 200 °C. The poste annealed at 300 °C, the cockle shell was occurred the new sharp peak at 2theta 27 but stilled small peak of aragonite. The new peak was corresponded with the calcite phase (JCPDS file no. 72-1937) of calcium carbonate. After annealed 400 to 600 °C, the powder cockle shell was not detected aragonite phase but shown pure calcite phase. The XRD pattern of powder cockle shell was appeared a small peak at 2theta 37 after annealed at 700 °C and increased intensity with increasing temperature accorded with the JCPDS file no. 70-0649 of calcium oxide phase. At 800 °C, the XRD pattern was shown pure calcium oxide and continue until cockle powder annealed at 1300 °C. From the XRD result indicated that the powder cockle shell was completely transformed to calcite and calcium oxide after annealed at 400 and 800 °C, respectively. Phase transformation of calcite to calcium oxide is following as equation [1].

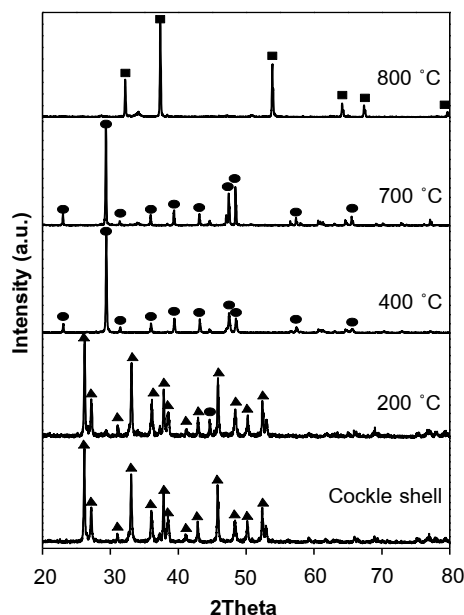


Figure 1 XRD pattern of before and after cockle shell different temperature (▲ : JCPDs 75-2230, ● : JCPDS 72-1937, and ■ : JCPDS 70-0649)

Function groups of biodiesel

From the XRD result, the powder cockle shell was used as catalyst in production biodiesel from palm oil must be calcium oxide. Then, the powder cockle shell after annealed at 800 to 1300 °C was selected for these experiments. The palm oil and biodiesel from powder cockle shell catalyst and commercial were investigated by FTIR as shown in Figure 2. The most common used FTIR analysis is free fatty acid determination, since free fatty acid content is critical parameter in the conversion of palm oil to methyl esters [4]. From the FTIR spectra, the band regions 1435, 1374 and 1196 cm^{-1} were stretched of methyl ester function groups [5]. The biodiesel from cockle shell catalyst annealed 800 to 1300 °C have function groups similarly biodiesel from commercial. The band regions and function groups of all samples were summarized as shown in Table 1. The yield of biodiesel from cockle shell catalyst annealed at different temperature was calculated by NMR technique.

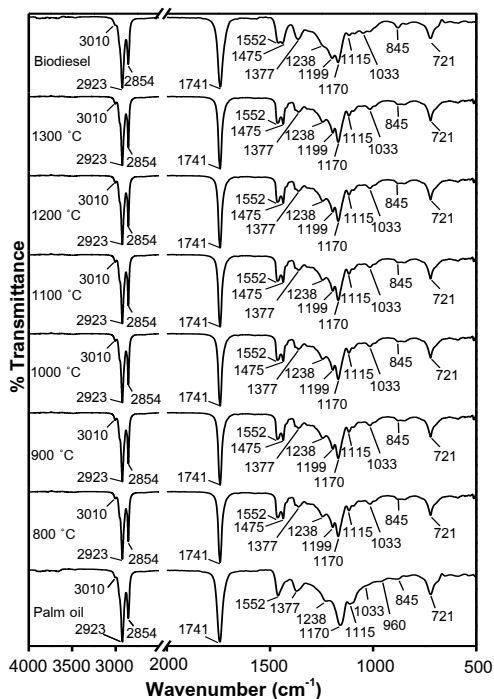


Figure 2 FTIR spectra of palm oil, biodiesel from palm oil using cockle shell catalyst and commercial

Table 1 Comparison of function groups of palm oil, biodiesel from palm oil using cockle shell catalyst and commercial

Wavenumber (cm^{-1})	Palm oil	Biodiesel synthesis	Biodiesel
3010	C-H	C-H	C-H
2800-3000	C-H ₂	C-H ₂	C-H ₂
1741	C=O	C=O	C=O
1464	C-H ₂	C-H ₂	C-H ₂
1435	-	C-H ₂	C-H ₂
1377	C-H ₃	C-H ₃	C-H ₃
1238	C-O	C-O	C-O
1196	-	C-O	C-O
1167	C-O-C	C-O-C	C-O-C
1117	C-O	C-O	C-O
1000-1100	-	C-O	C-O
960	C-H	-	-
700-900	C-H ₂	C-H ₂	C-H ₂

Yield of biodiesel

The biodiesel from commercial and cockle shell catalyst annealed at various temperatures were measured by NMR spectroscopy as shown in Figure 3. The peak in the range of 1.0 to 3.0 ppm in the proton spectra of biodiesel and palm oil were due to the proton of hydrocarbon chain [6]. The unsaturated protons in fatty acid methyl ester as well as in palm oil were appeared at 5.4 ppm [7]. On the other hand, at the peak 3.7 ppm was due to the $-\text{OCH}_3$ proton support the formation of biodiesel after transesterification reaction of palm oil [8]. The proton NMR spectra could be used to quantify of biodiesel formed during the transesterification [9] and presented in Table 2. From the NMR result indicated that the yield of biodiesel from cockle shells all the temperature has different value not significant. Then, the calcium oxide from cockle shell could be used a catalyst in production biodiesel through transesterification of palm oil.

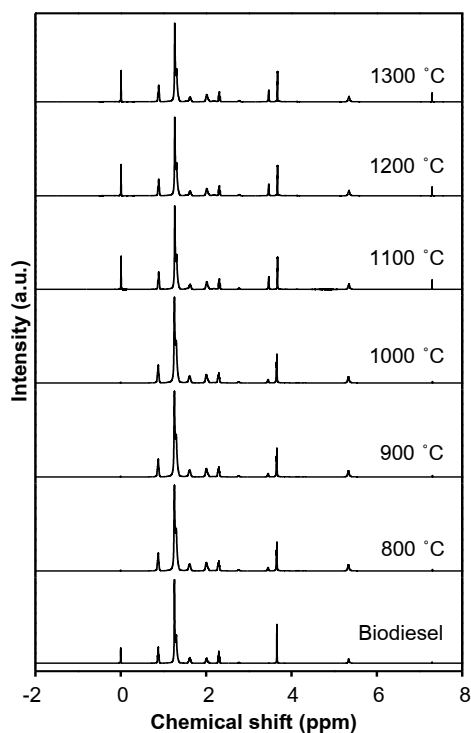


Figure 3 NMR spectra of biodiesel from palm oil using heated cockle shell at different temperature catalyst and commercial

Table 2 The yield of biodiesel using cockle shell catalyst annealed at different temperature

Type of biodiesel	The yield of biodiesel (%)
• Biodiesel commercial	97.97
• Biodiesel synthesized with cockle shell as catalyst	
800 °C	92.88
900 °C	92.01
1000 °C	92.98
1100 °C	94.70
1200 °C	95.54
1300 °C	94.92

Conclusions

The natural phase of cockle shell was aragonite phase of calcium carbonate and changed to calcite phase after heated at 400 °C. The powder cockle shell was heated at 800 up to 1300 °C that completely transformed to calcium oxide. The powder cockle after

heated at various temperature were used as a catalyst for production biodiesel of palm oil. The yield of biodiesel of cockle shell heated at various had more than 90% and different no significant. From this experiment indicated that the calcium oxide from cockle shell could be used a catalyst in production biodiesel through transesterification of palm oil.

Acknowledgments

The authors gratefully acknowledge the support given to this work by Faculty of Science, King Mongkut's University of Technology Thonburi, and Kasetsart University to provided tools for experiment.

References

- [1] Jian-Xun, W., Kung-Tung, C., Bi-Zhou, W., Yi-Hsien, B. L., and Chiing-Chang, C. 2012. "Transesterification of soybean oil to biodiesel using cement as a solid catalyst". **J Taiwan Chem Eng.** 43: 215-219.
- [2] Thawatchai, M., Sibudjing, K., and Chi-Hwa, W. 2015. "Biomass gasification ash as a source of CaO catalyst for biodiesel production via transesterification palm oil". **Energy Convers Manage.** 92: 234-243.
- [3] Boro, J., Thakur, A. J., and Deha, D. 2011. "Solid oxide derived from waste shell of turbonilla striatula as a renewable catalyst for biodiesel production". **Fuel Process Technol.** 92: 2061-2067.
- [4] Loh, K. S., Choo, N. Y., Cheng, F. S., and Ma, N. A. 2006. "Recovery and conversion of palm olein- derived used Frying oil to methyl for biodiesel". **J Oil Palm Res.** 18: 247-252.
- [5] Wei-Bo, Z. 2012. "Review on analysis of biodiesel with infrared spectroscopy". **Renew Sustainable Energy Rev.** 16: 6048-6058.
- [6] Muhammad, T., Saqib, A., Fiaz, A., Mushtaq, A., Muhammad, Z., Nasir, K., and Mir, K. A. 2011. "Identification, FT-IR, NMR (¹H and ¹³C) and GC/MS studies of fatty acid methyl esters in

biodiesel from rocket seed oil". **Fuel Process**

Technol. 92: 336-341.

[7] Zahoor, U., Mohamad, A. B., and Zakaria, M. 2014.

"Characterization of waste palm cooking oil for biodiesel production". **Int J Chem Eng Appl.** 5: 134-137.

[8] Adewale, A., Paul, O. A., and Rotimi, A. O. 2014.

"Hura crepitans seed oil: an alternative feedstock for biodiesel production". **J Fuels.** 1: 1-8.

[9] Priyanka, C., Venkat, R., John, G. V., Tong, W.,

and David, G. O. 2009. "Thermogravimetric quantification of biodiesel produce via alkali catalyzed transesterification of soybean oil". **Energy Fuels.** 23: 989-992.

Temperature effect on Zinc Substituted Hydroxyapatite Investigated by XRD, FTIR and FESEM Technique

C. Paikaew¹, P. Limsuwan¹, W. Kaewwiset² and K. Naemchanthara^{1*}

¹Department of Physics, Faculty of Science, King Mongkut's University of Technology Thonburi,
126 Pracha-Uthit Rd., Bangmod, Trungkru, Bangkok, 10140, Thailand

²Department of Physics, Faculty of Liberal Arts and Science, Kasetsart University,
Kamphaeng Saen Campus, 1 Malaiman Rd., Kamphaeng Saen,
Kamphaeng Saen Nakhon Prathom, 73140, Thailand

*E-mail: puri_kit@hotmail.com

Abstract

The aim of this work is investigate characteristic of zinc substituted hydroxyapatite after heat treatment. Zinc substituted hydroxyapatite was synthesized from calcium oxide (CaO) of waste eggshell by precipitation method. The concentration of zinc nitrate was substituted hydroxyapatite at various from 1 to 25 %wt. The zinc substituted hydroxyapatite was heated at different temperature from 200 to 1300 °C with an increment of 100 °C. The crystal structure, function group and morphology of sample were analyzed by X-ray diffraction (XRD), Fourier transform infrared spectroscopy (FTIR) and scanning electron microscopy, respectively. The XRD results show that the zinc substituted hydroxyapatite was hexagonal phase after heated from 200 to 800 °C. The hydroxyapatite phase of zinc substituted hydroxyapatite was changed to zinc containing β -tricalcium phosphate phase and higher crystalline after heated from 900 to 1300 °C. The crystalline of β -tricalcium phosphate was increased with increasing zinc concentration. The zinc substitution and phase change of zinc substituted hydroxyapatite was confirmed with FTIR and FESEM results.

Keywords: Eggshells, Hydroxyapatite, Precipitation, Zinc

Introduction

Hydroxyapatite is the major constituent of the skeleton and teeth of vertebrates and one of choices for bone tissue engineering application [1] due to its similarity of composition with the mineral of the real bone, biocompatibility, ability to promote cellular function, expressions and osteon conductivity [2]. However, hydroxyapatite shows that the bioactivity and bio resorption rate can be relatively limited. In this work have focused on the cationic and anionic substitute which aiming to mimic biological properties [3]. Hydroxyapatite structure can be substituted by several ionic that induce change in morphology, crystallinity,

resorption rate and thermal ability. Zinc ion is one of all in mineral phase of bone can be used in experimental on hydroxyapatite synthesis. Zinc is a relevant metallic element in the human body and important in cell differentiation, growth and metabolism of protein, lipid and carbohydrate [4]. Thus, the aim of this work is synthesis the hydroxyapatite from egg shells doped Zn at various concentrations from 1 to 25 % wt by precipitation method and calcite at different temperature from 200 to 1300 °C. The crystal structure, functional group and morphology of Zn- substituted on hydroxyapatite were characterized via X-ray diffractometer (XRD, Fourier transform infrared

spectroscopy (FTIR) and field emission scanning microscope (FESEM).

Materials and Methods

Chicken egg shells were collected from KMUTT canteen Bangkok, Thailand. Diammonium hydrogen orthophosphate ($(\text{NH}_4)_2\text{HPO}_4$), ammonia solution, zinc nitrate ($\text{Zn}(\text{NO}_3)_2$) and nitric acid were purchased from Sigma-Aldrich Company, USA. The membranes of chicken egg shells were removed and washed with distilled water to remove adhesion. The chicken egg shells were dried in the air for a few days. The chicken egg shells were ground into powder with agate mortar. Finally, the chicken egg shells were heated at 1300 °C with rate 5 °C/min at room temperature. The calcium oxide (CaO) powder from chicken egg shells was mixed with $\text{Zn}(\text{NO}_3)_2$ powders at the different percent weight from 1 to 25. The CaO and $\text{Zn}(\text{NO}_3)_2$ were mixed with HNO_3 and adjusted pH with ammonia solution. Then, it was precipitated with $(\text{NH}_4)_3\text{HPO}_4$ solution and ammonia was used to as agent for pH adjustment. The 800 ml of $(\text{NH}_4)_3\text{HPO}_4$ solution was dropped into the 700 ml of $\text{CaO}-\text{Zn}(\text{NO}_3)_2-\text{HNO}_3$ solution with vigorous stirring. The pH of the solution was adjusted to 12 with ammonia solution. These experiments were synthesized in nitrogen atmosphere. The solution was kept at room temperature for 48 h and washed with distilled water until ammonia was not detected in solution. The sample was filtered with no. 1 of filter paper (Whatman, UK) and kept in an oven at 90 °C for 48 h. After synthesis, the calcination was performed in the following heating schedule: 10 °C/min up to the desired temperature (200 to 1300 °C), and a plateau with a residence time at this temperature of 4 h. Then, it was cooled down at 10 °C/min to room temperature. The structure and phase structure of the samples were characterized by X-ray diffraction (XRD) using Bruker D8 Advance diffractometer with $\text{CuK}\alpha$ radiation generated at 40 kV and 40 mA. The samples were measured from 20° to 60° (2 Theta) with a step size of

0.02° and a count time of 1 s per step. The functional groups of the samples were investigated at room temperature by Perkin Elmer (spectra two) spectrometer. The samples were measured within a range of 400 to 4000 cm^{-1} , 16 scans and spectral resolution of 2 cm^{-1} . The surface morphology and particle size of the samples were evaluated by field emission scanning electron microscope (FESEM, FEI Nova NanoSEM 450).

Results and Discussion

The hydroxyapatite from chicken eggshell was doped Zn various concentration from 1 to 25 percent weight was studied and reported by XRD, FTIR, FESEM. The results indicated that the Ca^{2+} ion was substituted with Zn^{2+} ion. The crystalline size of hydroxyapatite doped Zn was decreased with increasing concentration of Zn. The hydroxyapatite doped Zn at 25 percent weight was selected for studying thermal behavior from 200 to 1300 °C. The X-ray diffraction pattern of hydroxyapatite doped Zn at 25 percent weight was heated various temperatures shown in Figure 1. The peak of XRD pattern has broadened indicated amorphous phase of hydroxyapatite (JCPDS file no. 09-0432) at low temperature. The intensity of XRD peak was increased with increasing temperature after heated from 200 to 700 °C. After heated at 800 °C, the peak of hydroxyapatite 2theta around 32.01 to 33.16 was separated into 2 peaks and sharp due to hydroxyapatite had higher crystallinity after heat treatment. In addition, the new peaks were appeared at 2theta 28.10 and 34.71 and sharpened after heat 900 °C. These new peaks were assigned to the β -tricalcium phosphate according to JCPDS file no. 09-0169. After heated 1000 to 1300 °C, the sample consisted two phases of hydroxyapatite and β -tricalcium phosphate. From the result, the temperature at 900 °C was selected for heat treatment hydroxyapatite doped Zn various concentration.

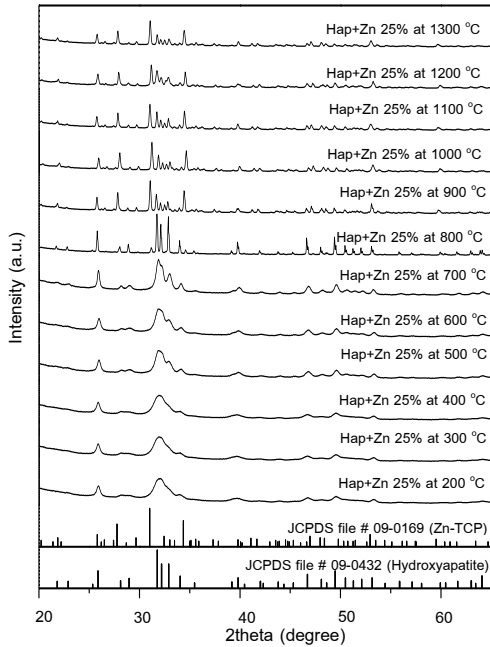


Figure 1 XRD patterns of hydroxyapatite doped Zn 25%wt heated at various temperatures

The XRD pattern of hydroxyapatite doped Zn various concentration after heated at 900 °C as shown in Figure 2. The XRD pattern show that the hydroxyapatite doped Zn from 1 to 13 percent weight was not detected other crystal phase. At 15 percent weight, the new phase of β -tricalcium phosphate was occurred and increased with increasing Zn concentration while intensity of hydroxyapatite decreased. For pure hydroxyapatite was transformed to β -tricalcium phosphate after heat treatment more 1300 °C [5]. But in this experiment the hydroxyapatite doped Zn 15 percent weight was change to β -tricalcium phosphate phase after heat treatment only 900 °C. From the results indicated that the Zn concentration as a catalyzer for phase transformed of hydroxyapatite to β -tricalcium phosphate after heat treatment.

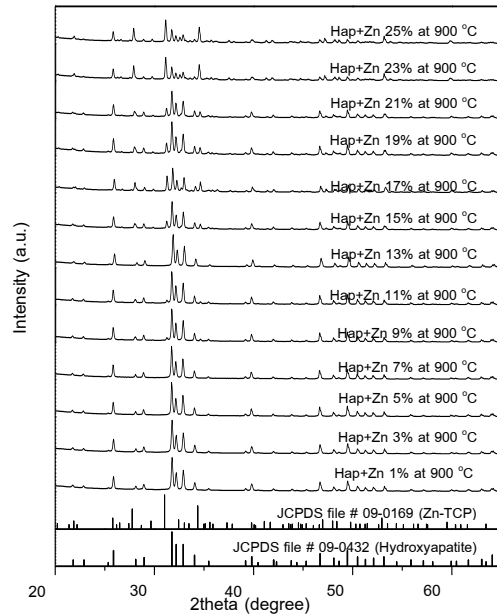


Figure 2 XRD patterns of hydroxyapatite doped Zn 1-25%wt heated at 900°C

The function groups of hydroxyapatite dope Zn and heat treatment as shown in Figure 3 and 4. From the results, all the samples show the same FTIR spectra. The broad bands region 571, 632, 962 and 1026 cm^{-1} were assignment PO_4^{3-} group and other chemical groups were summarized in Table 1. In addition, the broad band at 632 of (OH⁻) vibration of β -tricalcium phosphate was not detected in hydroxyapatite doped Zn heated lower 900 °C indicated that the FTIR results were accorded with XRD results.

Table 1 FTIR vibration modes of synthesized Zn-HAP

Wave number (cm^{-1})	Function Group
571	(PO_4^{3-}) Bending
602	(PO_4^{3-}) Bending
962	(PO_4^{3-}) Bending
1091	(PO_4^{3-}) Stretching
1026	(PO_4^{3-}) Stretching
632	(OH ⁻) Vibration

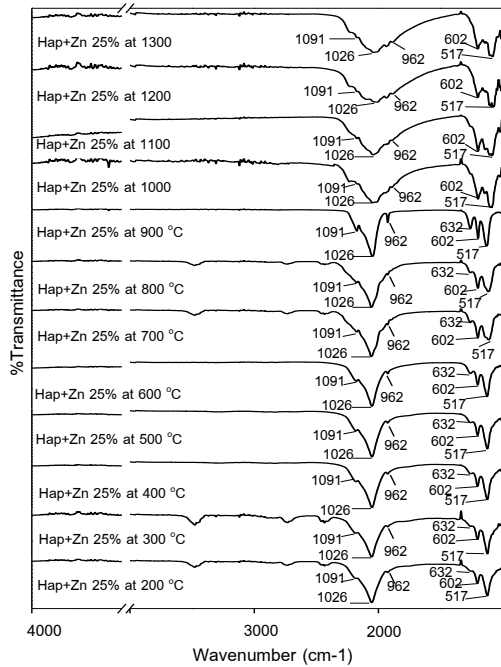


Figure 3 FTIR spectra of hydroxyapatite doped Zn 25%wt heated various temperature 200 to 1300 °C

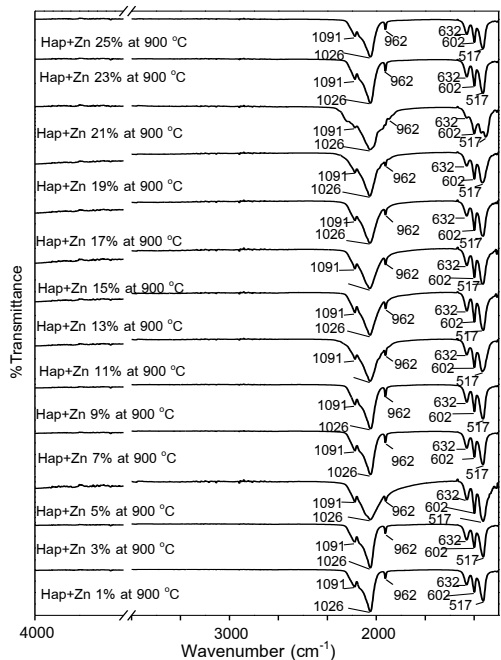


Figure 4 FTIR spectra of hydroxyapatite doped Zn 1-25%wt heated at 900 °C

The FESEM micrograph of hydroxyapatite doped Zn various concentration after heated at 900 °C as shown in Figure 5. From the FESEM micrograph, the particle of hydroxyapatite was agglomerated and depended on Zn concentration. Particles size of hydroxyapatite was become to nanometer and more dispersed at high Zn concentration.

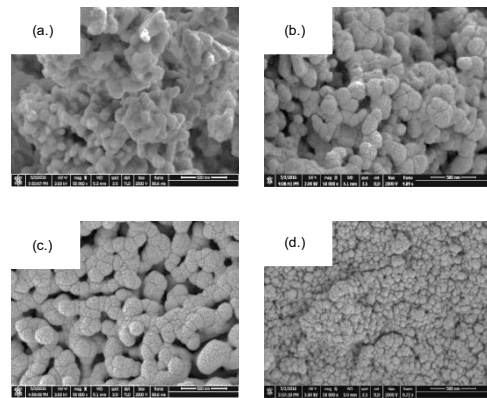


Figure 5 FESEM micrograph of hydroxyapatite doped Zn 1-25%wt heated at 900°C (a.) Hap+Zn 1% (b.) Hap+Zn 7% (c.) Hap+Zn 19% (d.) Hap+Zn 25%

Conclusions

The hydroxyapatite synthesized from chicken eggshell was doped Zn at various concentration by precipitation technique. The Zn^{2+} ion was substituted Ca^{2+} ion result in the crystalline size of hydroxyapatite decreased. Hydroxyapatite doped Zn no less than 13 percent weight indicated that transformed to β -tricalcium phosphate after heat treatment at 900 °C. The nanoparticle of hydroxyapatite more dispersed at high Zn concentration. The experiment shows that the Zn addition on hydroxyapatite as a catalyzer for phase transformed of hydroxyapatite to β -tricalcium phosphate after heat treatment.

Acknowledgments

In acknowledgement you may thank all the people/organizations who provided their assistance to you in forms of advice, suggestions, and any others.

References

- [1] Meski, S. , Ziani, S. , Khireddine, H. , Boudboub, S., and Zaidi, S. 2011. "Factorial design analysis for sorption of zinc on hydroxyapatite". **J Hazard Mater.** 186: 1007-1017.
- [2] Santos, V. , Zeni, M. , Bergmann, C. P. , and Hohemberger, J.M. 2008. "Correlation between thermal treatment and tetragonal/ monoclinic nanostructured zirconia powder obtained by sol-gel process". **Adv Mater Sci.** 17: 62-70.
- [3] Miyaji, F. , Kono, Y. , and Suyama, Y. , 2005. "Formation and structure of zinc- substituted calcium hydroxyapatite". **Mater Res Bull.** 40: 209-220.
- [4] Ioku, K., Fukuhara, M., Fujimori, H., and Goto, S. 1999, "Hydroxyapatite sheet prepared by hydrothermal one- process method". **J Korean Chem Soc.** 5:1 – 15.
- [5] Pankaew P. , Hoonnivathana E. , Limsuwan P. , and Naemchanthara K. 2010. "Temperature effect on calcium phosphate synthesized from chicken eggshells and ammonium phosphate". **J Appl Sci.** 10: 3337-3342.
- [6] Ioku, K., Fukuhara, M., Fujimori, H., and Goto, S. 1999. "Hydroxyapatite sheet prepared by hydrothermal one- process method". **J Korean Chem Soc.** 5:1 – 15.
- [7] Takahashi, H. , Yashima, M. , Kakihana, M. , and Yoshimura, M., 1995. "Synthesis of stoichiometric hydroxyapatite by a gela route from the aqueous solution of citric and phosphine acetic acids". **Eur J Solid State Inorg Chem.** 32: 29 - 35.
- [8] Layrolle, P., Ito, A., and Takishi, T. 1999. "Sol-gel synthesis of amorphous calcium phosphate and sintering into microporous hydroxyapatite bioceramics". **J Am Chem Soc.** 81:1 - 8.
- [9] Gross, K.A., Chai, C.S., Kannangara, G.S.K., Bin-Nissan, B. , Hanley L. , and Thin, A. 1998. "Hydroxyapatite coatings via sol-gel synthesis". **J Mater Sci Mater Methods.** 9: 39 - 43.

Evaluation of Radiation Dose from Powder and Bulk Hydroxyapatite for Routine Dosimeter

K. Boonsook¹, S. Ninlapruk², P. Limsuwan¹ and K. Naemchanthara^{1*}

¹Department of Physics, Faculty of Science, King Mongkut's University of Technology Thonburi,
126 Prachauthit Road, Thung Khru, Bangkok, 10140, Thailand

²Office of atom for peace, 16 Vibhavadee Rungsit, Chatuchak, Bangkok, 10900, Thailand

*E-mail: puri_kit@hotmail.com

Abstract

The aim of this study is to analyze the interaction of gamma radiation with powder and bulk hydroxyapatite synthesized from quail eggshell at various doses for development hydroxyapatite as a routine dosimeter. The powder and bulk of hydroxyapatite were irradiated with gamma from 0.1 kGy to 10 kGy. Electron spin resonance (ESR) spectroscopy was used to determine and evaluate dose response from characteristic signal. The center peak group of both ESR signals was occurred g-value at 2.0029, 2.0022, 2.0018 and 1.9986 that indicated the radiation induced inorganic free radicals of 4 molecule ions as CO^- , CO_2^- , CO_3^{3-} and CO_2^- , respectively. The correlation between the intensity of ESR signal with the dose response of bulk hydroxyapatite was good polynomial function in range 0.2 kGy to 2 kGy. Furthermore, the free radicals stability of hydroxyapatite during 45 - 60 days after irradiated showed a small decay about 25%. These results have shown that the bulk hydroxyapatite from quail eggshell could be used a good and easily routine dosimeter for high dose.

Keywords: Eggshell, Electron spin resonance spectroscopy, Gamma radiation, Hydroxyapatite, Quail eggshell

Introduction

Hydroxyapatite ($\text{Ca}_{10}(\text{PO}_4)_6(\text{OH})_2$) is highly biocompatible material due to its chemical and structural similarities with inorganic part of the human hard tissue [1]. Bone defects and damage as serious health problems have attracted more and more attentions. Hydroxyapatite is material select for bone replacement [2]. After bone replacement, patients have live and work. The patient bone replacement will be work about radiation or diagnose by radiation. Then, hydroxyapatite from synthesize must be investigate the effect of radiation on hydroxyapatite. In the research, the hydroxyapatite synthesis from quail eggshell before and after irradiated gamma ray was characterized by electron spin resonance (ESR) spectroscopy. The dose

response, new radiation dose and percentage error of hydroxyapatite was determined for describe behavior of radical after irradiated and applied for new dosimeter use in routine dosimeter.

Materials and Methods

The quail eggshells were removed membrane and cleaned with water. The quail eggshells were annealed in oven at 70 °C for 24 h and crushed into powder with agate mortar and pestle. The calcium oxide (CaO) was synthesized from quail eggshell heated at 1300 °C in the room temperature for 4 h with heating rate 5 °C/min. The CaO from quail eggshell was mixed with nitric acid (HNO_3) and adjusted pH with ammonia solution. Then, it was precipitated with

$(\text{NH}_4)_3\text{HPO}_4$ solution and ammonia was used to as agent for pH adjustment. The solution was stirred with magnetic stirrer for 24 h and rinsed and washed with distilled water many time until ammonia not remains. The precipitate from solution was filtered with paper filter and annealed in oven at 100°C for 48 h to removed water [3]. The hydroxyapatite was crushed into powder and sieved with a sieve size $150\ \mu\text{m}$. The bulk of hydroxyapatite was prepared from hydroxyapatite 0.065 g molded with force 3000 N. The powder and bulk hydroxyapatite from quail eggshell were irradiated with gamma ray from ^{60}Co source with various dose rate from 0.1 to 10.0 kGy. The powder

and bulk of hydroxyapatite from quail eggshell were investigated by electron spin resonance (ESR) spectroscopy. The ESR spectra were recorded using a convention X – band spectrometer Bruker, Model E500 at room temperature with a TE011 rectangular cavity, operating at: modulation amplitude 0.4 mT, microwave power 0.635 mW, time constant 10.24 ms and sweep width 64 mT. For dose evaluation and fading time, the dose dependent amplitude of central line in the ESR signal was used. The dose response and fading time of hydroxyapatite were calculated in range 0.1 to 10.0 kGy and 60 days, respectively.

Results and Discussion

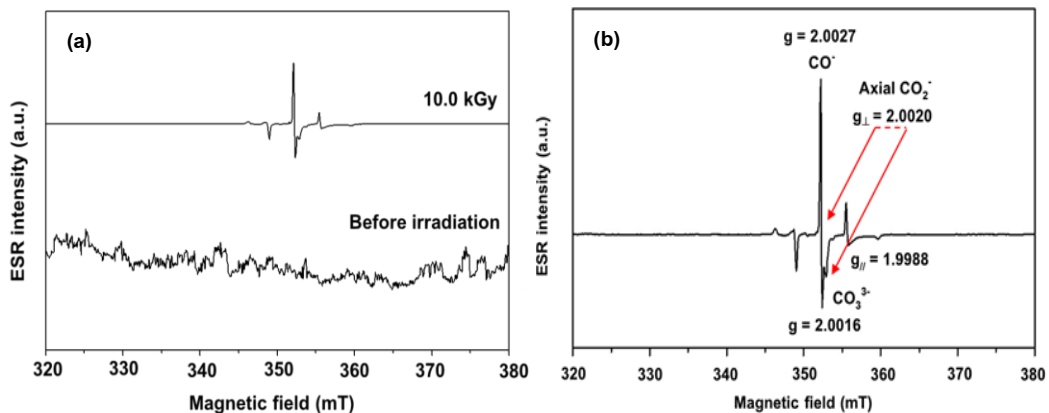


Figure 1 ESR spectrum of hydroxyapatite from quail eggshell (a) before and (b) after irradiation

The spectra of hydroxyapatite from quail eggshell before and after irradiated were shown in Figure 1. The spectra of hydroxyapatite before irradiated were silent that indicated that not free radical. After irradiation, the intensity at center peak was appeared at magnetic field about $352.14 \pm 0.04\ \text{mT}$ and g value 2.0027 ± 0.0002 according with carbonate (CO^\cdot) ion [4]. At magnetic field $352.35 \pm 0.02\ \text{mT}$ or g value 2.0016 ± 0.0002 was accorded with CO_3^{3-} radical [5]. On the other hand, the magnetic field between 352 and 353 mT spectra was appeared anisotropic spectra of axial CO_2^\cdot radical corresponding with g_\perp about 2.0020 ± 0.0002 and g_\parallel about 1.9988 ± 0.0002 [6]. All the peak

of spectra was due to radiation induced free radical of inorganic in hydroxyapatite [7]. The powder and bulk of hydroxyapatite from quail eggshell were irradiated at various doses from 0.1 to 10.0 kGy as shown in Figure 2. The results showed that the intensity ESR signals of carbonate radical of both samples were increased with increasing radiation dose. The relation between radiation dose and intensity ESR signal was plotted and presented in Figure 3. The dose respond curve obtained in case of gamma irradiation was tried to fit by linear function of the applied dose as $y = mx + c$. In this function, y and x represent the intensity of ESR signal and dose exposures,

respectively. The parameter m in this function is representing the slope of linear and parameter c represents y intercept. The parameter m and c of powder and bulk hydroxyapatite from quail eggshell

calculated from fitting procedure was found are 1000000, 271003 ($R^2 = 0.9933$) and 778732, 703654 ($R^2 = 0.9710$), respectively.

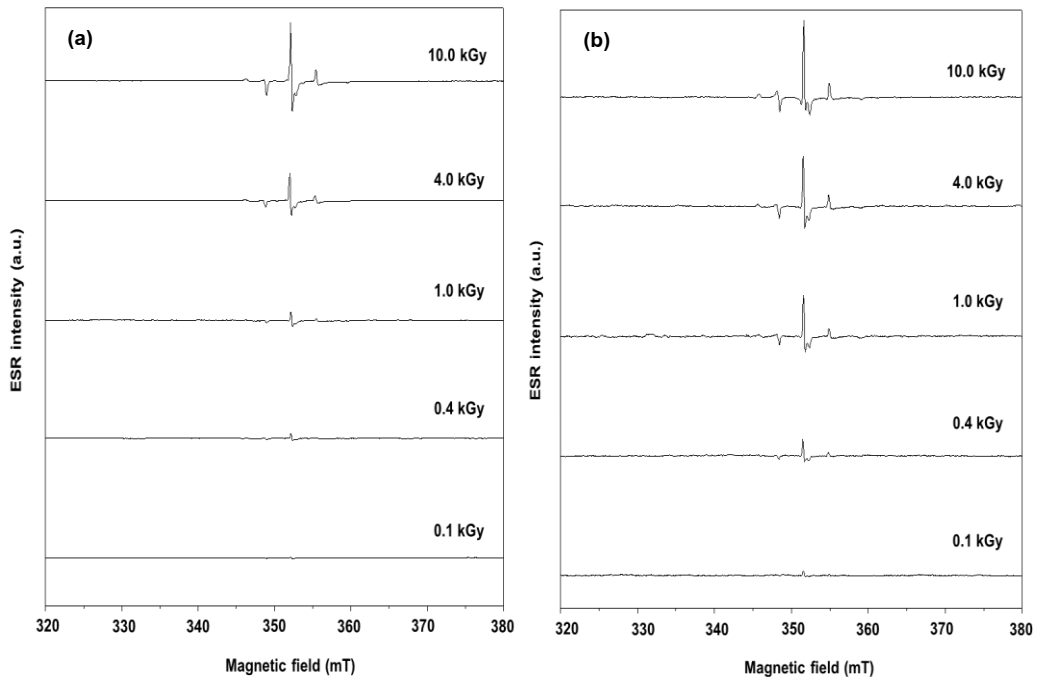


Figure 2 ESR spectrum of (a) powder and (b) bulk hydroxyapatite from quail eggshell at 0.1 to 10.0 kGy

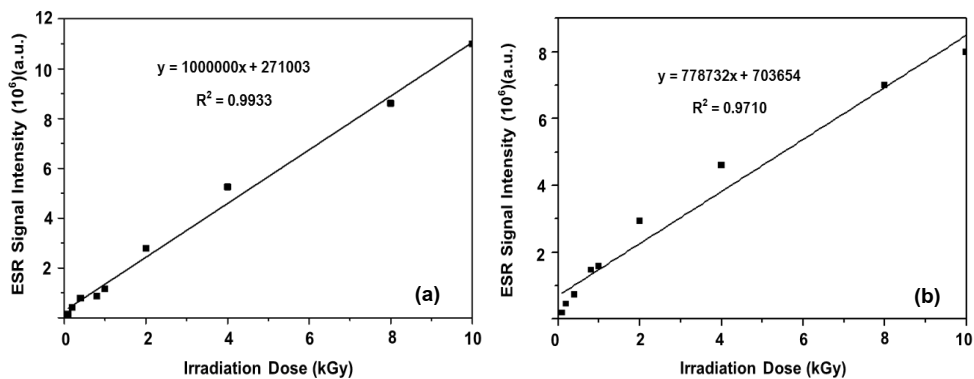


Figure 3 Dose response curve of (a) powder and (b) bulk hydroxyapatite irradiated with gamma ray at dose 0.1 to 10.0 kGy

From this function we can calculate new radiation dose from calibration curve and compared with Fricke solution dose and show results in Table 1. The results show that the percentage error of powder hydroxyapatite was less than 29 but bulk

hydroxyapatite was about 87. For percentage error 29 of powder hydroxyapatite is accept and use in routine laboratory. Bulk hydroxyapatite is convenient and easy to use.

Table 1 Comparison radiation dose and percentage error of powder and bulk hydroxyapatite irradiated at 0.1 to 10.0 kGy.

Dose (kGy)	QS – HAp (powder)		QS – HAp (bulk)	
	Dose (kGy)	% error	Dose (kGy)	% error
0.1	- 0.121	-	- 0.657	-
0.2	0.145	27.566	- 0.322	-
0.4	0.516	28.918	0.051	87.118
0.8	0.599	25.093	0.983	22.901
1.0	0.883	11.722	1.117	11.650
2.0	2.527	26.346	2.877	43.858
4.0	4.982	24.560	5.005	25.127
8.0	8.338	4.220	8.090	1.130
10.0	10.729	7.289	9.356	6.441

The response curve was reconsidered and tried to fit by polynomial function of dose exposure as show in Figure 4. The best correlation is obtained for second degree polynomial varying function as $y = a + bx + cx^2$. In this function, y and x represent the ESR signal intensity and applied radiation dose, respectively and the parameter a, b and c are constant to be determined. The parameter a in this function representing the ESR signal intensity at zero applied dose mean that the relative amount of free radical species of un-irradiated sample and parameter b and c represent the rate of radical production and radiation yield upon irradiation at room temperature. The parameter of a, b and c of bulk hydroxyapatite from fitting procedures was found to be 264948, 1000000 and -56931 ($R^2 = 0.9966$), respectively. The new dose was calculated from polynomial function and compared the Fricke solution as presented in Table 2. From the results show percentage error is terribly. The respond curve was selected exposure dose in range 0.2 to 2.0 kGy and refitted by polynomial function as showed in Figure 5.

The percentage error was calculated after compared dose from Fricke solution and presented in Table 3. All of dose from 0.2 to 2.0 kGy have percentage error less than 20 and less than powder hydroxyapatite. From the experiment can conclusion the powder and bulk hydroxyapatite can use the dosimeter for routine dosimeter in range 0.1 to 10.0 and 0.2 to 2.0 kGy, respectively.

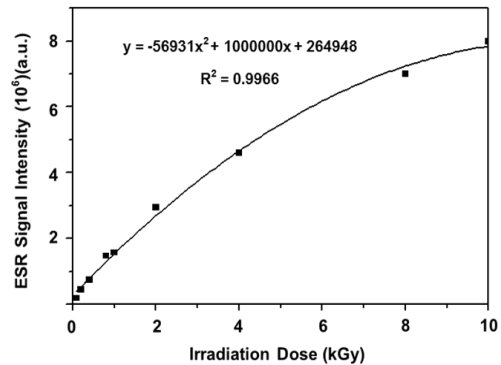


Figure 4 Dose response curve of bulk hydroxyapatite irradiated with gamma ray at dose 0.1 to 10.0 kGy

Table 2 Comparison radiation dose and percentage error of bulk hydroxyapatite from polynomial function irradiated at 0.1 to 10.0 kGy

Dose (kGy)	Bulk Hydroxyapatite (polynomial)	
	Dose (kGy)	% error
0.1	- 0.073	-
0.2	0.190	5.181
0.4	0.493	23.162
0.8	1.301	62.585
1.0	1.424	42.353
2.0	3.299	64.937
4.0	7.800	94.998
8.0	-	-
10.0	-	-

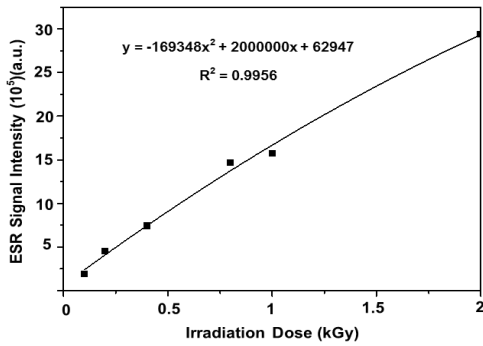


Figure 5 Dose response curve of bulk hydroxyapatite irradiated with gamma ray at dose 0.2 to 2.0 kGy

Table 3 Comparison radiation dose and percentage error of bulk hydroxyapatite from polynomial function at 0.2 to 2.0 kGy

Dose (kGy)	Bulk Hydroxyapatite (polynomial)	
	Dose (kGy)	% error
0.2	0.198	0.940
0.4	0.351	12.290
0.8	0.751	6.134
1.0	0.811	18.926
2.0	1.679	16.028

Fading time and percentage of ESR intensity of hydroxyapatite after irradiated from 1 to 60 days was calculated and shown in Figure 6 and 7, respectively. The results show that the intensity of ESR signal was decreased with increasing time. The ESR intensity of powder hydroxyapatite was decreased about 22% after left for 60 days that less than bulk was compared.

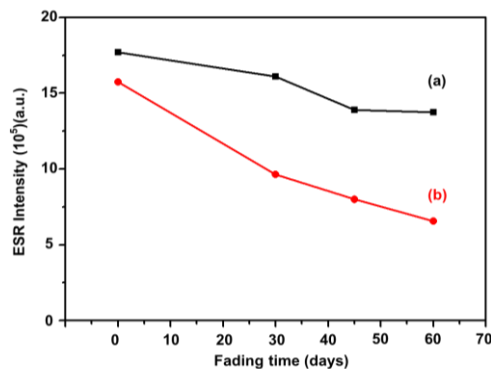


Figure 6 Fading time of ESR intensity of (a) powder and (b) bulk hydroxyapatite at 1 kGy

The bulk hydroxyapatite is easier to use, although fading time is decrease more than powder.

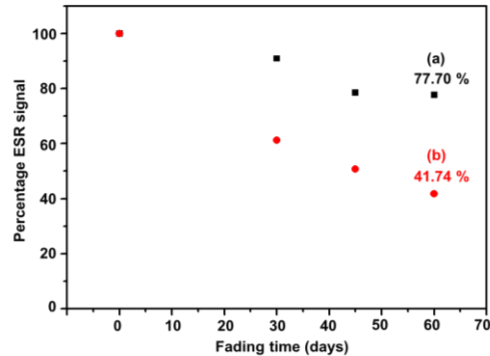


Figure 7 Percentage of ESR intensity of (a) powder and (b) bulk hydroxyapatite irradiated at 1 kGy

Conclusions

The hydroxyapatite synthesized from quail eggshell after irradiated and investigated by ESR spectroscopy was consisted of CO⁻, CO₃³⁻ and axial CO₂⁻ radical. The intensity ESR signal of CO₂⁻ was increased with increasing radiation dose and used to calculated new radiation dose and compared dose with Fricke solution. The powder and bulk hydroxyapatite from quail eggshell can use as a dosimeter for routine dosimeter in rage 0.1 to 10.0 and 0.2 to 2.0 kGy, respectively.

Acknowledgments

The authors gratefully acknowledge the support given to this work by faculty of science, King Mongkut’s University of Technology Thonburi. The authors would like to sincere thanks to office of atoms for peace (OAEP) provided tools for experiment.

References

[1] Maruta, T., Shiraishi, K., Ebina, Y., and Miki, T. 1996. “An ESR study of defects in irradiated hydroxyapatite”. *Appl Radiat Isot.* 47: 1527-1531.
 [2] Ponon, W., Suntornsaratoon, P., Charoenphandhu, N., Thongbunchoo, J., Krishnamra, N., and Mingtang, I. 2016. “Hydroxyapatite from fish scale

- for potential use as bone scaffold or regenerative material". **Mater Sci Eng C**. 62: 183-189.
- [3] Pankaew, P., Hoonivathana, E., Limsuwan, P., and Naemchanthara, K. 2010. "Temperature effect on calcium phosphate synthesized from chicken eggshells and ammonium phosphate". **J Appl Sci**. 10: 3337-3342.
- [4] Moens, P., Callens, F., Matthys, P., Maes, F., Verbeeck, R., and Naessens, D. 1991. "Adsorption of carbonate-derived molecules on the surface of carbonate containing apatites". **J Chem Soc Faraday Trans**. 87: 3137-3147.
- [5] Serway, R.A., and Marshall, S.A. 1967b. "Electron spin resonance absorption spectrum of orthorhombic CO₃ molecule-ions in irradiated single crystal calcite". **J Chem Phys**. 47: 868-869.
- [6] Da Costa, Z.M., Pontuschka, W.M., and Campos, L.L. 2004. "Study of the ESR signal of gamma irradiated hydroxapatite for dose assessment". **Nucl Instr Meth Phys Res B**. 218: 283-288.
- [7] Callens, F.J., Verbeeck, R.M.H., Naessens, D.E., Matthys, P.F.A., and Boesman, E.R. 1989b. "Effect of carbonate content on the ESR spectrum near $g_{\frac{1}{2}}$ of carbonated calcium apatites synthesized from aqueous media". **Calcif Tissue Int**. 44: 114-124.

Characteristic and Formation of Hydroxyapatite Synthesized from Heat Treatment of Cuttlefish Bone

K. Faksawat¹, E. Hoonnivatthana², P. Limsuwan¹ and K. Naemchanthara^{1*}

¹Department of Physics, Faculty of Science, King Mongkut's University of Technology Thonburi,
126 Pracha Uthit Road, Bangmod, Trung Khru, Bangkok, 10260

²Department of Physics, Faculty of Science, Kasetsart University, 50 Ngam Wong Wan Road, Lat Yao,
Chatuchak, Bangkok, 10900

*E-mail: puri_kit@hotmail.com

Abstract

Hydroxyapatite is one of calcium phosphate phase and widely use in medical and dental application. Hydroxyapatite could be synthesized from natural calcium source. Cuttlefish bone waste are mainly composed of calcium carbonate. This paper, hydroxyapatite was synthesized from cuttlefish bone by high energy ball milling technique. The cuttlefish bone was heated at different temperature from 200 to 1300 °C. The heated cuttlefish bones at different temperature were mixed with di ammonium hydrogen orthophosphate ratio 5:3 moles and added distilled water 25 ml. The solution was milled at different time from 5 to 120 min. The structure, morphology and functional group of cuttlefish bone and hydroxyapatite samples were investigated with X-ray diffraction (XRD), field emission scanning electron microscopy (FESEM) and Fourier transform infrared spectroscopy (FTIR), respectively. The results show that the natural phase of cuttlefish bone was aragonite phase of calcium carbonate (CaCO₃) and changed to pure calcite phase after heated at 500 °C. The calcite phase of cuttlefish bone was completely transformed to calcium oxide (CaO) after heated at 900 °C. For hydroxyapatite synthesizing show that the samples were milled for 5 min not only hydroxyapatite phase appeared but also remained initial phase. The pure hydroxyapatite phase appeared that the aragonite and lime phase precursor were milled for 60 and 5 min, respectively. From experiment, the cuttlefish bone before and after heated can be use a source of calcium for hydroxyapatite synthesizing by high energy ball milling technique.

Keywords: Hydroxyapatite, Cuttlefish bone, Ball milling

Introduction

Hydroxyapatite (Ca₁₀(PO₄)₆(OH)₂) is a one of calcium phosphate and major component of bone and tooth [1]. Hydroxyapatite can be used in orthopedics and dental application due to their similar chemical composition with real bone [2]. Furthermore, hydroxyapatite is used for repairing of bone defect owing to its perfect biocompatibility, osteon conductivity and bioactivity [3]. Hydroxyapatite can be synthesized from several natural materials such as egg shell, coral,

fish bone, sea shell and bovine bone. Cuttlefish bone is a one of natural materials that consist of calcium more than 90% [4]. Cuttlefish bone has been selected to produce hydroxyapatite and can help to promoting recycle of materials. In this work, hydroxyapatite is prepared by ball milling technique for providing of short term to reaction and hydroxyapatite is characterized by X-ray diffraction (XRD), Fourier transform infrared spectroscopy (FTIR) and field emission scanning electron microscope (FESEM).

Materials and Methods

The cuttlefish bones which were obtained from Samut Prakarn province in Thailand were washed by distilled water. Then, the cuttlefish bones were dried in the air and ground until to powder by agate mortar. The cuttlefish bone powder was heated 200 to 1300 °C with rate 5 °C/min in the room temperature. The changed phase of cuttlefish bone from XRD results was selected 3 temperatures such as before and after heated cuttlefish bones at 500 and 900 °C which use be precursors for synthesized hydroxyapatite. Each precursor was mixed diammonium hydrogen orthophosphate and distilled water in stainless steel container. The mixed ratio of the cuttlefish bone powder to $(\text{NH}_4)_2\text{HPO}_4$ was 5:3 (mole ratio). The mixture was milled in a high energy ball milling machine for various durations 5, 30, 60 and 120 min. After milling, the slurry was dried in a convection oven at 90 °C for 48 h. The samples were kept in desiccator and ground into powder for characterization.

The crystalline structure of the samples was characterized by powder X-ray diffractometer (XRD; Philips X'Pert PW3020) with $\text{CuK}\alpha$ ($\lambda = 1.5418 \text{ \AA}$) radiation source generated at 30 kV and 30 mA in the 2-theta range 20 to 80 degree at scan speed of 0.02 seconds. Identification of the phase was performed by the Joint Committee on Powder Diffraction Standard (JCPDS). The microstructure of the samples was observed by a field-emission scanning electron microscopy (FESEM; FEI Nova NanoSEM 450). The functional group of the samples was identified by a Fourier transform infrared spectroscopy (FTIR; Perkin Elmer spectrum two), over the region 400-4000 cm^{-1} with a spectral resolution of 2 cm^{-1} .

Results and Discussion

The crystalline structures of the before and after heated cuttlefish bone are shown the Figure 1. The raw cuttlefish bone showed an aragonite phase of CaCO_3 according to the JCPDS file no. 75-2230. The aragonite phase was completely changed to a calcite phase of

CaCO_3 at 500 °C and an accorded to the JCPDS file no. 72-1937. After heat at 900 C, the calcite phase of CaCO_3 was completely transformed to lime phase (calcium oxide; CaO) according to JCPDS file no. 78-0649. The intensity of CaO phase from cuttlefish bone was not changed and continued up to 1300 °C. The thermal decomposition of CaCO_3 from cuttlefish bone can be described by an equation [5].

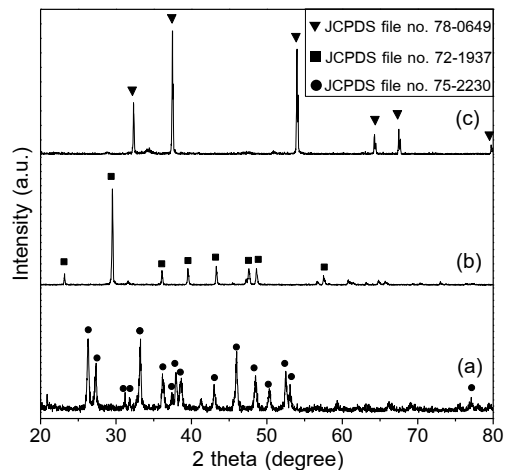
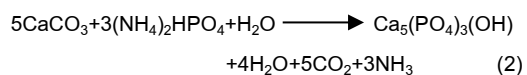


Figure 1 XRD patterns of before and after heated cuttlefish bone at (a) raw cuttlefish bone, (b) 500 °C and (c) 900 °C

Hydroxyapatite from aragonite phase

Figure 2 shows the XRD pattern of the hydroxyapatite synthesized from aragonite phase of cuttlefish bone by ball milling at various time. The results show that hydroxyapatite phase appeared after ball milled sample for 5 min, the intensities of hydroxyapatite increased while diffraction peak of aragonite phase decreased. Upon milling for 60 min, the pure hydroxyapatite peaks present and continue up to 120 min according to JCPDS file no. 09-0432. The chemical reaction of hydroxyapatite shows by following equation [6].



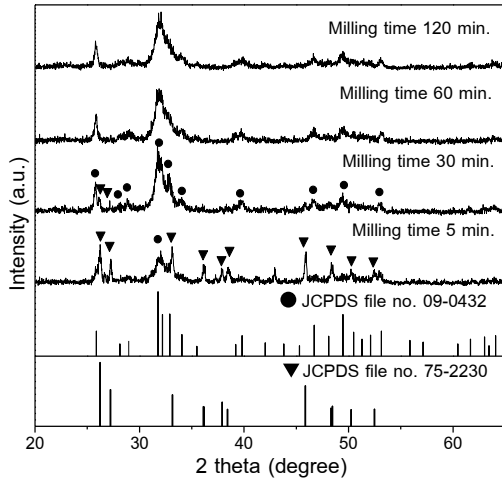


Figure 2 XRD patterns of synthesized hydroxyapatite from aragonite phase precursor milled for different time
Hydroxyapatite from calcite phase

Figure 3 shows the X-ray diffraction patterns of hydroxyapatite synthesized from calcite phase of heated cuttlefish bone at 500 °C for 5, 30, 60 and 120 min. The peak of hydroxyapatite appeared after sample milled 5 min but still remain the peak of calcite phase in the sample. When milling to more than 30 min, the diffraction peak of hydroxyapatite increased and the intensities of calcite phase decreased with increasing in the milling time as shown in the Figure 3.

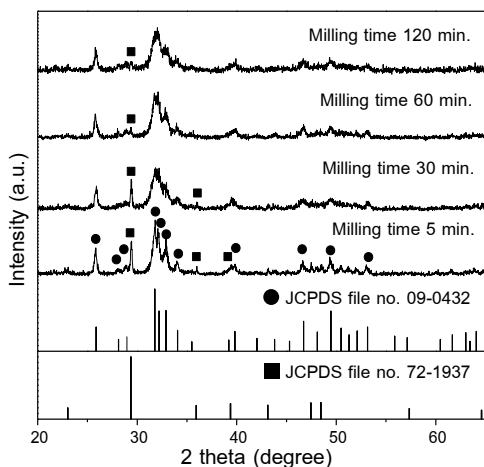


Figure 3 XRD patterns of synthesized hydroxyapatite from calcite phase precursor milled for different time

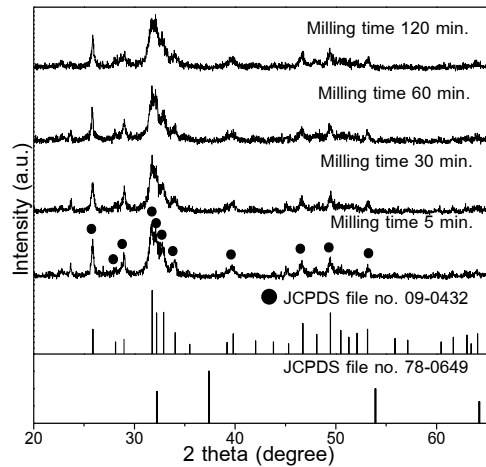


Figure 4 XRD patterns of synthesized hydroxyapatite from lime phase precursor milled for different time

Hydroxyapatite from lime phase

Figure 4 present the XRD patterns of hydroxyapatite synthesized from CaO phase of the heated cuttlefish bones and (NH₄)₂HPO₄ milled for 5, 30, 60 and 120 min. After milled at 5 min. the powder of CaO, (NH₄)₂HPO₄ and distilled water completely reacted to hydroxyapatite. The intensity of hydroxyapatite was increased with increasing ball milling time. From the results can be conclude the reaction of hydroxyapatite as in equation [6].

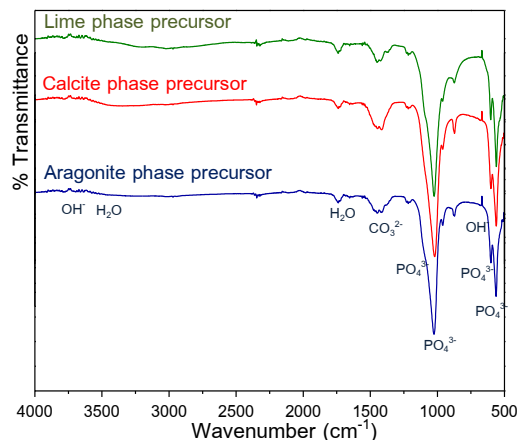
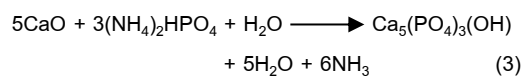


Figure 5 FTIR spectra of synthesized hydroxyapatite from different phase precursors milled for 120 min

The FTIR spectra of hydroxyapatite synthesized milled from all precursor for 120 min as shown the Figure 5. The hydroxyapatite bands have been observed in all of these sample. All sample had OH⁻ group, stretching mode at 3532 cm⁻¹ and vibration at 630 cm⁻¹. The band of PO₄³⁻ group appeared in region about 900 to 1150 cm⁻¹, that vibration of bond shows

stretching modes and in region 600 and 562 cm⁻¹, which showing the bending modes. The weak band appeared at 1437 cm⁻¹. This band demonstrated the attendance of CO₂ in the synthesized hydroxyapatite [7]. The results of FTIR are corresponding with the XRD results.

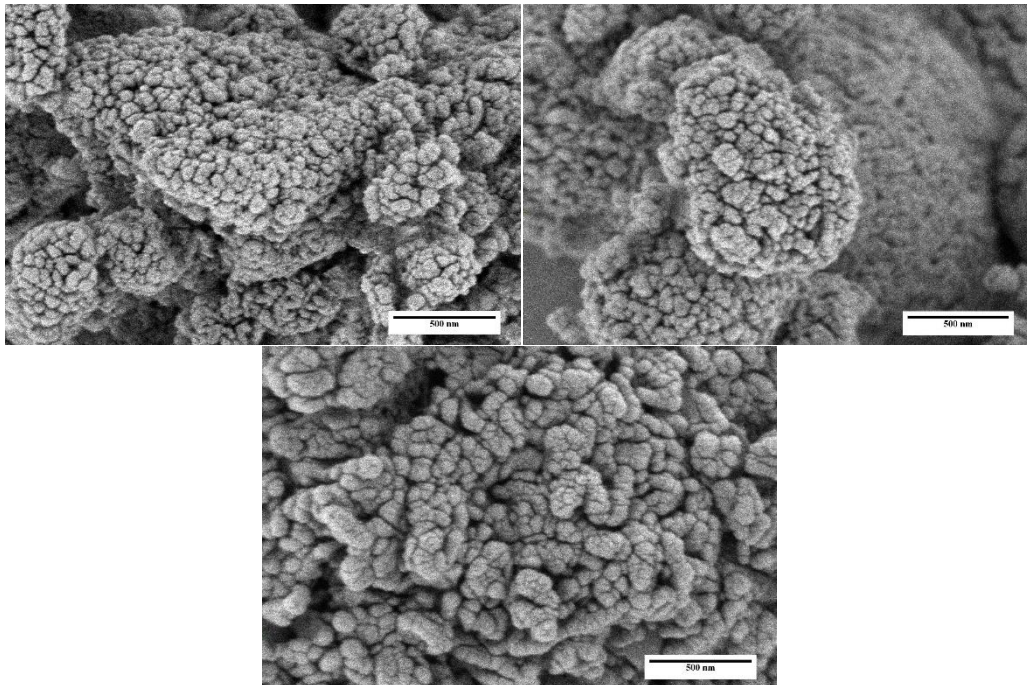


Figure 6 the FESEM image of the synthesized hydroxyapatite from different precursors milled for 120 min (a) aragonite (b) calcite and (c) lime precursors

Figure 6 shows the FESEM image of the all samples milled for 120 min. The all hydroxyapatite was an agglomerate of fine, sphere like crystals. The particles size of all sample were about 60 to 70 nm and nanoparticles had also an interconnect and porosity. The nanostructure hydroxyapatite is related to good bioactivity and can be used for bone tissue engineering application [8].

calcite phase at 500 °C and completely change to lime phase at 900 °C. The lime and aragonite phase precursors can be synthesized hydroxyapatite milled for 5 and 60 min, respectively but the calcite phase must be ball milled more than 120 min. The all sample had an average particle size about 60-70 nm and were agglomeration. From the results, the ball milling technique can be provided easy and short term to synthesized nano hydroxyapatite.

Conclusions

The crystal structure of raw cuttlefish bone is aragonite phase. The aragonite phase transform to

Acknowledgments

The authors gratefully acknowledge the support given to this work by Faculty of Science, King Mongkut's University of Technology Thonburi. The authors would like to sincere thanks to Kasetsart University, Kamphaeng Saen campus provided Fourier transform infrared spectroscopy for experiment.

References

- [1] Gao, Y., Cao, W.L., Wang, X.Y., Gong, Y.D., Tian, J. M. , Zhao, N. M. , and Zhang, X. F. 2006. "Characterization and osteoblast- like cell compatibility of porous scaffolds: bovine hydroxyapatite and novel hydroxyapatite artificial bone". **J Mater Sci Mater Med.** 17: 815-823.
- [2] Akram, M., Ahmed, R., Shakir, I., Ibrahim, W., and Hussain, R., 2014. "Extracting hydroxyapatite and its precursors from natural resources. **J Mater Sci.** 49: 1461-1475.
- [3] Wu, S.C., Hsu, H.C., Hsu, S.K., Chang, Y.C., and Ho, W.F. 2015. "Effect of heat treatment on the synthesis of hydroxyapatite from eggshell powders". **Ceram Int.** 41: 10718-10724.
- [4] Cadman, J., Zhou, S., Chen, Y., and Li, Q. 2012. "Cuttlebone: characterisation, application and development of biomimetic materials". **J Bionic Eng.** 9: 367-376.
- [5] Eric, M.R., Witold, B., Victor, M.C., Diaz-Estrada, J. R. , Hernandez, R. , and Rodriguez, J. R. 1999. "Synthesis of hydroxyapatite from eggshells" . **J Mater Let.** 41: 128-134.
- [6] Mehdi, S. S., Khorasani, M. T. , Ehsan, D. K. , and Ahmad, J. 2013. " Synthesis methods for nanosized hydroxyapatite with diverse structures". **Acta Biomater.** 9: 7591-7621.
- [7] Amin, S. , Bekhit, A. E. , Azam, A. , and Zhifa, S. 2015. "Synthesis of nano-hydroxyapatite (nHA) from waste mussel shells using a rapid microwave Method". **Mater Chem Phys.** 149-150: 607-616.
- [8] Lee, S. J. , Lee, Y. C. , and Yoon, Y. S. 2007. "Characteristics of calcium phosphate powders synthesized from cuttlefish bone and phosphoric acid", **J Ceram Process Res.** 8: 427-430.

Microstructure of Hydroxyapatite from Waste Eggshell Synthesized under Different Temperature

A. Sangmala, P. Limsuwan and K. Naemchanthara

Department of Physics, Faculty of Science, King Mongkut's University of Technology Thonburi,
126 Pracha-Uthit Rd., Bangmod, Trungkru, Bangkok, 10140, Thailand

*E-mail: puri_kit@hotmail.com

Abstract

Hydroxyapatite, $\text{Ca}_{10}(\text{PO}_4)_6(\text{OH})_2$ were prepared by the reaction of calcium hydroxide from waste chicken eggshell and di-ammonium hydrogen orthophosphate solution and heated at different temperature from 200 to 700°C for 4 h. The crystal structure, function group and morphology of hydroxyapatite were investigated by X-ray diffraction (XRD), Fourier transform infrared spectroscopy (FTIR) and field emission scanning electron microscopy (FESEM), respectively. The structure was found to be hydroxyapatite phase at 200 to 600°C and the crystalline size increased with increasing temperature. However, the hydroxyapatite phase was transformed to tri-calcium phosphate phase completely at 700°C. The morphology of hydroxyapatite were agglomerates and sphere particles. These experiments show that the hydroxyapatite could be synthesized from waste chicken eggshell and reduced time and cost for biomaterials application.

Keywords : Calcium hydroxide, Chicken eggshell, Heat treatment, Hydroxyapatite

Introduction

Hydroxyapatite ($\text{Ca}_{10}(\text{PO}_4)_6(\text{OH})_2$) is the most famous material which use in orthopedic and dental material [1]. It can be found in the living bone and is the major inorganic component of natural bone [2]. Although hydroxyapatite has been widely use in medical application, but it is too expensive for some patient groups. Recently, researchers study and develop the methods to synthesis hydroxyapatite in low cost. One of the most methods for reducing the cost is use the bio waste for hydroxyapatite synthesizing. The bio waste are several kind such as coral, animal bone and eggshell [3]. Because, they are full of calcium that is the major composition of hydroxyapatite. In the present work, the chicken eggshells had been used as the calcium source of hydroxyapatite synthesizing. The method to synthesis is wet chemical with different temperature. And the samples were heated to

treatment from 200 to 800°C for study temperature effect. The crystal structure phase, chemical function groups and morphology of hydroxyapatite were investigated by X-ray diffraction (XRD), Fourier transform infrared (FITR) spectroscopy and field emission scanning electron microscopy (FESEM), respectively.

Materials and Methods

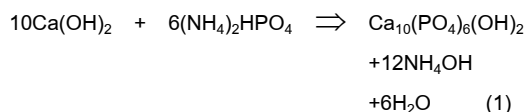
The chicken eggshells were obtained from canteen at King Mongkut's University of Technology Thonburi (KMUTT), Bangkok, Thailand. Di-ammonium hydrogen orthophosphate ($(\text{NH}_4)_2\text{HPO}_4$), was purchased from Ajax Finechem company, Australia. The inner membranes of chicken eggshells were removed, washed with distill water and dried at room temperature for two days. The chicken eggshells were grounded into powder with agate mortar. Finally, the

eggshells were heated at 1300°C with rate 5°C/min and transformed to calcium oxide (CaO). The calcium hydroxide (Ca(OH)₂) were prepared by dissolve the CaO powder in the distill water. While, the hydroxyapatite were prepared by the reaction of Ca(OH)₂ and (NH₄)₂HPO₄. The Ca(OH)₂ solution was mixed with (NH₄)₂HPO₄ solution and stirred by magnetic stirring for 30 min. The sample solution was calcined at 200 to 700°C with an increment 100°C for 4 h. The samples after calcined were heated at different temperature from 200 to 800°C for 4 h for studying the temperature effect. The crystal structure phases of the samples were investigated by X-ray diffraction (XRD) using Phillips PW108 with CuK_α radiation generated at 30 kV and 30 mA. The function groups of the samples were measured by Fourier transforms infrared spectroscopy (FTIR, Perkin Elmer (spectra two)). The morphology and particles size of the samples characterized by field emission scanning electron microscopy (FESEM, FEI (Nova NanoSEM 450)).

Results and Discussion

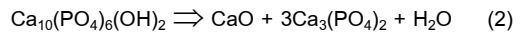
Hydroxyapatite synthesizing under different temperature.

The XRD pattern of synthesized sample powder various temperature as shown in Figure. 1. At the 100°C of synthesizing temperature, the XRD pattern of sample was found hydroxyapatite phase according with JCPDS file no. 09-0432. The chemical reaction between Ca(OH)₂ and (NH₄)₂HPO₄ become to hydroxyapatite as an equation [4].



After increased up to 600°C of the synthesizing temperature, the phase of the sample was found in hydroxyapatite as same synthesizing at 200°C. Moreover, phase of the sample became to tri-calcium phosphate (Ca₃(PO₄)₂) according with JCPDS file no.70-2065 at 700°C of synthesizing temperature.

The Ca₃(PO₄)₂ phase can be formed at 700°C as a result of the deformation of hydroxyapatite phase as an equation [5].



However, the other phase was found in the samples at 400 to 700°C. A small peak was observed at 29.57 degree of XRD pattern which is the calcium phosphate (Ca₂P₂O₇) according with JCPDS file no.81-2257 [6].

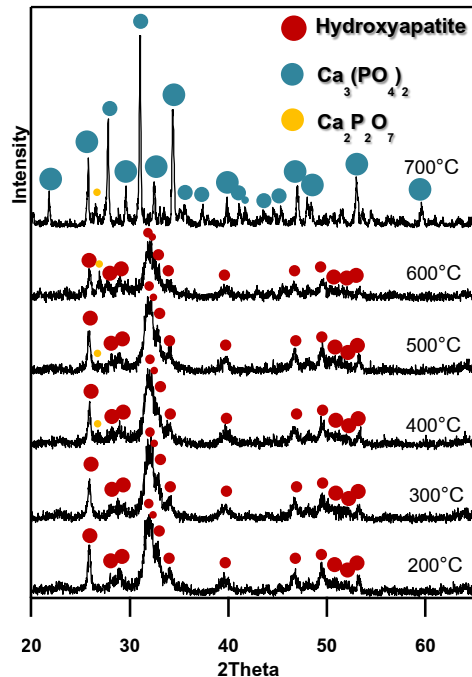


Figure 1 XRD patterns of hydroxyapatite were synthesized various temperature

The FTIR spectra of the samples powder synthesized at various temperature as shown in Figure. 2. The spectra show vibration bands corresponding to phosphate (PO₄³⁻) and hydroxyl (OH⁻) as summarized in Table 1. The band at 1095, 1040, 964, 601 and 562 cm⁻¹ are attributed to the PO₄³⁻. And, the band at 631 cm⁻¹ is attributed to the OH⁻ [4].

Table 1 Observed vibrational frequencies of hydroxyapatite

Wave number (cm ⁻¹)	Function Group
562, 601, 964	(PO ₄ ³⁻)
1040, 1095	(PO ₄ ³⁻)
631	(OH ⁻)

Furthermore, the band at 631 cm^{-1} was not detect in the sample synthesized at 700°C . This FTIR spectra result indicated that OH^- group from hydroxyapatite was decompose after synthesizing at this temperature and hydroxyapatite transform to $\text{Ca}_3(\text{PO}_4)_2$ similarly to the XRD result.

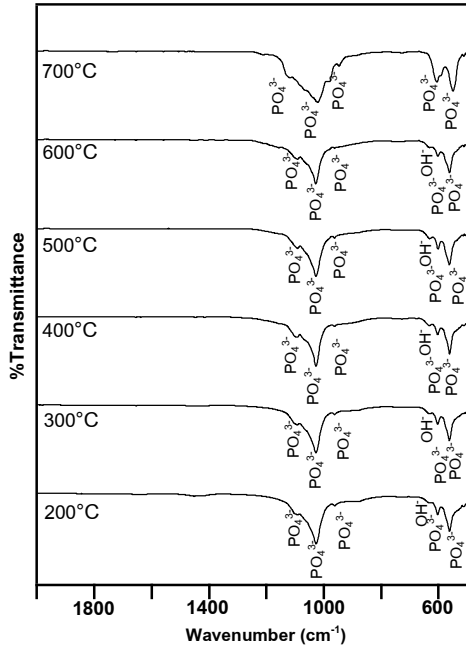


Figure 2 FTIR spectra of hydroxyapatite were synthesized various temperature

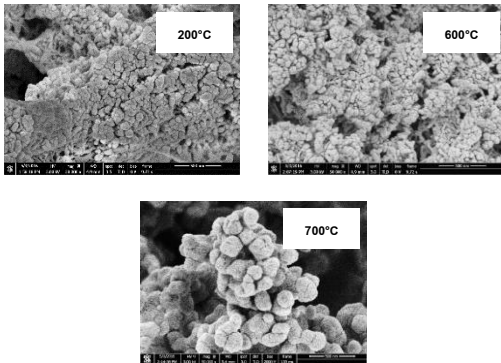


Figure 3 The FESEM images of sample powder were synthesized various temperature

The Figure 3 show the FESEM micrograph of the samples powder synthesized at various temperature. The hydroxyapatite particle at 200 and 600°C are agglomerated in sphere shape with 50 nm of diameter. However, the sample synthesized at 700°C

which is the $\text{Ca}_3(\text{PO}_4)_2$ phase was merged from high temperature during synthesizing. The particle size are around at 100 nm as shown in Figure 3. The FESEM results correspond to the XRD and FTIR result

Temperature effect on hydroxyapatite

The XRD pattern of hydroxyapatite synthesized at 200°C was heated at various temperature as shown in Figure. 4. The XRD results indicated that the hydroxyapatite phase is still after heat in the range 200 to 600°C . The crystalline size of hydroxyapatite increase with increasing of the heating temperature as shown in Figure 5. The crystalline size (D) were calculated by Scherrer's equation following the equation (3).

$$D = \frac{0.9\lambda}{\beta \cos \theta} \quad (3)$$

Where λ is 1.5405 \AA ($\text{CuK}\alpha$), β (rad) is the width of diffraction peak and θ is obtained by full width at half maximum (FWHM) middle point [7].

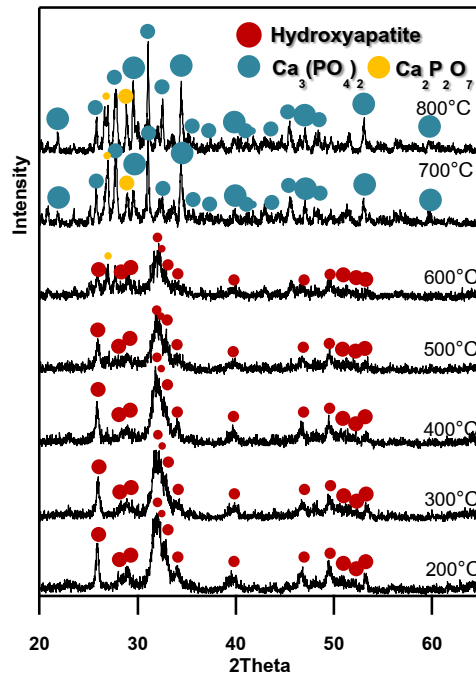


Figure 4 XRD patterns of hydroxyapatite were heated various temperature

However, the crystalline size at 600°C was dramatically decreased. The decreasing of crystalline size is due to the hydroxyapatite phase was starting transform to other phase and when the heating temperature up to 700 and 800°C the hydroxyapatite was not detect. On the other hand, the XRD pattern show the $\text{Ca}_3(\text{PO}_4)_2$ phase was detected at these both temperature. The $\text{Ca}_3(\text{PO}_4)_2$ phase was formed by the thermal decomposition of hydroxyapatite phase following an equation (2).

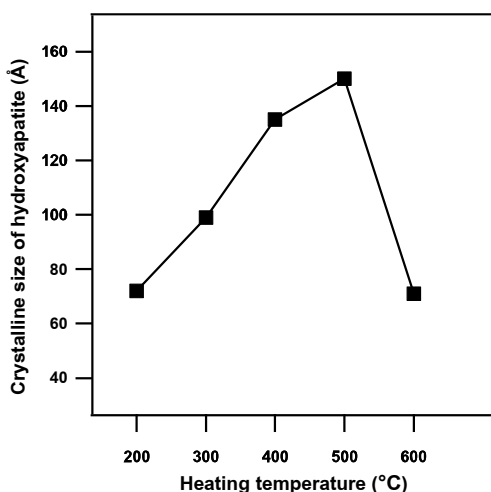


Figure 5 The crystalline size of hydroxyapatite were heated at various temperature

Conclusions

Hydroxyapatite were prepared by the reaction of $\text{Ca}(\text{OH})_2$ from waste chicken eggshells and $(\text{NH}_4)_2\text{HPO}_4$ various synthesizing temperature. At the 200 to 600°C of synthesizing temperature, the hydroxyapatite phase were observed. The hydroxyapatite phase were transformed to $\text{Ca}_3(\text{PO}_4)_2$ phase at 700°C. The sample powder synthesized at 200°C were heated treatment at 200 to 800°C. The results show that the phase of sample are similarly to the result from synthesizing temperature effect. The particle size of hydroxyapatite are sphere in 50 nm of diameter. The experiment results indicated that the hydroxyapatite can be synthesized from chicken

eggshells. Consequently, this method can reduced time and cost for biomaterials application.

Acknowledgments

The authors gratefully acknowledge the support given to this work by Faculty of Science, King Mongkut's University of Technology Thonburi.

References

- [1] Rapacz-Kmita, A., Slosarczyk, A., Paszkiewicz, Z., and Paluszkiwicz, C. 2004. "Phase stability of hydroxyapatite-zirconia (HAP-ZrO₂) composites for bone replacement". *J Mol Struct.* 704: 333-340.
- [2] Deepak, K., Divya, P., Sujal, R. C., Prasad, B. T., and Mohan, T. R. 2005. "Synthesis and evaluation of hydroxyapatite ceramics". *Trends Biomater Artif Organs.* 18: 87-93.
- [3] Ramesh, S., Natasha, A.N., Tan, C.Y., Bang, L.T., and Ching, C.Y. 2016. "Direct conversion of eggshell to hydroxyapatite ceramic by a sintering method". *Ceram Int.* 42: 7824-7829.
- [4] Gonzalez, G., Sagarzazu, A., and Villalba, R. 2006. "Mechanochemical transformation of mixtures of $\text{Ca}(\text{OH})_2$ and $(\text{NH}_4)_2\text{HPO}_4$ or P_2O_5 ". *Mater Res Bull.* 41: 1902-1916.
- [5] Bahman, N.T., Abbas F., and Reza, E.K. 2012. **Current microscopy contributions to advances in science and technology: Characterization of nanostructured calcium phosphate-based bioceramics.** Badojoz, Spain: Formatex research center.
- [6] Ibrahim, D.M., Hegazy, W.H., Mahgoub, A.E., and Abo-Elmaged, H. 2000. "Prepare and characterization of calcium hydroxyapatite". *Commun Fac Sci Univ Ank Series B.* 46: 33-46.
- [7] Miyaji, F., Kono, Y., and Suyama, Y. 2005. "Formation and structure of zinc-substituted calcium hydroxyapatite". *Mater Res Bull.* 40: 209-220.

Enhancing Student's Concept on Projectile Motion by Classroom and Outdoor Activities

F. Polthep and U. Tipparach*

Department of Physics, Faculty of Science, Ubon Ratchathani University, Warin Chamrab, Ubon Ratchathani

34190 Thailand

**Corresponding Author. Email : udom.t@ubu.ac.th*

Abstract

We have designed and created learning activities in classroom and outdoor experiments in Physics on Projectile motion. The purpose of the experiments is to increase learning achievement. The activities are composed of classroom experiment to obtain the relation between vertical and horizontal motion on the dimensions of positions and times. The students were also provided video about projectile motion in action and predicted simulation. The outdoor activities consist of projectile motion in different situations such as throwing a ball at different angles and pitching an object vertically while moving horizontally. These activities can improve students' understanding the concept of projectile motion. The students' attitude towards learning physics is positive and the retention rate is increased.

Keywords: Projectile, Learning activities, Outdoor activities

Introduction

It is generally believed that learners will learn more when taught less as the Minister of Education of Singapore embarked on "teach less, learn more"[1] in 2005. This means that learners learn more when they do experiments get trained or practiced by emphasizing on improving the quality of interaction between teachers and learners so that the learners can be more engaged in learning and better able to achieve desired outcomes of education. Many scientific and technological works are cooperative. The well-known learning pyramid by National Training Laboratories, Bethel, Maine, U.S.A., states that people will learn more and retain more their knowledge if the learning process involves doing, stimulating real experience and practicing [2]. In

addition, to understand physics and do physics, learners should have both knowledge in Physics and scientific skills. Learners will gain better understand Physics if they learn knowledge and skills in doing physics with appropriate coaching. They also should have right-positive attitude towards learning Physics [3]. In this paper, we report the students' attitudes, expectations, and beliefs towards learning Physics compared to the experts in the field before taking the lesson. We describe the hands-on lessons so that the students can carry out experiments through cooperative learning. We will probe the students' attitudes, expectations, and beliefs towards learning Physics after taking the lesson as well.

The Ministry of Education of Thailand has issued the policy "Teach less, Learn more" in 2015. To

The Ministry of Education of Thailand has issued the policy "Teach less, Learn more" in 2015. To comply by this policy, we have designed learning activities focusing on students in order that the students learn and understand by constructing their knowledge. In this way, the students gain knowledge and build their scientific skills as well as social skills.

In this work, thus, we propose developing learning activities on projectile motion for grade 10 students to enhance understanding the concept of projectile so that the students can construct their own knowledge by doing learning activities such as experiments and hands-on experience. The activities consist of in-class activities and outdoor activities.

Materials and Methods

The design of the apparatus for projectile experiment is shown in Figure 1. The real set up of the apparatus is shown in Figure 2.

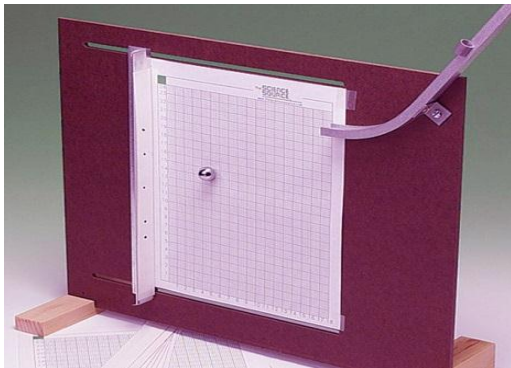


Figure 1 The designed apparatus for projectile experiment.

The purpose of the experiment is to construct students' concept of projectile. In this experiment, the students will carry out an experiment to verify that relation of positions of projectile in vertical (y) and horizontal (x) is parabola. The students are asked to plot a graph by plotting the positions of projectile in vertical (y) and the square of the horizontal (x^2) to prove that $y \propto x^2$ [4].



Figure 2 The real set up of the projectile experiment.

The students also explore the law of projectile motion in outdoor activities. The teacher asks the students questions. The questions are designed by the 5E inquiry method of teaching. The students perform a series of outdoor activities using 5E inquiry method of teaching. The examples of the questions include: which path of the projectile for a ball if the man is riding a bicycle with a certain velocity throw the ball into the air vertically.



Figure 3 A man throws a ball into the air vertically while riding a bicycle with a certain velocity.

Results and Discussion

The apparatus has been used in grade 10 Physics classroom of Khuemyai Wittaya School. The students were excited and happy to learn. They have a chance to work in a group of 5 students. They have learned Physics by doing experiments, develop scientific skills, e.g., measurement, collecting data, graphing, analyzing data, and drawing a conclusion. They also have gained social

skills such as group discussion, working together, and communication. The activities can be used to promote learning physics as proposed by Popov [5] in 2006. The average score was increased with statistical significance at .05 levels as shown in Table 1.

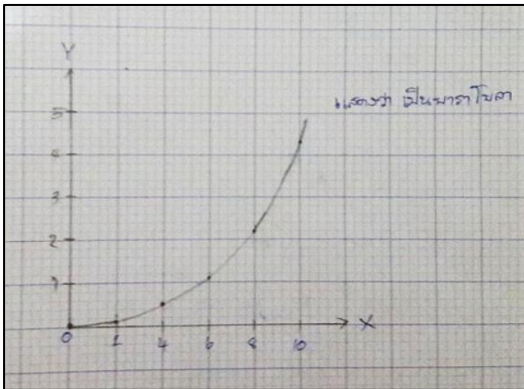


Figure 4 Students' work on relation of positions of projectile in vertical (y) and horizontal (x).

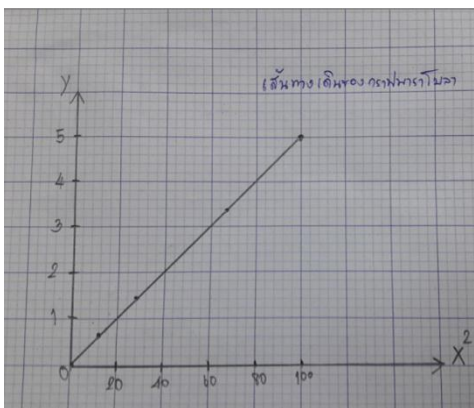


Figure 5 Students' work on relation of positions of projectile in vertical (y) and square of horizontal (x^2).



Figure 6 Outdoor activities about projectile (a) watering and (b) throwing a ball

Table 1 Mean score, average normalized gains, and t-statistics on the pre-test and post-test.

Score	Number of students	Full score 20		SD	t
		mean	percent		
pretest	34	7.38	21.7	0.99	45.74*
posttest	34	13.71	40.32	1.17	

* $t_{\alpha=.05, df=33}=1.692$

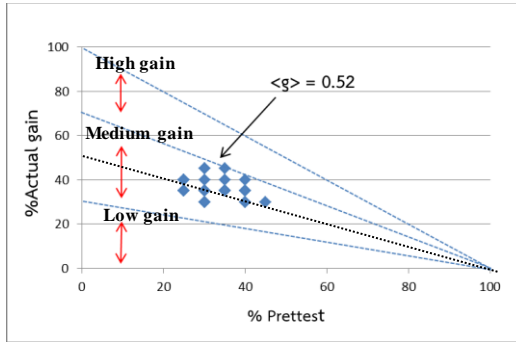


Figure 7 The relation between %pretest and %gain of the students.

The normalized gain, $\langle g \rangle$, a measure of the advancement of students' learning in scores between pre-test and post-test, was expressed as a fraction of the range of possible score increase and was also calculated by [4],

$$\langle g \rangle = \frac{\% \text{ posttest} - \% \text{ pretest}}{100\% - \% \text{ pretest}}$$

And $\langle g \rangle < 0.3$ is low gain,

$0.3 < \langle g \rangle < 0.7$ is medium gain,

$\langle g \rangle \geq 0.7$ is high gain.

The average normalized gains were 0.52 which is considered as medium gain. No student is in low gain and high gain. All students are in medium gain.

Conclusions

We have developed the apparatus for learning through inquiry and active learning methods. The learning activities helped to develop students' concepts of projectile motion. The activities also promote abilities of the student in analytical thinking on projectile motion. The students participated in Physics classroom and outdoor activities enthusiastically. They developed scientific skills and social skills at the same time.

Acknowledgments

We would like to thank the institute for the promotion of teaching science and technology (IPST) for financial supports.

References

- [1] Ho., F.F., Boo, H.K. (2007) **Asia-Pacific Forum on Teaching and Learning**, 8, 7.
- [2] McKeachie, W.J. Active Learning, http://courses.science.fau.edu/~rjordan/active_learning.htm access on July 5th, 2010.
- [3] Redish, E. F. Steinberg, R. N. Saul, J. M. (1998) **American Journal of Physics**, 66, 212-224.
- [4] The Institute for The Promotion of **Teaching Science and Technology (IPST), Physics** Vol.1, Ministry Of Education, 2012.
- [5] Oleg Popove, "Developing outdoor activities and a website as resources to stimulate learning Physics in teacher education" **J. Phys. Tehr. Educ. online**, V.3(3), 2006, 18-22.

Design and Development of an Experimental Apparatus to Study the Rotational Motion on an Inclined Plane

K. Homdungsri and V. Mekla

Faculty of Science, Ubonratchathani Rajabhat University, Ubonratchathani 34000

E-mail:Kannika7133@gmail.com

Abstract

The design of apparatus to study of a rotating double cone down an inclined plane by "Digital Photogate Timer" A timer. Researchers have designed and built a series of experiments for the moment of inertia of the double cone using a material made from superlean a rotating double cone down an Inclined plane. Which can adjust the height various values. The results obtained to calculate the moment of inertia of the double cone. Find the moment of inertia of the experiment compared with the moment of inertia was calculated from the experimental apparatus. That the moment of inertia of the experimental apparatus for the moment of inertia, which is equal to $I = 1.336 \times 10^{-6} \text{ kg.m}^2$. As a result, the moment of inertia is equal $I = 1.385 \times 10^{-6} \text{ kg.m}^2$ and percentage of error equal 3.54%

Keywords: Double cone, Moment of inertia, Digital photogate timer, Rotational motion down an Inclined Plane

Introduction

Moment of Inertia is a property of objects when rotated. The amount that the rotational inertia of an object in which to try to maintain the same rotation it. The object has a moment of inertia, it will change the object's rotation was hard, and if the object is the moment of inertia, it will cause the object to change its rotation was easy.

The rotation of rigid bodies in many cases may need to know the moment of inertia of objects. For objects with the substance to determine the moment of inertia requires calculus mathematics, which is a hassle. Students also learn therefore, it is difficult for students to calculate the moment of inertia of the object. The moment of inertia of the object about an axis of rotation. The shape of the object and the arrangement of objects around the spindle to calculate the moment of inertia of a mathematical method.

Department of Physics is a fundamental concept in the development of other health problems that can be found in the course will mainly focus on the final results of the study [1].The teaching physics with the goal that the students understand the principles, theory and experimental analysis and problem solving in physics. The laboratory is something that will help. Students have a clear understanding of the principle or theory that is clear from the map that the students have studied in books and trial is to eliminate misunderstandings in principle or theory. The trial is a form of learning that students have the opportunity to build knowledge and self-understanding and recognition at all over. Last year It is undeniable that one of the main problems of the education system in Thailand. It is inevitable that an analysis of Thailand. Still much lower than the benchmark a key contributor to several studies suggest that. Most of the educational

system that encourages children to experiment with their own search for answers. But how often do children learn facts from finished. And the kids do not have anything more specific to teaching science. Which require the trial searched survey evidence and the rational to conclude to get the answer yourself.

From the above, the researcher is interested in designing and developing a series of experiments to determine the moment of inertia on the slope of a cone. To serve as a medium of instruction is easy to use. Students will see the relationship During the moment of inertia of theoretical and experimental studies to have a clear understanding of the principle or theory that a clear plan which treatments have low production costs high-precision be attributed to teaching in high school students to understand the principles and theories correctly.

Materials and Methods

Rigid body is an object that has not changed shape while moving or under force. Rigid body comprising a Particle system (system of particle) is generally moves. Classified into three types of rigid body motion is promoted. (Translational motion) rotational motion (rotational motion) and the movement, including rotation and position (combination motion) or rolling (Rolling) [2].

Moment of inertia Depending on the shape of the object (And the mass the distribution of mass), and the moment of inertia depending on the axis of rotation [3]

The equation for kinetic energy of rotation can be rewritten in the form of the moment of inertia is

$$E_k = \frac{1}{2} I \omega^2 \quad (1)$$

If you compare the kinetic energy of rotation. The kinetic energy of the linear movement of the object. This is a

$$E_k = \frac{1}{2} m v^2 \quad (2)$$

Where m is the mass of each object, and v is the velocity of the object will see that for rotational

motion. Mass moment of inertia is the same as in the linear movement.

The linear movement an object with a mass requires more force to evoke movement. The object with a mass to use less force to move.

Rotational motion the object has a moment of inertia requires a large torque (torque), to induce rotation. The object with a moment of inertia is less than the torque to the rotation. In conclusion Moment of inertia is properties resist rotational motion. And mass properties Anti-linear movement of each object.

Researchers have designed and built a series of experiments for determining the moment of inertia of the double cone of rolling on an inclined plane. Which can adjust the height values and bring the results to calculate the moment of inertia of objects conical pair of Equation (3) by the double cone made of super-density polyethylene, which is constant throughout the whole lump. By experimental equipment shown.

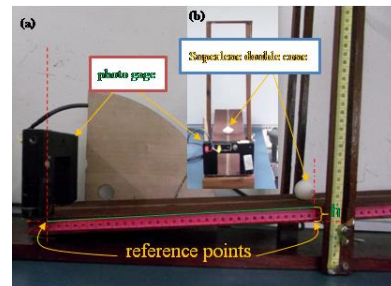


Figure1 (a) show side view test set up for moment of inertia (b) show front view test set up for moment of inertia

From the first law of motion, Newton would have that the.

$$\begin{aligned} \Sigma E &= 0 \\ Mgh &= \frac{1}{2} Mv^2 + \frac{1}{2} I\omega^2 \end{aligned} \quad (3)$$

Where m is the mass of the double cone pair (kg), h is the height measured from the reference point (m), is the acceleration due to gravitational field of the earth $9.8m/s^2$, v the velocity vector of the object at the point references (m/s), I the moment of inertia of

the double cone kg. m^2 and ω the angular speed of the object as a reference point (rad/s) and $\omega = v/R$ on which is R the radius of a double cone (m).

Moment of inertia of the double cones can be calculated from Equation (3) in this research report double cone objects is equal $M = 0.01675$ and radius $R = 0.015$ m. Then calculate the moment of inertia (I) by using Equation (3). Already defined as the moment of inertia. The object of the double cone of theories. And conducted by the organized device is shown in Figure (1). In the initial height of the slope height ($h = 0.05$ m) and set the height increments of 0.05 meters. Then let the double cone through a rolling machine timer or photocell package (cobra-interface2, PHYWE SYSTEM (THAILAND) CO.,LT) at that point, defined as a point of reference to measure height ($h = 0$). The experiment by letting the object rolled down the slope at different heights set up a total of 50 times the height save the time (t). The results into a table recording the results. Then calculate the average time taken to calculate the size of the linear velocity and then the angular speed and then bring values the graph of the relationship between height. With speed squared to determine the moment of inertia ($I_{\text{experiment}}$) then came to the percentage tolerances between the values calculated from theory of moment of inertia (I_{theory}).

Results and Discussion

Find the moment of inertia of theory

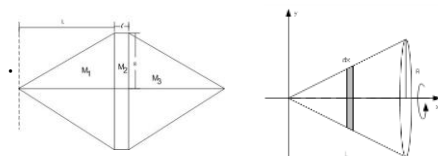


Figure 2 show drawing of double cone When moment of inertia of rigid body

When moment of inertia of rigid body

$$I = \int r^2 dm = \int \rho r^2 dV \quad (4)$$

by dV is volume element and

$$I = \int dI_1 + \int dI_2 + \int dI_3 \quad (5)$$

Consider M_1 the moment of inertia of circular cone

$$\rho = \frac{M_1}{V} = \frac{M_1}{\frac{\pi R^2 L}{3}} = \frac{3M_1}{\pi R^2 L}$$

So that

$$I = \frac{3M_1 R^2}{10} + \frac{M_2 R^2}{2} + \frac{3M_3 R^2}{10} \quad (6)$$

$$\rho = \frac{M}{V} = \frac{M}{\frac{2\pi R^2 L}{3} + \pi R^2 l}$$

When

$$M = 0.01675 \text{ kg}, R = 0.015 \text{ m}$$

$$L = 0.02 \text{ m}, l = 0.005 \text{ m}; R = 0.015 \text{ m}$$

The result is

$$\rho = 1.293 \times 10^3 \text{ kg/m}^3$$

$$M_1 = \rho V_1 = (1.293 \times 10^3) \left(\frac{(3.14)(0.015)^2 (0.02)}{3} \right)$$

$$= 0.00609 \text{ kg}$$

$$M_2 = \rho V_2 = (1.293 \times 10^3) (3.14) (0.015)^2 (0.005)$$

$$= 0.00457 \text{ kg}$$

$$M_3 = \rho V_3 = (1.293 \times 10^3) \left(\frac{(3.14)(0.015)^2 (0.02)}{3} \right)$$

$$= 0.00609 \text{ kg}$$

$$M = M_1 + M_2 + M_3 = 0.01675 \text{ kg}$$

$$I = \frac{3M_1 R^2}{10} + \frac{M_2 R^2}{2} + \frac{3M_3 R^2}{10}$$

$$I = \frac{3(0.0069)(0.015)^2}{10} + \frac{(0.00457)(0.015)^2}{2}$$

$$+ \frac{3(0.00609)(0.015)^2}{10}$$

$$I = 4.11075 \times 10^{-7} + 5.14125 \times 10^{-7} + 4.11075 \times 10^{-7}$$

$$I = 1.336 \times 10^{-6} \text{ kg.m}^2$$

The value obtained from the experiments results

records in the table below.

Table 1 The record shows the experimental results.

Time	Height (m)	The average time (s)	Speed (m/s)	Speed squared (m/s) ²
1	0.05	0.047762	0.628	0.394
2	0.10	0.027751	1.081	1.169
3	0.15	0.021288	1.410	1.989
4	0.20	0.018405	1.630	2.657
5	0.25	0.016099	1.863	3.471
6	0.30	0.014743	2.035	4.141

The obtained data to create graphs of height with speed squared for the slope.

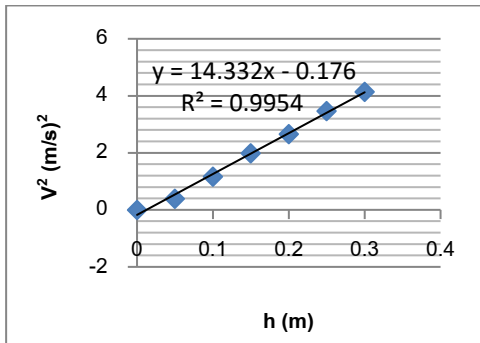


Figure 3 The graph shows the difference between the speed squared.

The slope is equal = 14.332

$$I = \frac{2MR^2g}{slope} - MR^2$$

$$I = \frac{2(0.01675)(0.015)^2(9.8)}{14.332} - (0.01675)(0.015)^2$$

$$I = \frac{0.0000738675}{14.332} - 0.00000376875$$

$$I = 5.154026 \times 10^{-6} - 3.76875 \times 10^{-6}$$

$$I = 1.385 \times 10^{-6} \text{ kg.m}^2$$

And the moment of inertia of the experiment is.

$$I = 1.385 \times 10^{-6} \text{ kg.m}^2$$

And percentages discrepancy compared to the values calculated by the theory.

$$\left| \frac{1.385 - 1.336}{1.385} \right| \times 100 = 3.54\%$$

Conclusions

In this research the researchers have designed and developed a series of experiments to determine the moment of inertia on the inclined plane of a double cone. The object made from superlean shaped as a double cone. That the moment of inertia of the experimental apparatus for the moment of inertia, which is equal $I = 1.336 \times 10^{-6} \text{ kg.m}^2$. As a result, the moment of inertia is equal $I = 1.385 \times 10^{-6} \text{ kg.m}^2$ and percentage of error equal 3.54%.

Acknowledgments

This work was made possible by the support and help of many people, the author would like to thank you for support and the tools for analysis. Ubon Ratchathani Rajabhat University

References

- [1] Boonsaard, A. Kritkharuehart, S. and Pongpiyarat, I. 2012. "The Development of Assessment of Conceptual Knowledge in Physics by Using a Concept Map". *Journal of Behavioral Science for Development* .6(1). :189
- [2] Seehamart, K. 2014. "Moment of Inertia Measurement Instrument from Rotational Motion of Rigid Body". *Rajamangala University of Technology Isan*. : 4-6
- [3] Sohang, C. and Costas, J. 2005. "The Ascending Double - Cone A Closer Look at a Familiar Demonstration". *Department of Physics University of Central Florida Orlando*. :1-16.